Mueller Matrix Confocal Scanning Laser Polarimetry and Optimal Conditions for Improved Image Quality

by

Julia Zangoulos

A thesis
presented to the University of Waterloo
in fulfillment of the
thesis requirement for the degree of
Masters of Science
in
Physics

Waterloo, Ontario, Canada, 2021

Author's Declaration

I hereby declare that I am the sole author of this thesis. This is a true copy of the thesis, including any required final revisions, as accepted by my examiners. This thesis consists of material all of which I authored or co-authored. The Statement of Contributions is included in the thesis.

I understand that my thesis may be made electronically available to the public.

Statement of Contributions

A small portion of the content included in Chapter 4 has been presented previously at Photonics North 2020 under the coauthorship of Dr. Melanie Campbell (Julia Zangoulos and Melanie Campbell. Optimal pupil size in older adults for retinal imaging. Photonics North, 2020). The content presented in Section 5.3.1 was submitted as an abstract to ARVO 2021 (Melanie Campbell, Julia Zangoulos. Reduced impact of ocular higher order aberrations on image quality when imaging the retina at longer wavelengths, ARVO 2021).

Hannah Sara Rosenberg aided with the development of the automation code presented in Chapter 4 by writing Matlab code that generated the .int files containing the Zernike polynomial coefficient for each subject and pupil size. The Flowchart in Figure 4.5 outlines Hannah's work. In addition, Hannah created the Flowcharts presented in Figures 4.5, 4.6 and 4.7. Steven Esau helped with the simulation of the polarization states on the Poincaré sphere presented in Chapter 3. By modifying his code I generated Figures 3.6, 3.8 and 3.10. In addition, conversations with Steven regarding polarization theory and instrumentation have helped tremendously during my MSc. Further, Austin Roorda's equations derived in his PhD thesis were used in Chapter 5. Julian Whiting gave valuable advise on statistical methods including regression analysis, presented in Chapter 4.

Rachel Redekop, Steven Esau, Tasia Zangoulos, Mary McPherson, and Dr. Melanie Campbell read this thesis in part or whole and provided excellent editorial feedback.

Dr. Bizheva and Dr. Sanderson gave valuable recommendations as part of my research advisory committee. Furthermore, I am thankful that Dr. Strickland agreed to be an external examiner and has reviewed this thesis.

Dr. Campbell had the most contribution to the work presented and has spent many hours helping and directing me to new research questions. I am grateful to Dr. Campbell, and extremely thankful for her contributions to my research.

Abstract

Alzheimer's disease (AD), a fatal neurodegenerative disorder, is the most common form of senile dementia. Five hundred thousand Canadians are living with dementia, a number predicted to double by 2030. Currently, the most definitive diagnosis of AD must be conducted after death due to the lack of both specific methods for detecting neurodegenerative disorders, and broadly accessible methods for screening preclinical symptoms. The disease is now known to manifest in the eye, an optically accessible structure, and so AD can be diagnosed if amyloid-β deposits are identified in the neural retina. Extensive research by Campbell labs has determined the intrinsic polarization properties of presumed amyloid-β deposits, and developed a novel Mueller-Matrix (MM) polarimetric tool that can image these deposits in *ex-vivo* retinas. Dr. Campbell's research group has shown MM polarization imaging to be a promising non-invasive, label-free diagnostic tool that provides improved image contrast and a higher signal-to-noise ratio (SNR) than conventional retinal imaging systems. Further, Dr. Campbell's group has found that amyloid-β deposits correlate well with brain pathology, making this imaging modality a strong candidate for an AD diagnostic method.

The research group is now working on a prototype live-eye MM imaging device, and this thesis contributes to this goal. The commercial market for ocular imaging technologies is highly competitive, and therefore defining design requirements that will place the MM polarimeter at a competitive position is important. The research presented in this thesis has taken into account these requirements to design an MM scanning laser polarimeter by integrating polarization optics with a donated scanning laser opthalmoscope (SLO). The polarization optics were selected based on the need for fast, repeatable and accurate polarization modulation, and to ensure a compact cost-effective product. The optimal setup of the polarization unit was identified and designed as a custom made linear holder with four quarter-waveplates placed at different orientations. This method eliminated rotation related errors, increasing the accuracy and repeatability of the polarization modulation unit.

Ocular performance and retinal imaging quality decrease during normal aging, which has important implications in the design of retina imaging instruments for the aging population. Furthermore, since optical resolution due to diffraction becomes better with increasing pupil size, whereas that due to aberrations becomes worse, the optimal pupil size for best lateral resolution as a function of age had to be determined. Eye models incorporating monochromatic aberrations of individual eyes were designed in Code V to determine optimal imaging parameters for retinal instruments targeting the older population. The optimal pupil size for best lateral resolution obtained from the encircled energy metric, in

adults 58-70, was found to be 2.73 mm $\pm$ 0.402 mm, providing a lateral resolution of 4.48 $\mu m \pm 0.654$ μm ($\lambda = 550$ nm). The optimal pupil size for best lateral resolution, in adults 20-32, was found to be 3.09 mm $\pm$ 0.488 mm, providing a lateral resolution of 3.95 μm $\pm$ 0.6 μm ($\lambda = 550$ nm). The optimal pupil size was found to be statistical significant with age. Further, regression analysis indicated that optimal pupil size as a function of higher order wavefront error gave an exponential fit ($R^2 = 0.75$). These findings when implemented can enable high resolution retinal imaging without the use of adaptive optics. In addition, the optimal pupil size for best lateral resolution for an 830 nm imaging wavelength, in adults 58-70, was found to be 3.13 mm $\pm$ 0.486 mm, providing a lateral resolution of 5.9 $\mu m \pm 0.848$ μm. It was also determined that in the presence of high aberrations at large pupil sizes, higher wavelengths do not introduce additional aberrations than in lower wavelengths.

In-vivo imaging of the human retina is a unique optical process because the retina is not directly accessible, so imaging must be done by detecting the double-pass reflection. Modalities for imaging the human retina using this approach have existed for many years and are constantly improving. Two specific optical setups, optimized for imaging amyloid-β deposits in older adults, are designed and presented in this thesis. The retinal image quality of the MM polarimeter using an SLO setup with a small entrance pupil was almost solely affected by the aberrations and diffraction of light leaving the eye in the second-pass, making it a single-pass method. In addition, the MM polarimeter with a conventional SLO setup with a large exit beam, which uses an optimal entrance pupil size and the whole exit pupil, was also found to be a single-pass modality. Thus, in this second configuration, image quality depends only on the first-pass. Optimal pupil and pinhole sizes for 830 nm light were implemented in the optical design of both setups for the development of a system designed to image retinal amyloid-β deposits in older adults as a diagnostic tool for AD.

In summary, an MM confocal scanning opthalmoscope was designed and optimized for imaging the retinal amyloid-β deposits in older adults.

Acknowledgements

Thank you to my supervisor Dr. Melanie Campbell for her guidance, advice and encouragement. Thank you to my fellow lab members Rachel Redekop, Laura Emptage, Steven Esau, Hannah Sara Rosenberg, Peter Neathway, Olivia Tong, Yunyi Qui, Erik Mason, Monika Kitor, Yifan Ding and Nathan DeJong for helpful discussions. It was a privilege to be a part of this outstanding research group. I would also like to aknowledge the University of Waterloo and our funding agencies, the Natural Sciences and Engineering Research Council of Canada and the Canadian Institutes of Health Research.

Dedication

This is dedicated to my mum and dad, Tasia and Nikos Zangoulos, who taught me the value of hard work. You have been my greatest strength and support. This thesis is also dedicated to my beloved grandparents, whose love knew no bounds: Timotheos and Androulla Zangoulos, Andreas and Julia Loizides, you are always in my heart and thoughts. Next, I am dedicating this thesis to my brother and sister, Timos and Andrea Zangoulos, who have been a constant source of encouragement and make me proud everyday. Last but not least, I am dedicating this to Julian, who has always found a way to make me smile, even in the worst of days.

Table of Contents

List of Figures

List of Tables

List of Abbreviations

AD	Alzheimer's Disease
MM	Mueller-matrix
SLO	Scanning laser opthalmoscope
cSLO	Confocal scanning laser opthalmoscope
AO	Adaptive optics
RNFL	Retinal Nerve Fiber Layer
ONH	Optic nerve head
SNR	Signal-to-noise ratio
PSF	Point spread function
MTF	Modulation transfer function
OTF	Optical transfer function
EE	Encircled energy
FWHM	Full width at half maximum
SR	Strehl ratio
NA	Numerical aperture
LP	Linear polarizer
QWPL	Quarter waveplate
PSG	Polarization state generator
PSA	Polarization state analyzer
SOP	State of polarization
PEM	Photo-electic modulator
LOC	liquid crystal
MO	magneto-optic
FOV	Field of view
TDL	Times-diffraction-limited
LED	Light-emitting diode
TRA	Transmission characteristic analysis

Chapter 1

Introduction

Alzheimer's disease (AD) is a fatal neurodegenerative disorder associated with a variety of cognitive and neuropsychiatric symptoms [84]. AD is the most common form of senile dementia affecting 60–70% of dementia cases [186]. Worldwide, 50 million people are living with dementia, with 10 million new cases estimated every year. Five hundred thousand Canadians currently have dementia, and this number is predicted to double by 2030 [3]. Classically, AD is characterized by two cardinal pathologies which involve amyloid-β plaques and neurofibrillary tangles in the brain [84]. At present, the most definitive diagnosis of AD is conducted after death by histological brain examination [46, 84] because we lack both specific methods for detecting neurodegenerative disorders, and broadly accessible methods for screening preclinical symptoms. Statistical reports on the disease demonstrate a large socioeconomic impact which is predicted to become more prevalent over the years [55, 88]. While there is extensive research into AD pathology and on methods to delay disease progression, no cure is available. However, therapeutic and preventive strategies have been discovered that can induce small delays in the onset and progression of AD [29]. Therefore, an early diagnosis of AD may enable existing treatment methods to provide more successful results [55, 103, 140]. Traditionally, AD has been considered as a disease manifested in the brain. However, the manifestation of the disease in the eye, which is a developmental outgrowth of the brain, led to the discovery of imaging techniques to visualize the deposits in the retina [46, 84]. Intrinsic polarization properties of amyloid-β deposits were discovered in Campbell labs [45, 46, 58, 97, 145]. Mueller-matrix (MM) polarization imaging was implemented in Campbell labs and amyloid-β deposits were imaged in *ex-vivo* retinas. MM polarization imaging was found to improve visualization of amyloid-β by enhancing contrast and signal-to-noise ratio (SNR) without the need of a staining method [34, 46]. Furthermore, this unique optical inspection method provides

additional morphological information that can reveal features in a sample that cannot be resolved using conventional intensity or phase imaging systems [2, 15, 34, 61, 144]. Thus, MM polarization imaging of presumed amyloid-β deposits is a promising method for AD diagnosis [46].

Our lab is developing a prototype *in-vivo* MM polarimeter and this thesis aims to contribute to this purpose. While MM polarimetry is a novel imaging method, polarization related errors are a characteristic challenge in this modality [167, 170]. These polarization related errors can be reduced by optimizing the selection and design of the polarization modulation units responsible for modulating the state of polarization in the optical setup [80, 108, 110, 168]. Chapter 3 presents the optical design of the MM confocal scanning laser polarimeter by integrating polarization optics in a donated scanning laser opthalmoscope (SLO). In addition, design requirements and specifications were identified in order to place this diagnostic instrument in the forefront of a highly competitive market of retinal imaging diagnostic systems. A custom-made, optimal method for polarization modulation was presented, which provided high polarization modulation accuracy and repeatability, while eliminating common polarization related errors.

The *in-vivo* MM scanning laser opthalmoscope uses the ocular optics as a microscope objective. Therefore, image quality is limited by both the aberrations from ocular optics and diffraction through the pupil. Identifying optimal pupil sizes that balance the effect of ocular aberrations and diffraction can allow high resolution imaging without the need of adaptive optics (AO), resulting in a more affordable diagnostic device.

In addition, ocular optics change as a function of age [4, 11, 11, 13, 82, 137, 152]. This age dependency suggests that optimal pupil sizes vary as a function of age and is described by anatomic changes in the human eye [78]. Multiple studies on the corneal wavefront aberrations indicated that coma increases with age due to the increased asymmetry during aging [4, 82, 137]. Spherical aberration caused by the cornea surface were found to be invariant with age, indicating that other structures may be responsible for the age-dependent reduction of image quality in the human eye [4, 11, 137]. Glasser and Campbell were among the first to identify the substantial increase of spherical aberration of the crystalline lens [75, 121]. The lens changes with age by increasing surface curvatures, and by changing the refractive index [75]. Thickening of the lenticular cortex and hardening of the lens were also observed in older adults [76]. Further, the total aberrations from the corneal and crystalline lens in the younger eye enables an improved retinal image [11, 13, 66, 154]. Many research groups have determined that when studying aberrations of the cornea and crystalline lens separately there was high coma and spherical aberration. However, when studying the cornea and crystalline lens as a combined system, an overall reduction of wavefront aberration was observed in younger eyes [13, 66, 154]. The

researchers attributed this reduction to the fact that in younger subjects the crystalline lens aberrations compensate for the corneal aberrations. This property was found to be lost with increasing age, leading to reduced retinal image quality [11, 13, 66]. Therefore, the anatomical changes demonstrate the progressive decline of average optical performance of the human eye with age by increasing wavefront aberrations [81, 82].

The increase of monochromatic ocular wavefront aberrations as a function of age, which was documented by several research groups, explains the decline of optical performance and retinal image quality [40, 73, 121, 150]. In Chapter 4, higher order (HO) wavefront aberrations of a large population was used to study how different optical performance metrics change as a function of pupil size and age when taking into account both diffraction and wavefront aberrations. From this study optimal pupil sizes were determined for maximizing lateral resolution as a function of age. Since AD is prevalent in older adults, optimizing the optical setup by selecting optimal pupil and pinhole sizes for this specific population will be shown to significantly improve image quality, by approaching the diffraction limit at an optimal pupil that best balances the effect of diffraction and aberrations, providing high resolution imaging even without AO. Furthermore, results from this chapter could be used as a benchmark for other optical systems, other than the MM polarimeter and SLO, that are specialized for specific populations. Lastly, Chapter 5 presents an optimized design of the MM scanning laser opthalmoscope, which is presented in Chapter 3, by using the optimization condition identified in Chapter 4 and extended in Chapter 5.

In conclusion, this thesis contributes to the prototype AD diagnostic instrument being developed by Campbell labs, by proposing a modified optical design that provides improved image quality and is population specific. The design reduces polarization-related errors, provides a large field of view, and allows label free imaging that further enhance this modality by adding to the instrument's competitiveness in the commercial market.

Chapter 2

Background

2.1 Polarized light

2.1.1 Wave Representation of polarized light

Polarization is a fundamental property of electromagnetic waves, which stems from the vectorial nature of light, and polarimetry is the science of measuring polarization [23, 61, 74, 86]. Light is a transverse electromagnetic wave, where the electric and magnetic fields oscillate 90 degrees apart, and are perpendicular to the wave propagation direction [61]. The temporal evolution for the x and y components of the electric field of a quasi-monochromatic electromagnetic wave can be expressed as [74, 86]:

$$\vec{E}_x(z,t) = A_x(t)\cos(\omega t - kz + \phi_x)\hat{x} \tag{2.1}$$

$$\vec{E}_y(z,t) = A_y(t)\cos(\omega t - kz + \phi_y)\hat{y} \tag{2.2}$$

where A_x, A_y are amplitudes and (ϕ_x, ϕ_y) are phase factors of the wave in the x and y directions; k is the wavenumber, $k = \frac{2\pi}{\lambda}$; and ω is the angular frequency, $\omega = 2\pi f$ [74]. The vector sum of these two perpendicular waves describes the cumulative temporal evolution of an electric field, described in Equation 2.3

$$\vec{E}(z,t) = \vec{E}_x(z,t) + \vec{E}_x(z,t) \tag{2.3}$$

As the electromagnetic wave travels along the z direction though one wavelength, the electric field progresses through one complete oscillatory cycle [74, 86]. Thus, the electric field vector traces an elliptical pattern for each cycle. The polarization state of the

electromagnetic wave is determined by the relative phase difference, $\phi = \phi_x - \phi_y$ between the x and y components of the electric field and the amplitude of each component, A_x, A_y [86]. Given that the phase of both x and y components of the electromagnetic wave are equal, $\phi = 0$, or have a phase difference that is a scalar multiple of π, light is said to be linearly polarized [74, 86]. When the x and y amplitudes are equal and the relative phase difference is $-\pi/2 + 2m\pi$, where $m = 0, \pm1, \pm2$, and so on, the electromagnetic wave is circularly polarized [74, 86]. When the electric field vector is rotating clockwise the light is described as right-handed circularly polarized (RHCP), otherwise it is left-handed circularly polarized (LHCP) [86]. Linear and circular polarization are two special cases of elliptically polarized light [86]. Elliptical polarization results from a difference of both amplitude and phase of the x and y electric field components. Elliptically polarized light can be described as the vector sum of circular waves with different amplitudes or the vector sum of two linear polarized waves with a different phase [61, 74, 86].

2.1.2 Polarization ellipse and Stokes parameters

The polarization ellipse is a useful concept in optics as it describes the evolution of the electric field [74]. To derive the polarization ellipse equation, the electric field components are expressed in Equation 2.4, using $\tau(t) = \omega t - kz$ as derived in [74, 97].

$$E_x(t) = A_x(t)cos(\tau(t)) \tag{2.4}$$
$$E_y(t) = A_y(t)cos(\tau(t) + \phi) \tag{2.5}$$

A_x, A_y are amplitudes in the x and y directions; k is the wavenumber, $k = \frac{2\pi}{\lambda}$; ω is the angular frequency, $\omega = 2\pi f$; and ϕ is the phase difference, between the x and y components of the electric field [74]. Dividing the electric field components with the amplitude, and using fundamental trigonometric equations the expressions expand to [74, 97]:

$$\frac{E_x(t)}{A_x(t)} = cos(\tau(t)) \tag{2.6}$$
$$\frac{E_y(t)}{A_y(t)} = cos(\tau(t) + \phi) = cos(\tau(t))cos(\phi) - sin(\tau(t))sin(\phi) \tag{2.7}$$

Combining the two electric field components the equation becomes:

$$\frac{E_y(t)}{A_y(t)} - \frac{E_x(t)}{A_x(t)}cos(\phi) = -sin(\tau(t))sin(\phi) \tag{2.8}$$
$$= -[(1 - (\frac{E_x(t)}{A_x(t)})^2)^{1/2}]sin(\phi) \tag{2.9}$$

By squaring and rearranging, the polarization ellipse equation is derived as:

$$\left(\frac{E_x(t)}{A_x(t)}\right)^2 + \left(\frac{E_y(t)}{A_y(t)}\right)^2 - 2\frac{E_x(t)E_y(t)}{A_xA_y(t)}cos\phi(t) = (sin\phi(t))^2 \tag{2.10}$$

For monochromatic light in vacuum, the amplitudes $A_x(t)$, $A_y(t)$ and the phase $\phi(t)$ stay constant. Hence, the shape and size of the ellipse is constant throughout its propagation as illustrated in Figure 2.1 [74, 86, 97].

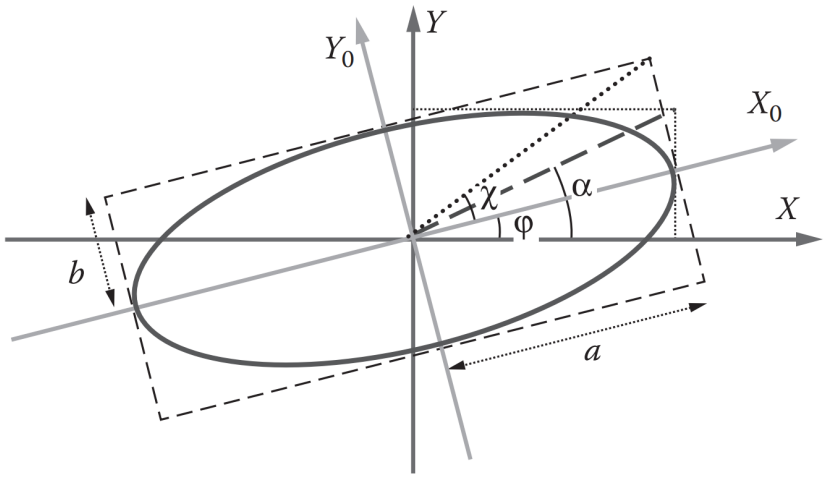

Figure 2.1: Polarization ellipse described by Equation 2.10 with azimuth $\psi(t)$ and ellipticity $\chi(t)$ [74]. Reprinted with permission from Taylor & Francis Group provided by the Copyright Clearance Center.

In addition, azimuth $\phi(t)$ and ellipticity $\chi(t)$ are used to describe the orientation and shape of the ellipse. To derive the azimuth and ellipticity equations, α is first determined, which is the ratio of the amplitudes, $\alpha(t) = arctan(\frac{A_y}{A_x})$ $(0 \leq \alpha \leq \pi/2)$ and is used in Equation 2.11.

$$tan2\alpha(t) = \frac{2A_x(t)A_y(t)cos\phi(t)}{A_x(t)^2 - A_y(t)^2} \tag{2.11}$$

Then, the azimuth $\psi(t)$ and ellipticity $\chi(t)$ can be computed from Equations 2.12 and 2.13

[74].

$$tan2\psi(t) = \frac{2A_x(t)A_y(t)cos\phi(t)}{A_x(t)^2 - A_y(t)^2} = tan2\alpha(t)cos\phi(t) \tag{2.12}$$

$$sin2\chi(t) = \frac{2A_x(t)A_y(t)cos\phi(t)}{A_x(t)^2 + A_y(t)^2} = sin2\alpha(t)sin\phi(t) \tag{2.13}$$

The description of light in terms of the the polarization ellipse allows to easily describe polarization states by a single equation. However, the shortcoming of this method is that it only describes light that is completely polarized, which is an idealization of the true behavior of light. Therefore, it is suggested that polarized light should be described in terms of observed or measured quantities such as intensity [20, 23, 61, 86].

An alternative method for visualizing the states of polarization was introduced by Sir Gabriel Stokes who described polarization in terms of observables [77]. Using this method, the four measurable quantities, called the Stokes polarization parameters, can completely describe the state of polarization. These four parameters can be derived by the equation of the polarization ellipse and by considering average values of the optical field. An equivalent equation to the polarization ellipse is described as:

$$\left(A_x^2 + A_y^2\right)^2 - \left(A_x^2 - A_y^2\right)^2 - \left(2A_xA_ycos\phi\right)^2 = \left(2A_xA_ysin\phi\right)^2 \tag{2.14}$$

Each grouped term of Equation 2.14 represents a Stokes parameter for a plane wave, which satisfies the relationship of $S_0^2 - S_1^2 - S_2^2 - S_3^2 = 0$ for monochromatic light and $S_0^2 \geq S_1^2 + S_2^2 + S_3^2$ for partially polarized light.

$$S_0 = A_x(t)^2 + A_y(t)^2 \tag{2.15}$$

$$S_1 = A_x(t)^2 - A_y(t)^2 \tag{2.16}$$

$$S_2 = 2A_x(t)A_y(t)cos\phi \tag{2.17}$$

$$S_3 = 2A_x(t)A_y(t)sin\phi \tag{2.18}$$

The Stokes parameters can also be expressed as follows:

$$S_0 = I_x + I_y \tag{2.19}$$

$$S_1 = I_x - I_y \tag{2.20}$$

$$S_2 = I_{+45} - I_{-45} \tag{2.21}$$

$$S_3 = I_R - I_L \tag{2.22}$$

$I_x, I_y, I_{+45}, I_{-45}, I_R, I_L$ are the intensity of linearly polarized light along the x axis, y axis, +45 degree axis, 45 degree axis, and right and left circularly polarized light, respectively. The Stokes vectors are commonly arranged in a column vector and written as:

$$S = \begin{bmatrix} S_0 \\ S_1 \\ S_2 \\ S_3 \end{bmatrix} \tag{2.23}$$

2.1.3 The Mueller-matrix and Mueller-stokes formalism

The Mueller-Matrix (MM), introduced by Hans Mueller, describes the mapping between an input Stokes vector S_{in} to another output Stokes vector, S_{out} [74, 86, 97]. The interaction of polarized light and a structure has the ability to change the state of polarization and therefore varies the Stokes vector. The MM is a powerful tool for describing this interaction. The polarized light and its interaction with the sample can be represented using two mathematical methods: the Jones formalism and the Mueller-Stokes formalism. Since depolarization effects cannot be computed using the Jones formalism, the Mueller-Stokes formalism is used in this work [77, 97]. The mathematical formalism of the Mueller-Stokes method using the 4×4 MM is described as follows:

$$S_{out} = MMS_{in} \tag{2.24}$$

$$\begin{bmatrix} S'_0 \\ S'_1 \\ S'_2 \\ S'_3 \end{bmatrix} = \begin{bmatrix} m_{00} & m_{01} & m_{02} & m_{03} \\ m_{10} & m_{11} & m_{12} & m_{13} \\ m_{20} & m_{21} & m_{22} & m_{23} \\ m_{30} & m_{31} & m_{32} & m_{33} \end{bmatrix} \begin{bmatrix} S_0 \\ S_1 \\ S_2 \\ S_3 \end{bmatrix} \tag{2.25}$$

The elements of the MM describe the interaction between polarized light and structures that have the ability to change the state of polarization. Therefore, by recording the input Stokes vector, S_{in}, and output Stokes vector, S_{out}, one can calculate the MM elements. The behavior of a sample in changing the state of incoming polarized light can be determined from the MM elements. Among other polarimetric techniques the MM formalism is the only one that gives access to the effects of a sample on polarized light [77, 85].

The measurement of a single output Stokes vector cannot infer all the elements of the MM. A number of unique combinations of input and output states are required to infer

all sixteen elements of the MM. To determine all polarimetric properties of the sample at least sixteen linearly independent combinations are required. The implications of this requirement on the instrumentation is that four unique polarization states need to be generated using the polarization state generator (PSG) and four unique polarization states need to be generated using the polarization state analyzer (PSA). Therefore, the measured intensity using a pair of PSG and PSA, which consist of rotating waveplates, with fast axis orientation g_n and a_n, respectively, and with the MM of the sample defined as M_s is given as :

$$I_{g_n,a_n} = (S_A(a_n))^T M_s S_G(g_n) \tag{2.26}$$

Using a PSG and PSA 16 intensity values are obtained as indicated in Equation 2.27.

$$\begin{bmatrix} I_{g1\alpha1} & I_{g2\alpha1} & I_{g3\alpha1} & I_{g4\alpha1} \\ I_{g1\alpha2} & I_{g2\alpha2} & I_{g3\alpha2} & I_{g4\alpha2} \\ I_{g1\alpha3} & I_{g2\alpha3} & I_{g3\alpha3} & I_{g4\alpha3} \\ I_{g1\alpha4} & I_{g2\alpha4} & I_{g3\alpha4} & I_{g4\alpha4} \end{bmatrix} = I = M_A M_s M_G \tag{2.27}$$

The 4 states for each of the PSG and PSA are required as indicated below

$$M_G = (S_G(g_1), S_G(g_2), S_G(g_3), S_G(g_4)) \tag{2.28}$$

$$M_A = \begin{bmatrix} S_A(a_1) \\ S_A(a_2) \\ S_A(a_3) \\ S_A(a_4) \end{bmatrix} \tag{2.29}$$

Therefore, the full MM of the sample of interest can be computed as

$$MM_s = (M_A)^{-1} I (M_G)^{-1} \tag{2.30}$$

The MM measurement enables us to quantitatively determine optical properties including retardance, diattenuation and depolarization using various decomposition techniques [115, 170]. Additional polarization properties are discussed by other members of Campbell labs in [131, 145] and are not described here as they are beyond the scope of this thesis.

2.1.4 State of polarization and the Poincaré Sphere

The Poincaré sphere, which was introduced by Jules Henri Poincaré, is described as the spherical surface formed by completely polarized states. Poles represent circular polarization where the upper-hemisphere represents left handed circular polarization and the lower hemisphere represents the right handed circular polarization. The equator represents linear polarizations. [23, 97]. The degree of polarization of partially polarized light is defined as $P = \frac{\sqrt{S_1^2+S_2^2+S_3^2}}{S_0}$. Therefore, the Stokes vector can be represented as follows, where P represents the degree of polarization of polarized light, $\psi(t)$ and $\chi(t)$ is the azimuth and ellipticity, respectively:

$$S = S_0 \begin{bmatrix} 1 \\ Pcos2\phi cos\chi \\ Psin2\phi cos\chi \\ Psin2\chi \end{bmatrix} M \tag{2.31}$$

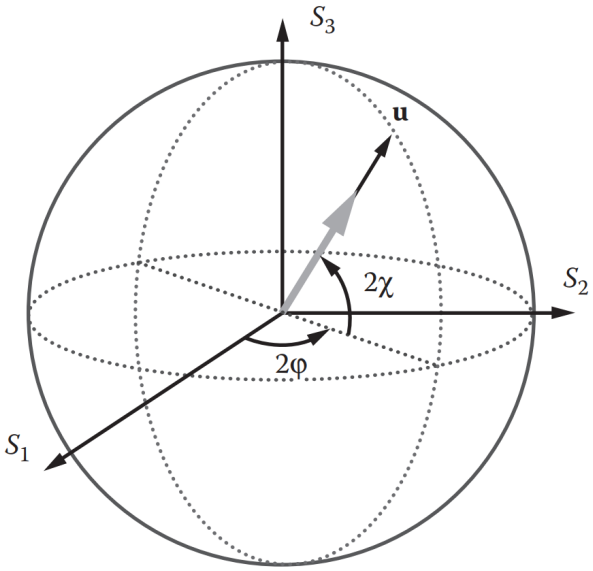

Figure 2.2: The Poincaré Sphere described by Equation 2.14 with azimuth angle $\phi(t)$ and ellipticity angle $\chi(t)$. u is the point on the sphere representing the polarization state and P=1 [74]. Reprinted with permission from Taylor & Francis Group provided by the Copyright Clearance Center.

The elements in Equation 2.31 form a vector presented in Equation 2.32 where S is a point on the Poincaré sphere. The Poincaré sphere is illustrated in figure 2.2 and the evolution of the vector on the sphere is described by the MM, as introduced in the previous section.

$$s = (cos2\phi cos\chi, sin2\phi cos\chi, sin2\chi) \tag{2.32}$$

2.2 Polarization properties of ocular structures

The polarization properties in ocular structures must be clearly understood before undergoing any investigation of methods for assessing retinal disease by means of polarimetric imaging. This need arises because retinal imaging is conducted by detecting reflected light that has traversed twice though the ocular optics, double passing through the cornea, lens, aqueous humor and upper layers of the retina. Therefore, light polarization may be affected when light interacts with the ocular optics during retinal imaging. Although there is a plethora of published work on the interaction of polarized light with ocular structures, quantitative findings are not always consistent because of the numerous polarimetric imaging methods that are used, and the complexity of the ocular optics [20, 34, 105, 114, 170, 171, 176].

The cornea has been modeled as a biaxial crystal, which has a fast principal axis normal to its surface and a slow axis nasally downward [171], causing birefringent polarization properties. The birefringence of the cornea stems from cylindrical, collagenous fibril lamellae present in the stroma. Each of the individual lamella, which are stacked, consists of fibrils of different refractive indices [37, 50, 114, 171]. It has been documented that when light is incident normal to the surface of the cornea, the birefringence is weaker at the central part of the cornea [37, 114]. However, due to the curvature of the cornea, when light enters the eye parallel to the optical axis but off axis, it makes an angle with the normal of the corneal surface. This angle of incidence results in a retardation, [114] which has been documented by multiple authors as a saddle like curve of retardance as a function of position in pupil plane [37, 114, 171]. In addition, it was concluded by multiple authors that "corneal retardance lies in the approximate range of zero to 120 degrees, with the axis ranging from slightly nasally downward to highly nasally upward" [37, 171]. This variation is dependent on the wavelength, angle of incidence, the retardance measurement methods, and from person to person. In addition, it was determined that dichroism is negligible, and depolarization is very small when light interacts with the cornea but this may increase in older eyes [32]. Therefore, it has been concluded that the cornea contributes to the state of polarization, mostly by means of its birefringent structure [37, 114, 171].

The crystalline lens is another ocular structure that is characterized by its birefringence signature [35, 122, 176]. Birefringence stems from the arrangement of cellular structures, and from the structure of fiber membranes and interstitial cytoplasm [35, 170, 176]. Intrinsic and form birefringence were found to be similar in magnitude and have opposite signs, resulting in a small retardance value [35, 122, 176]. Published work by Bueno and Campbell found an average lens retardance of 6.97 $\pm$ 1.79 degrees, which is axially symmetric in the center, and decreases from center to the edge of the lens [35]. In addition, diattenuation was found to be on average 0.051 $\pm$ 0.032, and the degree of polarization was found to be 0.64 $\pm$ 0.04. In comparison to the birefringence of the cornea, that of the lens is negligible, and thus the polarization properties, except depolarization, are often neglected [35]. Bueno and Campbell reported significant depolarization in older lenses and suggested that it is an important polarization property that should be taken into account when studying polarization properties of the light that passes twice through the ocular media and may have an age dependence [35]. Further, a later study found a non-significant numerical increase of birefringence with age and sex [176].

Together with the polarization effects in the lens and cornea, the aqueous humor is also characterized by polarization effects [122]. Optical activity has been identified by chircal compounds that minimally rotate linear polarized light as it interacts with the aqueous solution [122]. The optical activity stems from the presence of multiple compounds within the aqueous humor, including glucose, albumin, and ascorbic acid and is negligible [122].

The polarization properties of the retina have also been studied extensively by many research groups [44, 49, 90, 99]. The polarization properties of the retina originate from the retinal nerve fiber layer (RNFL), the Henle layer and the fovea. When birefringence of the RNFL was measured experimentally in several studies [49, 90, 99], it was determined that the RNFL exhibits linear birefringence. The RNFL birefringence originates from the orientation of the cylindrical structure of ganglion cell axons, and its magnitude depends on the density and composition of axon organelles [90]. The birefringence has been found to vary circularly around the optic nerve head (ONH). It is strongest in the superior and inferior locations, and lowest in the nasal and temporal regions[49, 90, 99]. Using a complete MM polarimeter, Campbell and Bueno determined that the RNFL has high linear polarizance and depolarization [44, 141]. The small RNFL diattenuation indicates that the retina differentially absorbs or reflects polarized light. Further, the interaction of polarized light with the ONH partially depolarizes incident light [44]. The Henle fiber layer and the RNFL have similar polarization properties [101]. The Henle fiber layer has demonstated birefringence and form diattenuation properties, which originate from the Henle's fibers that extend radially from the fovea [101]. In addition, it was determined that the macula area has diattenuation properties, forming the Haidinger's brush polarization

pattern [124, 170]. The polarization properties of the RNFL are employed in a widely used method for monitoring the health of the ganglion cells and this polarization signature of the RNFL has been linked to glaucoma [105, 106].

In conclusion, the eye is a complex structure characterized by ocular components that have distinct polarization signals. Therefore, when obtaining the MM of a specific ocular component, it is important to keep track of the polarization changes induced by other parts of the eye. Understanding the polarization signature of ocular structures is crucial for determining methods to identify the polarization signatures of amyloid-β on the retina *in-vivo*, as discussed in Section 2.3.

2.3 Polarization signal of retinal amyloid-β deposits

The presence of amyloid-β deposits in the neuronal retina and their intrinsic polarization properties enable label-free visualization of deposits using MM polarimetry [46, 84]. The MM amyloid-β properties and polarization contrast demonstrate great potential to be used as a non-invasive diagnostic tool [46]. Ocular structures, other then the amyloid-β deposits also demonstrate polarization properties, and were described in the previous section. It was determined by Campbell et. al. that polarization signals from amyloid-β deposits are significantly higher than that of the surrounding ocular optics [24, 45, 46, 58, 97, 145]. Assessing tissue with MM polarimetry provides additional morphological and composition information, while also enabling label free characterization of pathological changes [2, 15, 34, 144]. Further, it was experimentally determined that polarization imaging provides improved image contrast and a higher signal-to-noise ratio (SNR) than conventional retinal imaging systems [2, 15, 34, 61, 144].

2.4 Confocal scanning laser opthalmoscopy

Optical inspection of the human retina has been conducted for many years [14, 107, 149, 177, 178, 181]. The scanning laser opthalmoscope (SLO) is a sophisticated retinal imaging method, which is widely used in vision science [14, 149, 177, 178, 181]. The limitations of fundus photography, a retinal imaging modality that uniformly illuminates the retina, led to the development of the SLO [59, 134, 177]. The SLO, first presented by Webb [177], uses a monochromatic illumination source and a scanning unit, where the focused input beam is raster scanned on the retina. Reflected light from the retina by-passes some of the input beam optics, and is then recorded by a detector at each scan position. In comparison to

preceding retinal imaging modalities, the SLO has improved contrast and optical quality in retinal images. A later development, the confocal scanning laser opthalmoscope (cSLO), uses a confocal aperture prior to the detector, which is usually optically conjugate to the illumination spot on the retina. Thus, the cSLO further reduces out of focus scattering in the image plane by blocking light scattered from planes and points other than the illumination spot, and further improves image contrast.

Chapter 3

Mueller-matrix scanning polarimeter design: Retrofitting polarization modules in the original SLO

3.1 Introduction

Conventional commercially available retinal imaging systems record the intensity and phase of scattered or reflected light from retinal structures. Mueller-matrix (MM) polarization retinal imaging enables optical inspection that can reveal features that cannot be detected using conventional retinal imaging systems [2, 15, 34, 61, 144]. Assessing tissue polarization properties provides additional morphological and composition information, while also implementing label free characterization of pathological changes [2, 15, 34, 144]. In addition, it was experimentally determined that polarization imaging provides improved image contrast and a higher signal-to-noise ratio (SNR) than conventional retinal imaging systems [2, 15, 34, 61, 144].

MM polarization imaging requires an imaging modality that can collect light from a sample of interest. Therefore, retinal polarization imaging is usually done in conjunction with another modality that collects intensity information from the imaged structure. One of the widely used methods for ophthalmic polarization imaging is using a scanning laser opthalmoscope (SLO) [177] and integrating the polarization optics in the optical path, creating a MM confocal scanning polarimeter.

In this chapter, I first describe a donated SLO. The optical setup of the input illumination, pinhole detection, fixation and pupil tracking channels of the donated SLO are

presented in Section 3.2. Design constraints for the modified polarization instrument, the MM confocal scanning laser polarimeter are presented in Section 3.3. These design constraints provide the motivation for the modifications presented in this chapter and in Chapter 5. The MM scanning laser polarimeter, which is realized by retrofitting the polarization modules in the donated SLO, is presented in Section 3.5. The selection of QWPLs for polarization modulation in the MM scanning laser polarimeter is explained by a comparative literature review, which is carried out between three highly used methods for polarization modulation, and is presented in Section 3.6. Lastly, Section 3.7 characterizes the instrument performance, and required modifications are identified and discussed in Section 3.8. Additional modifications based on the optical quality analysis presented in Section 3.7 are implemented in Chapter 5 to satisfy the design constraints.

The optical design work presented in this chapter contributes to the development of a prototype instrument, the MM confocal scanning laser polarimeter, for Alzheimer's disease (AD) diagnosis. The material presented in this chapter is theoretical and can be used as a benchmark to speed up prototype development. It is expected that the modifications presented in this thesis will be carried out and tested experimentally.

3.1.1 Mueller-matrix laser scanning polarimeters for imaging the human retina in literature

Polarization imaging in opthalmoscopy was first used to assess the retinal nerve fiber layer *in-vivo* [64]. This novel imaging method played an important role for the early detection of blinding eye diseases particularly glaucoma, for which it was implemented in a scanning laser polarimeter for diagnosis [64, 139]. In the last few years, multiple MM polarimetric opthalmoscope designs have been implemented for imaging polarization properties of the human retina [170]. The basic setup of a polarimetric opthalmoscope consists of a light source, a polarization state generator (PSG), which generates known polarization states of input light, a polarization state analyser (PSA), which analyzes the reflected light, and a detector [36]. The PSG and PSA have the ability to modulate the polarization to unique positions on the Poincaré sphere as described in Sections 2.3 and 3.6.

A variety of methods to implement polarization modulation in MM scanning laser opthalmoscopes have been developed [64, 65, 170]. Some optical setups modulate polarization by using rotating quarter-wave plates (QWPLs) [34, 64, 101], pockel cells [139], liquid crystal modulators [33, 167, 168] or electro-optical modulators [159], enabling collection of the retinal MM. Optical setups that attempt to determine only one polarization property

of tissue, like birefrinence for glaucoma diagnosis, are often significantly simpler in terms of polarimetry. The simplicity of such setups stems from the fact that less polarization states need to be generated, enabling a simpler PSG and PSA design. In contrast, for the purpose of the AD diagnostic tool developed in Campbell labs, a full MM polarimeter is desired to enable the study of multiple polarization properties. A full MM polarimeter is realized using 16 unique, linearly independent, polarization states [97, 167, 169]. It was previously reported by Bueno et al. that depolarization is an important polarization property of ocular tissue that should be obtained during polarization imaging [38]. In addition, depolarization was reported to change as a function of various factors such as age [38]. A polarization sensitive (PS) optical coherence tomography (OCT) system for imaging the retina cannot satisfy this requirement. While OCT, as an interferometric method, provides the advantage of rejecting light that is no longer coherent when it reflects from the sample, the loss of this information prevents the PS-OCT systems from measuring depolarized light interacting with the sample [61, 97]. Another important disadvantage is that most often OCT systems have a limiting field of view (FOV), which may result in a poor diagnosis when imaging amyloid-β deposits on the retina [47, 103, 190]. Furthermore, OCT systems first obtain depth information, in the z-direction, per imaging position in the x-y plane, leading to a slower cross-sectional image (x-y plane) acquisition than SLO systems. Lastly, using an OCT may significantly increase the cost and complexity of the prototype instrument.

3.2 The donated SLO optical setup

The donated SLO is a non-mydriatic, wide-field imaging device. A collimated narrow beam of light incident on the eye's entrance pupil is focused by the optics of the eye onto the retina. The scanning unit of the SLO then raster scans the focused beam to image the retina. The scanning beam and the detection through a pinhole enable out-of-focus light and wide-angle scatter rejection. The optical setup is illustrated in Figure 3.1. The device is distinguished by four optical channels: input illumination, pinhole detection, fixation and pupil tracking channel. These four channels of the donated SLO are described in the next subsections.

3.2.1 Input illumination channel

The input illumination optical path is illustrated in Figure 3.1 starting from the input fiber to the eye. An 830 nm fiber (15-20 nm bandwidth) with a numerical aperture (NA)

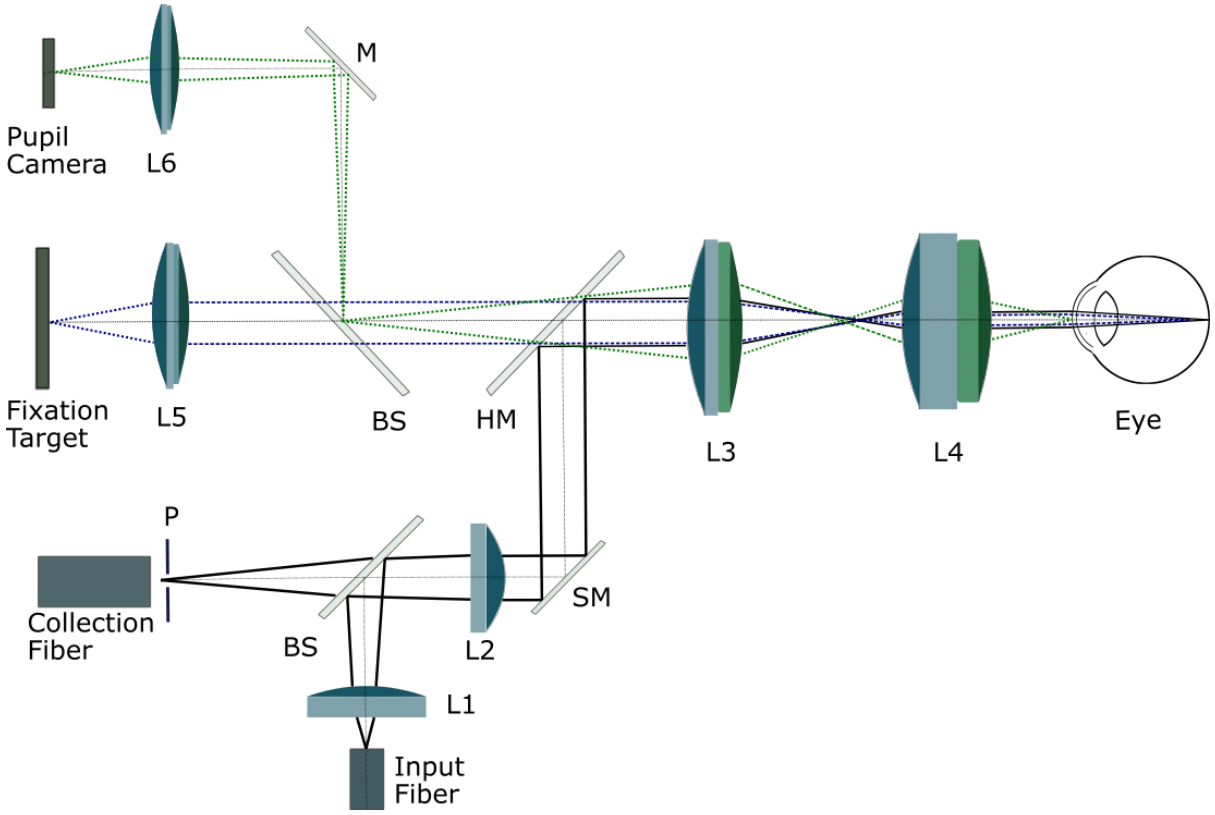

Figure 3.1: The original donated SLO. The beam path is illustrated for the central scan position. Optical components: L-lens, BS-beamsplitter, SM-scanning mirrors, HM-hot mirror, M-mirror, P-pinhole. Illustration was done with Inkscape (open-source vector graphics editor); dimensions were modified for better visualization.

of 0.12 and an output power of 10 mW is used as an input illumination source. A two-step collimator uses two lenses (Ls), L1 and L2, where L2 is optically conjugate to the entrance pupil of the eye. The illumination and detection paths are separated by a beamsplitter (BS) placed in between the two collimating lenses. The collimated beam is then directed towards the scanning unit, which consist of two galvanometric mirrors with a fast scan speed of 850 Hz and a maximum scan angle of 12.5 degrees. Then, the entrance beam is reflected off the hot mirror, set at 45 degrees and directed to the tube lens system. The hot mirror is a mirror with a filter, which reflects infrared light while transmitting visible light. The tube lens consists of two custom built lenses that de-magnify the scanning beam by 2.6 times. The collimated beam is then incident on the eye pupil, with a beam size of 0.6 mm

in diameter, and then focused on the retina by the ocular optics. The retina is scanned by changing the angle of the incident beam at the entrance pupil. However, the beam does not remain stationary between scans. Thus, the area that the incident beam covers on the entrance pupil cumulatively from all scan positions due to the walk of the beam of the pupil is approximately 2.2 mm. Thus, the donated SLO can accommodate patient pupil diameters as small as 2.2 mm. The scanning laser source offers an advantage over conventional fundus imaging since the nature of the moving spot across the retina allows for a point by point retinal exposure. Thus, the SLO setup provides more optimal light exposure to the human eye, according to the ANSI standards [67]. A further advantage of the SLO setup, which uses a scanning beam, is the improved contrast by rejecting out of focus light and wide-angle scatter, whereas fundus imaging that uses flood illumination, has no rejection of out of focus light [69, 178].

3.2.2 Pinhole detection channel

The pinhole detection optical path is illustrated in Figure 3.1 starting from the eye and ending at the collection fiber. Most of the detection channel follows the same path as the input illumination channel but in the reverse direction. Light from the retina is reflected and directed to the tube lenses, then reflected from the hot mirror (HM) onto the galvanometric mirrors, and then is directed towards the focusing lens (L2). When light is incident onto the BS, 90% of the energy will go through the beamsplitter and onto the 250 μm in diameter pinhole. Light is then directed to the collection fiber and finally incident on the avalanche photodiode (APD), a non-cooled detector with a peak sensitivity of 800 nm and a spectral response range of 400 to 1000 nm. A pinhole is placed in a retinal conjugate plane. Thus, if the pinhole is small enough it leads to the reduction of out of focus light. The size of the pinhole will be discussed in a later section of this chapter.

3.2.3 Fixation target

The human eye is constantly in motion, even during fixation [120]. Natural fixation eye movements made by a subject produce distortions during retinal imaging. These fixation eye movements can be reduced and thus the fixation target is an important aspect of instrument designs. The SLO includes a fixation target for the patient to view to minimize eye movements. The fixation target is a blue light-emitting diode (LED) source of 470 nm and 10 nm bandwidth. The fixation channel optics share some of the input illumination and pinhole detection channel optics. Light from the fixation target is projected though L5

and tube lens optical components, and is focused by the optics of the eye onto the retina. To achieve alignment of the fixation LED with the center of the scan channel, the fixation target can be translated in x and y directions.

3.2.4 Pupil tracking

A pupil tracking system is also included in the donated SLO setup. The source wavelength is a near-infrared (NIR) LED and has a power of 50 mW. The camera channel is used to determine the eye pupil position and confirm the working distance. The optical head is moved into position for tracking the eye pupil position.

3.3 Design Requirements

The commercial market for ocular imaging technologies is highly competitive and so defining design requirements that will place the MM polarimeter, that is presented in this thesis, at a competitive position in the commercial market is important. Currently, the most definitive diagnosis of AD is conducted after death by histological brain examination [46, 84] due to a lack of both specific methods for detecting neurodegenerative disorders and broadly accessible methods for screening preclinical symptoms. Although recent research has indicated that the likelihood of AD can also be determined using amyloid PET scans [93, 119], these methods are very expensive, making them primarily accessible in drug trials rather than for routine diagnosis. In addition, amyloid PET scans are invasive because they use radioactive tracers. In contrast, the MM scanning polarimeter is designed to overcome these limitations associated with existing AD diagnostic technologies, substantially decreasing the cost of examination and providing a non-invasive diagnostic method. Common with other retinal imaging technologies, pupil dilation may be used, especially, when aiming to obtain a large FOV [48, 60, 125, 160]. The system presented here is designed as a non-mydriatic retinal imaging tool that provides a large FOV. This feature places the device in the forefront of competitors, along with other wide-field retinal imaging technologies [72, 109, 125, 160].

The modified instrument should maintain an SLO footprint similar to the original one, even after polarization modules are introduced. Since the original instrument is elevated, additional optics can be placed on its base. The optical and pixel resolutions should be high enough to resolve any amyloid-β deposits in the retinas of older adults. In a traditional SLO, the image acquisition speed is limited by the scanning unit. However,

in the MM scanning polarimeter, acquisition time is also limited by the motors used in the polarization units. It is central to the design that adequate image acquisition speed must be accomplished due to the presence of fixation eye movements that can introduce drift or artifacts to the retinal images [120]. The polarization modulation unit must be repeatable and accurate, with fast modulation capability. MM polarimetry is prone to errors that can be reduced by optimizing the polarization modulation units [80, 108, 110, 168]. Polarization optics are selected based on the need for fast, repeatable and accurate polarization modulation. As in any optical device, the MM scanning polarimeter should be modular, scalable and evolutionary, especially at the prototype phase of the design.

3.4 Methods

The optical design files of the donated SLO were provided in Code V, optical design software by Synopsys. Optical design modifications, and image quality analysis presented in Section 3.5 and 3.7, respectively, were carried out using Code V. A diffraction limited eye model was used to simulate image quality on the retina to identify and correct for system aberrations. Ocular aberrations are considered in Chapter 4. Further, the optimal polarization modulation method, which is used in Section 3.5, was identified by carrying out a comparative literature review on three main polarization modulation methods in Section 3.6. Mechanical design of the PSG and PSA was carried out in Autodesk Inventor as presented in section 3.6.

3.5 Mueller-Matrix scanning polarimeter: retrofitting the polarization module in the original SLO

The MM scanning polarimeter can be realized by retrofitting a polarization module in the donated SLO. The modified optical design is presented in Figure 3.2. QWPLs were used for polarization modulation in the MM scanning polarimeter in Figure 3.2 and the explanation of this choice is presented in the following section, Section 3.6, which is based on design requirements specified in Section 3.3. Further modifications for improved image quality are described in Chapters 4 and 5.

Polarization optics were introduced in the optical design based on work by members of Campbell labs in [34, 36, 44, 68]. Since the BS separates the input illumination from the pinhole detection beam path, the PSG was placed before the BS in the incoming

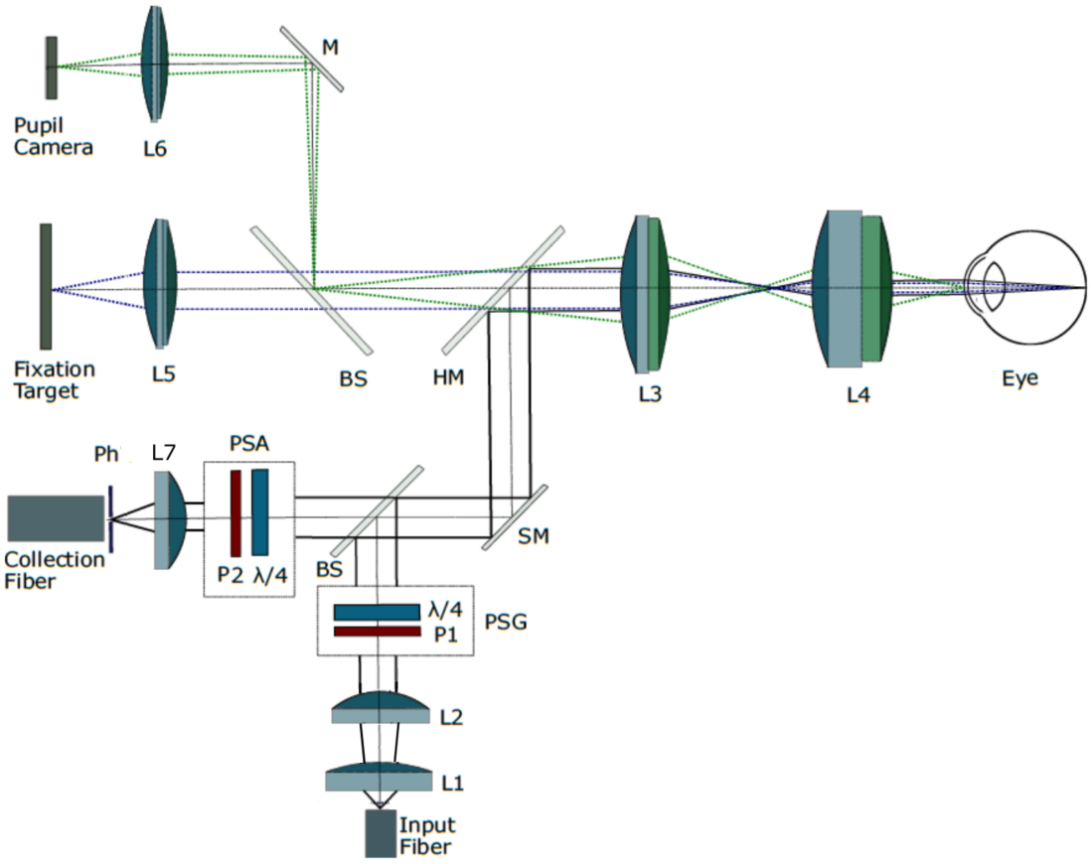

Figure 3.2: Donated SLO modified by integrating polarization modules. The beam path illustrated is for the central scan position. Optical components: M-mirror, L-lens, BS-beamsplitter, SM-scanning mirrors, HM-hot mirror, Ph-pinhole, P-Polarizer; $\lambda/4$-Quarter-waveplate unit. Illustration was done with Inkscape; dimensions were modified for better visualization.

path and the PSA was placed right after the BS in the return path. Therefore, the PSG and PSA interact with the input and reflected light sequentially. Since, it was previously reported that the retardance of a birefringent waveplate varies as a function of the incident angle of the beam, the PSG and PSA were placed in collimated space to eliminate or minimize errors related to the incident angle of light on the QWPL [79, 80]. This avoids rotation axis tip–tilt error, commonly called zenithal error [110]. Zenithal error is caused by an angular difference between the normal of the waveplate surface and the incident beam axis, and affects significantly the polarization modulation accuracy [79, 80, 110]. A

two step collimation was used to collimate the beam prior to the PSG, which is identical to the original design. Thus, the entrance pupil, scanning mirrors, PSG and PSA are optically conjugate. The optical design of the MM scanning laser polarimeter is illustrated in Figure 3.2. The input illumination and pinhole collection beam paths are illustrated in Figure 3.3 obtained from the Code V simulation. PSG and PSA, highlighted with red, are respectively comprised of a linear polarizer (LP) and a QWPL. Alternative polarization modulation methods with their advantages and disadvantages are discussed in the next section, where the selection of QWPLs for polarization modulation is justified.

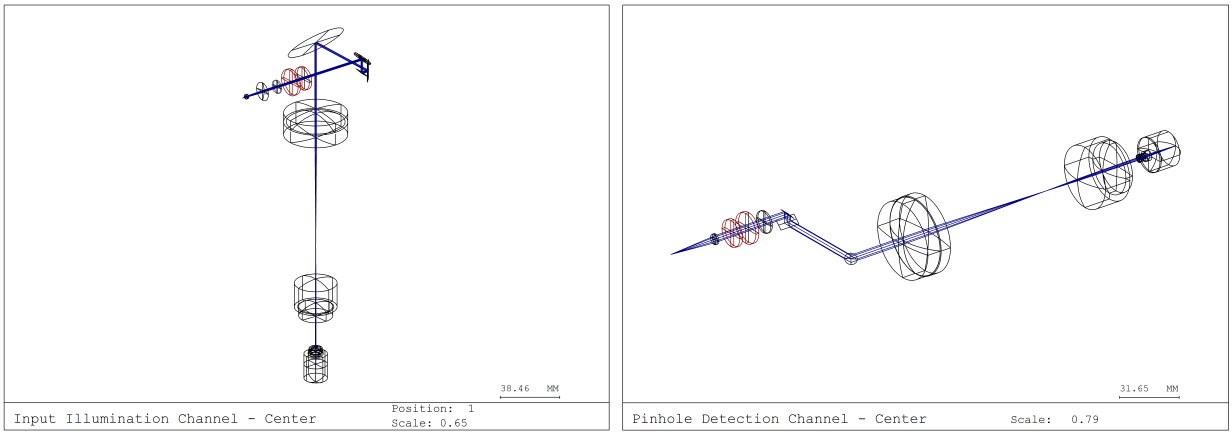

Figure 3.3: Modified input illumination and pinhole collection channel in Code V. Optical components in red are the PSG and PSA. Some dimensions were modified for better visualization.

An 830 nm fiber with a numerical aperture (NA) of 0.12 and with 10 mW output power is maintained as the input illumination source. The two step collimation lenses, formed by L1 and L2, are moved and placed before the BS. Light is then incident onto an LP followed by a QWPL as illustrated in Figure 3.2. The LP and the QWPL define the input state of polarization (SOP) that interacts with the sample of interest. The polarization unit, scanning mirrors and entrance pupil were optically conjugate. The remaining beam path that projects the light into the eye was maintained identical to the original setup. Reflected light from the retina passes through the tube lenses, is reflected from the hot mirror (HM) and directed onto the galvanometric mirrors. Reflected light is then transmitted through the BS and directed to the PSA, which is comprised by the QWPL and LP. The reflected beam was then focused onto the confocal pinhole (Ph) using L6 and detected by the APD.

3.6 Polarization modulation methods for MM retinal polarimetry: A comparative literature review

In this section, I present three polarization modulation modalities and qualitatively identify the optimal methods for polarization modulation. The three methods for polarization modulation described in this chapter are: rotating QWPL retarders, photo-electic modulators (PEMs) and magneto-optic (MO) modulators. Although liquid crystals (LCs) have been used in polarimetric setups, they are not one of the three modulation methods compared because they are characterized by slow response times and high variability in their polarization properties [30, 31, 167, 167, 169]. In addition, spatial uniformity in LCs is often poor and the retardance has a strong temperature dependence [167, 167, 169]. The optimal polarization modulation method is identified based on the design requirements presented in Section 3.3. Accurate and repeatable polarization modulation is the most important of these requirements for the selection of the optimal method. Accuracy in polarization modulators is defined as the degree to which the polarization state or point on the Poincaré sphere generated coincides with the correct state of polarization (SOP). Repeatability, is the ability of the modulator to return to the same position on the Poincaré sphere [61, 74, 86].

MM polarization imaging is an error-sensitive imaging modality [21, 108, 167, 169]. The accuracy of the MM reconstruction is reduced by error sources coupling into the measurement. Therefore, it is important to use methods that enable reduction of these errors. As described in Section 3.1.1, full MM polarimetry requires at least sixteen measurements obtained by linearly independent polarization state combinations of generator and analyzer [167, 169]. Thus, four PSG and four PSA states are required to obtain sixteen elements. Azzam et al. first discussed the optimal choice for generator and analyser SOPs. It was shown that four SOPs spaced far apart on the Poincaré sphere can reduce MM errors [21]. In addition, it was determined that the most robust MM determination is accomplished by using points that form Platonic solids in the Poincaré sphere space [108]. This was later discussed by others and it was identified that the four points far apart on the Poincaré sphere that decrease instrument errors are accomplished by a QWPL with azimuth angles of (-45, 0, 30, 60) or (-90, -45, 30, 60) degrees [5, 6, 7, 97, 168].

3.6.1 Dual rotating quarter-wave retarders polarimeter

Retarders are optical elements capable of changing the polarization of incident electromagnetic waves by causing phase lag between the two polarization states, E_x and E_y

[86]. Polarization modulation using a wave retarder or waveplate (WPL) is accomplished by rotating the WPL around the optical axis of the incident beam. The retardance, $\Delta\phi$, is defined as the absolute phase difference of the fast and slow axis, calculated as $\Delta\phi = |\phi_{\text{fast}} - \phi_{\text{slow}}|$. A QWPL is an optical element that introduces a relative shift of $\Delta\phi = \pi/2$ [86, 97].

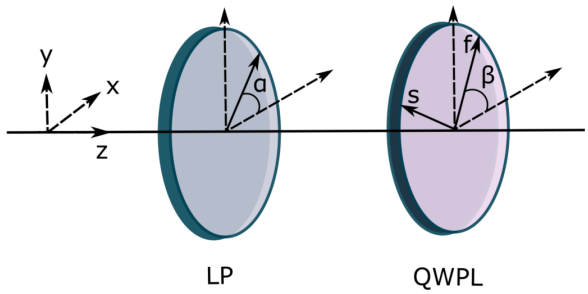

Figure 3.4: Polarization state generator. Light traveling in the horizontal direction interacts with the linear polarizer (LP) and quarter-wave plate (QWPL). Light travels from left to right in the z-direction. Adapted with permission from [20] © The Optical Society.

Polarization modulation can be accomplished by using a LP followed by a QWPL. In this setup, the LP has transmission-axis azimuth angles, α and the QWPL has fast-axis azimuth angles, β as illustrated in Figure 3.4. By rotating the LP and keeping the QWPL constant, points along the surface of the circle on the equator of the Poincaré sphere are accessed, representing linear polarization states. By keeping the LP at a constant azimuth angle and rotating the QWPL at a variable azimuth angle, β, the SOP is modulated at various points on the Poincaré sphere. One of the first polarimeter setups capable of measuring all sixteen elements of the MM of an optical system was developed by Azzam using rotating QWPLs [19]. Rotating QWPL MM polarimetry was also implemented for identifying *in-vivo* birefringence of the human foveal area [65, 101]. The implementation of the polarization modulation units using dual rotating QWPLs is illustrated in Figure 3.5. Input light passes through a LP to obtain linearly polarized light, which is then modulated to other SOP by using a rotating QWPL [65]. Using a scanning unit, polarized light is directed to various locations on the retina and reflected light is then directed to the PSA which passes though the rotating QWPL and stationary LP.

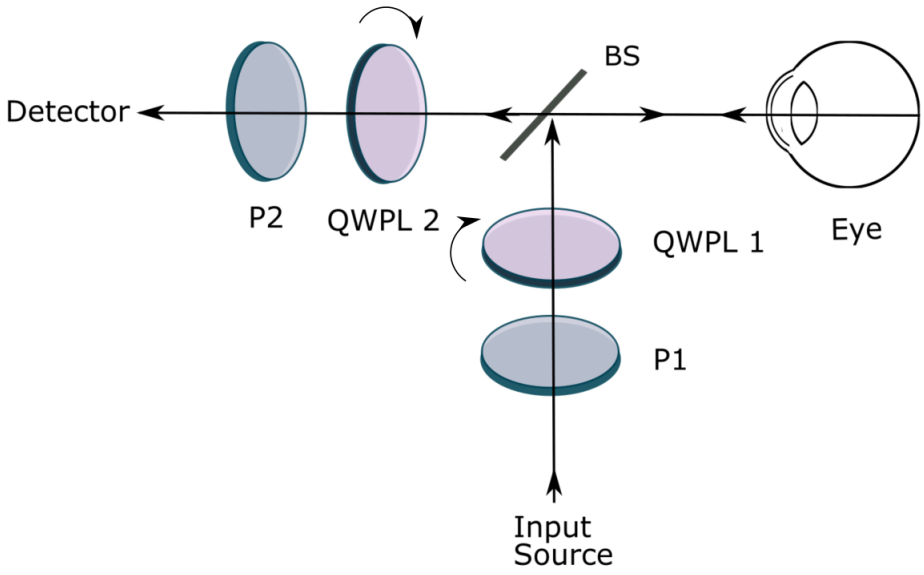

Figure 3.5: MM scanning laser polarimeter using rotating QWPLs. The PSG and PSA are comprised by a LP and a QWPL which rotates to 4 positions. Adapted with permission from [34] © The Optical Society.

SOP on the Poincaré sphere using rotating QWPL setup

The mathematics of how the SOP changes using a LP and rotating QWPL arrangement in the MM polarimeter was described using the Stokes–Mueller calculus presented in Chapter 2 [15, 20, 97]. All possible SOPs on the Poincaré sphere that can be accessed using this setup are illustrated in Figure 3.6. These SOP points were determined by simulating the possible stokes vectors derived in Equation 3.1, which were determined by taking the consecutive product of unpolarized light $\begin{pmatrix}1 & 0 & 0 & 0\end{pmatrix}^{\mathrm{T}}$, the MM of a LP, M_{LP}, and the MM of a QWPL, M_{QWPL} [15, 97]. In the following equations the variable azimuth angle, β, of the rotating QWPL is symbolized by θ. These points were previously described as a figure-eight contour on a hemisphere with mirror symmetry along the equatorial plane [20]. This indicates that with a LP and a rotating QWPL, one can generate states on the Poincaré sphere that are spaced far apart, which is an essential requirement of MM polarimetry for error minimization [20, 168, 169].

$$S(\theta) = \begin{pmatrix} 1 & 0 & 0 & 0 \end{pmatrix}^{\mathrm{T}} M_{\mathrm{LP}} M_{\mathrm{QWPL}} \tag{3.1}$$

$$= \begin{pmatrix} 1 & 0 & 0 & 0 \end{pmatrix}^{\mathrm{T}} \frac{1}{2} \begin{pmatrix} 1 & 1 & 0 & 0 \\ 1 & 1 & 0 & 0 \\ 0 & 0 & 0 & 0 \\ 0 & 0 & 0 & 0 \end{pmatrix} \begin{pmatrix} 1 & 0 & 0 & 0 \\ 0 & cos^2(2\theta) & cos(2\theta)sin(2\theta) & -sin(2\theta) \\ 0 & cos(2\theta)sin(2\theta) & sin^2(2\theta) & sin(2\theta) \\ 0 & sin(2\theta) & -cos(2\theta) & 0 \end{pmatrix} \tag{3.2}$$

$$= \frac{1}{2} \begin{pmatrix} 1 & cos^2(2\theta) & cos(2\theta)sin(2\theta) & sin(2\theta) \end{pmatrix} \tag{3.3}$$

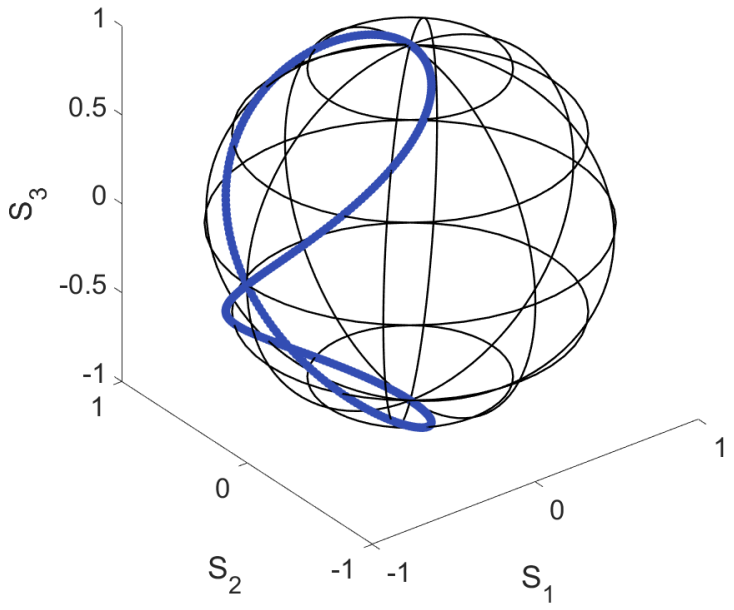

Figure 3.6: SOP illustrated on the Poincaré sphere using a LP and a rotating QWPL. Possible states of polarization (SOPs) are traced on the surface of Poincaré sphere and were obtained from $\theta = 0$ to 2π. The SOPs trace a figure-eight type trajectory. Modeled in Matlab.

Implications of polarization modulation using dual rotating QWPLs

Polarization modulation of quasi-monochromatic light in MM polarimeters using rotating QWPLs has been used for many years, providing reliable results [15, 20, 25, 65, 92, 101]. Using rotating QWPLs has the advantage of being a simple method for polarization modulation, and can be implemented in free space optics. Since the optical components used in this modulation method are widely available from multiple manufacturers, the cost of the device can be reduced, and low footprint options are available.

Since in this optical setup the QWPL must be rotated to obtain different polarization states, a rotational stage needs to be used. Therefore, the main limitation of this method was the rotation of the QWPL in free space, which can introduce errors and cause slow image acquisition times. Compact high speed rotational stages are commercially available but errors can be introduced by stopping the QWPL at the four required positions. This is because it is difficult to continuously rotate the QWPL fast enough and to stop rapidly at an accurate and repeatable position. Thus, the presence of rotational errors limits accuracy and repeatability. Minimizing rotational related errors while keeping high rotational speed may lead to significantly increasing instrument cost.

3.6.2 Photoelastic modulator polarimeter

Dual photoelastic modulator (PEM) systems are also widely used to modulate polarization [56]. Jasperson and Schnatterly presented the first Photoelastic modulator polarimeter [94]. Since then, other research groups have introduced variations in the original setup to improve the design [56, 96, 98, 108]. The PEM consist of a piezoelectric transducer and an optical element. A current is applied to the transducer which vibrates the optical element, inducing stress. The stress changes the birefringence of the transparent optical element causing change in the polarization state of light interacting with the crystal [96]. The implementation of the polarization modulation units using dual PEMs is illustrated in Figure 3.7. Polarization modulation using a single PEM can rotate the SOP around one of the axis of the Poincaré sphere. A PSG using a LP followed by two PEMs with two different orientation axes can modulate the SOP along any point on the Poincaré sphere as determined by sterographic projection and proven in the next section. In the optical setup, the LP is orientated with a transmission axis set to 0 degrees and is then followed by the two PEMs with retardance Δ and fast axes at azimuth angles of 45 and 0 degrees, respectively as illustrated in Figure 3.7.

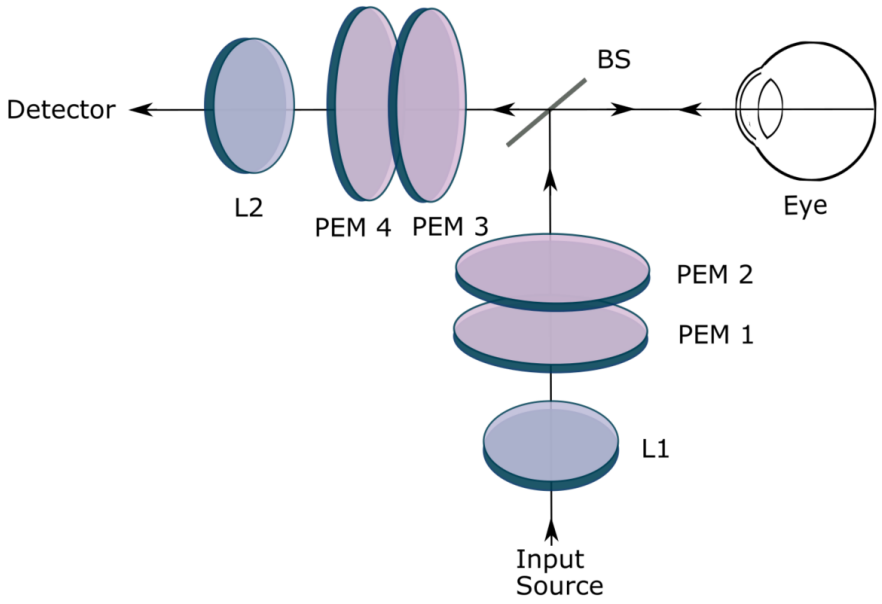

Figure 3.7: MM scanning laser polarimeter using dual PEMs. The PSG and PSA are comprised by a LP and two PEMs. Adapted with permission from [34] © The Optical Society.

SOP on the Poincaré sphere using dual PEMs

The mathematics of how the SOP changes using a LP and dual PEM arrangement in MM polarimetry was described using the Stokes–Mueller calculus presented in Chapter 2 [15, 20]. All possible SOPs on the Poincaré sphere that can be accessed using this setup are illustrated in Figure 3.8. These SOP points were determined by simulating the possible Stokes vectors derived in Equation 3.4, which were determined by taking the consecutive product of unpolarized light $\begin{pmatrix} 1 & 0 & 0 & 0 \end{pmatrix}^{\mathrm{T}}$, the MM of a horizontal LP, M_{LP}, and the MM of each PEM, M_{PEM}, [97, 169]. The LP has a transmission axis set to 0 degrees, the first PEM has a retardance Δ_1 and fast axis azimuth angle of 45 degrees, $\beta_1 = 45°$, and the second PEM has a retardance Δ_2 and fast axis azimuth angle of 0 degrees, $\beta_2 = 0°$. This indicates that with a LP and two PEMs one can generate all the SOP on the Poincaré sphere [20].

$$S(\theta) = \begin{pmatrix} 1 & 0 & 0 & 0 \end{pmatrix}^{\mathrm{T}} M_{\mathrm{LP}} M_{\mathrm{PEM}\,1}(\beta_1 = 45°) M_{\mathrm{PEM}\,2}(\beta_2 = 0°) \tag{3.4}$$

$$= \begin{pmatrix} 1 & 0 & 0 & 0 \end{pmatrix}^{\mathrm{T}} \frac{1}{2} \begin{pmatrix} 1 & 1 & 0 & 0 \\ 1 & 1 & 0 & 0 \\ 0 & 0 & 0 & 0 \\ 0 & 0 & 0 & 0 \end{pmatrix} \begin{pmatrix} 1 & 0 & 0 & 0 \\ 0 & cos\Delta_1 & 0 & -sin\Delta_1 \\ 0 & 0 & 1 & 0 \\ 0 & 0 & sin\Delta_1 sin45 & cos\Delta_1 \end{pmatrix} \begin{pmatrix} 1 & 0 & 0 & 0 \\ 0 & 1 & 0 & 0 \\ 0 & 0 & cos\Delta_2 & sin\Delta_2 \\ 0 & 0 & -sin\Delta_2 & cos\Delta_2 \end{pmatrix} \tag{3.5}$$

$$= \frac{1}{2} \begin{pmatrix} 1 & cos\Delta_1 & sin\Delta_1 sin\Delta_2 & sin\Delta_1 cos\Delta_2 \end{pmatrix} \tag{3.6}$$

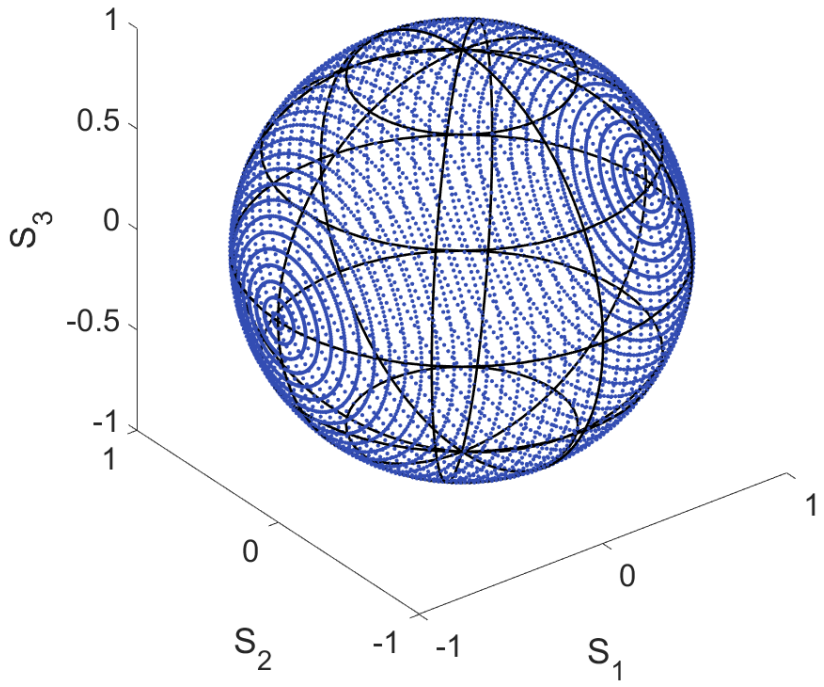

Figure 3.8: SOP illustrated on the Poincaré sphere using a LP and dual PEMs. Possible states of polarization (SOPs) are traced on the surface of Poincaré sphere and were obtained from $\Delta = 0$ to 2π. The SOPs trace a figure-eight type trajectory. Modeled in Matlab.

Implications of polarization modulation using PEMs

The PEM retarder is similar to a QWPL because it has a fixed retardance axis, with a rotational angle, resulting in sinusoidally varying retardance values. In contrast to the rotating QWPL setup, there are no mechanically rotating components which in some cases results in improved signal stability and accuracy. Compared to the other polarization variable retarders such as Faraday rotator and liquid crystal variable retarder, PEMs are far more powerful because they have high modulation frequencies [174].

However, modulation of polarization using PEMs is prone to phase errors [98, 108]. The high dependence of PEMs on tempurature can also introduce significant drift in the SOP [96]. PEM modulation of SOP was determined to have variable accuracy and repeatability which was evaluated experimentally in the lab by me and another lab member, Peter Neathway. Using a PEM from General Photonics Inc. the accuracy and repeatability for a 0 degree LP state and right hand circularly polarized (RCP) states were tested. Repeatability was determined by the ratio of the standard deviation of the measured state and the square root of the number of measured states, which is the standard deviation of the mean, and was determined to be 0.14 and 0.2053 degrees for LP(0) and RCP, respectively. Accuracy, which is the closeness of the measurements to a specific SOP value was measured by the difference between the mean values of the SOP to the actual state and was determined to be 0.16 and 0.538 degrees for LP(0) and RCP, respectively. In addition, there was a high degree of drift observed that was also reported by previous authors [96, 98, 108]. Therefore, while PEMs have the advantage of high polarization modulation speed, and do not require rotating components, they lack the desired accuracy and repeatability for *in-vivo* retinal imaging that will be used as a diagnostic tool.

3.6.3 Magneto-optical polarimeter

Polarization modulation with magneto-optical (MO) modulators operates using the MO effect. The MO effect is a result of the interaction of an electromagnetic wave with a diamagnetic crystal, where in the presence of a magnetic field, the polarization state of light changes. MO modulators are realized using MO crystals which become optically anisotropic by applying an external magnetic field causing a change in the permittivity, which leads to a refractive index change [132]. The optical axis of this induced optical activity is aligned with the axis of the applied magnetic field. While this phenomenon has been known for many years, it has only recently been developed and become commercially available for polarization modulation [51, 132]. In theory by using a LP followed by two magneto-optic modulators with rotation axes aligned to two axis of the Poincaré shpere

the SOP can be modulated to any state on the sphere, similar to the PEM polarimeter [51, 188]. General Photonics Inc. has developed the first commercially available all solid-state PSG that uses magneto-optic polarization rotators for MM polarimetry. This device can generate six unique polarization states across a Poincaré sphere and repeatability was reported to be better than 0.1 degrees [188]. The implementation of the polarization modulation units using MO modulators is illustrated in Figure 3.9. Input light passes through a LP to obtain linearly polarized light, which is modulated by the MO modulator. Using a scanning unit, polarized light is directed to various locations on the retina and reflected light is then directed to the PSA which passes though the rotating MO modulator and polarizer [188].

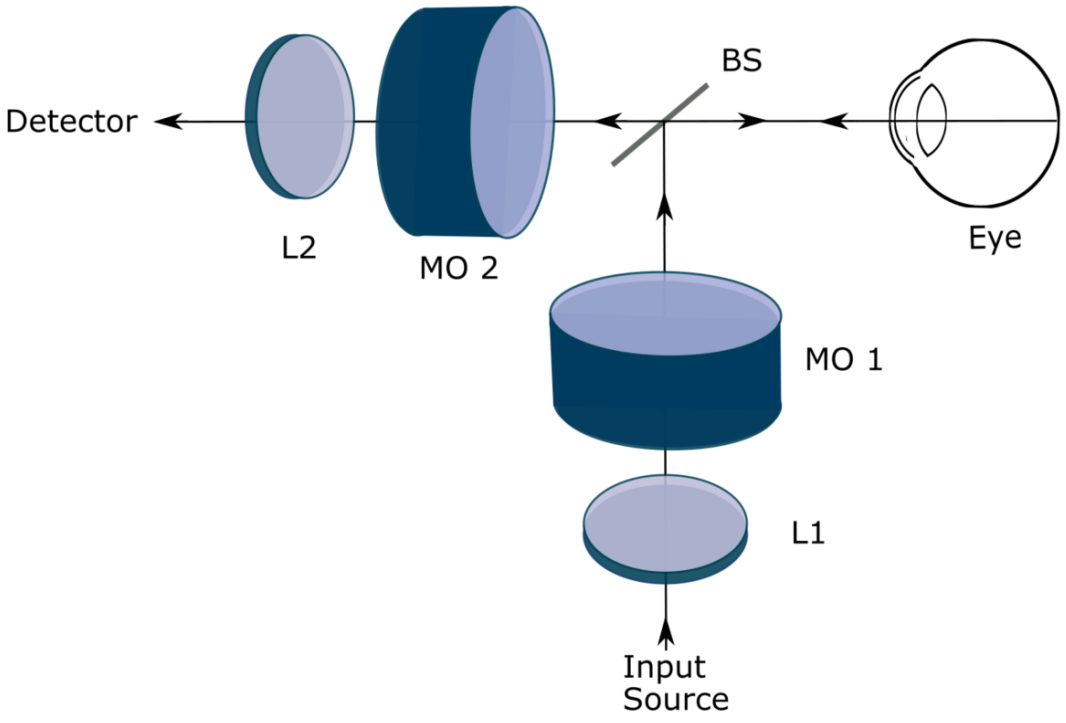

Figure 3.9: MM scanning laser polarimeter using MO modulators. The PSG and PSA are comprised by a LP and a MO modulator. Adapted with permission from [34] © The Optical Society.

SOP on the Poincaré sphere using dual MO modulators

The mathematics of how the SOP changes using a LP and MO modulator arrangement in MM polarimetry were described using the Stokes–Mueller calculus presented in Chapter 2 [15, 20]. All possible SOPs on the Poincaré sphere that can be accessed are identified using the exact same mathematics as the PEM arrangement in Section 3.6.2. If a LP and two MO optical modulators were used with a magnetic field applied causing a fast axis azimuth angle of 45 degrees, $\beta_1 = 45°$, and followed by a second MO modulator, which has a retardance with a fast axis azimuth angle of 0 degrees, $\beta_2 = 0°$, then all SOPs on the Poincaré sphere can be accessed. However, this option is not commercially available yet. Since an MO modulator are only commercially available as a complete device from General Photonics Inc., the possible SOPs on the Poincaré sphere are illustrated in Figure 3.10 for this device. It was determined that MO modulation was highly repeatable, and the measured solid angle repeatability was better than 0.1 degrees [188]. The MO modulator can access six polarization states including 0 degrees, ±45 degrees, 90 degrees, LHC and RHC across a Poincaré sphere as illustrated in Figure 3.10.

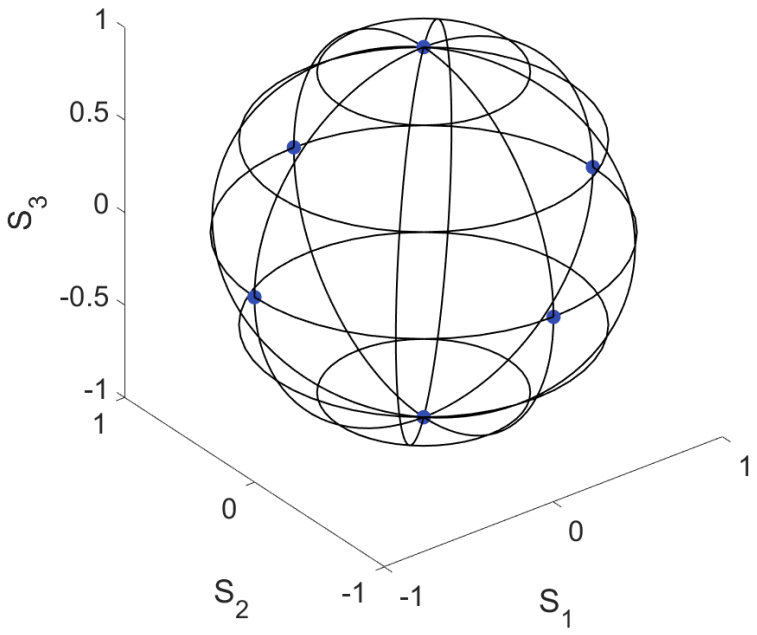

Figure 3.10: Possible states of polarization (SOPs) are illustrated on the Poincaré sphere using a MO modulator by General Photonics.

Implications of polarization modulation using dual MO modulators

The advantage of MO modulation includes the fact that it is a solid state device without being limited by rotating components, and has the ability to change the SOP almost instantaneously. The predictable wavelength and temperature dependence is another important advantage of MO modulators [188]. Due to the binary nature of the magneto-optic crystal, the magnetic field can be controlled by the electric circuit of the device that is already optimized to generate the magnetic field required for the six SOPs. This enables easier MO modulation implemented than PEMs and QWPLs. Other advantages include that the polarization unit is realized with free space optics and is characterize by fast response times. The lack of mechanically rotating components also improves the design with compact, fast, superior repeatability and stability.

The main limitation of this modality is that it is only available for communication wavelengths and not the 830 nm wavelength used in the instrumentation presented in this thesis. This is because the Verdet constant, which describes the strength of the magnetic field, is proportional to the wavelength. Another limitation of this method is that the MO modulator by General Photonics Inc. does not include elliptical SOPs. While it is possible to obtain a full MM, the lack of elliptical polarization is not ideal, as suggested by the optimal SOPs suggested in [5, 6, 7, 97] .

3.6.4 Optimal Polarimetric modulation method via QWPLs: a novel implementation

Accurate, repeatable and fast polarization modulation is crucial to the instrumentation of the MM scanning polarimeter that will be used as a diagnostic tool for AD. Three methods were described above and characterized in order to identify the optimal methods based on requirements presented in Section 3.3. Rotating QWPLs are the simplest to implement but introduce significant rotational related errors. On the other hand, PEMs and MO modulators are not limited by rotating components and thus they are generally described as more accurate and repeatable [168]. However, PEMs were found to lack high accuracy and repeatability, introduced retardation drifts, and are most commonly implemented using fiber optics. Implementation with fiber optics was avoided because optical fibers are known not to preserve the SOP of the light passing through them, which is central to the instrumentation [133, 147]. Among the three methods, MO modulation provided the most accurate, repeatable and fast polarization modulation. Further MO modulators can be implemented in free space optics and have a small footprint. However, the commercially available MO modulator cannot be used because it is only developed for

communication wavelengths and not for imaging wavelength of the 830 nm. Therefore, the optimal methods for polarization modulation is using QWPLs, determined by the process of elimination. In addition, it is possible to further optimize the QWPL setup to reduce or eliminate errors related to rotation. As a result of this requirement, a linear optical holder for four QWPLs was designed to replace the rotating motor. The four QWPL holder is illustrated in Figure 3.11. Each QWPL is mounted into a specific orientation. The linear holder moves in and out of the beam path using a linear actuator.

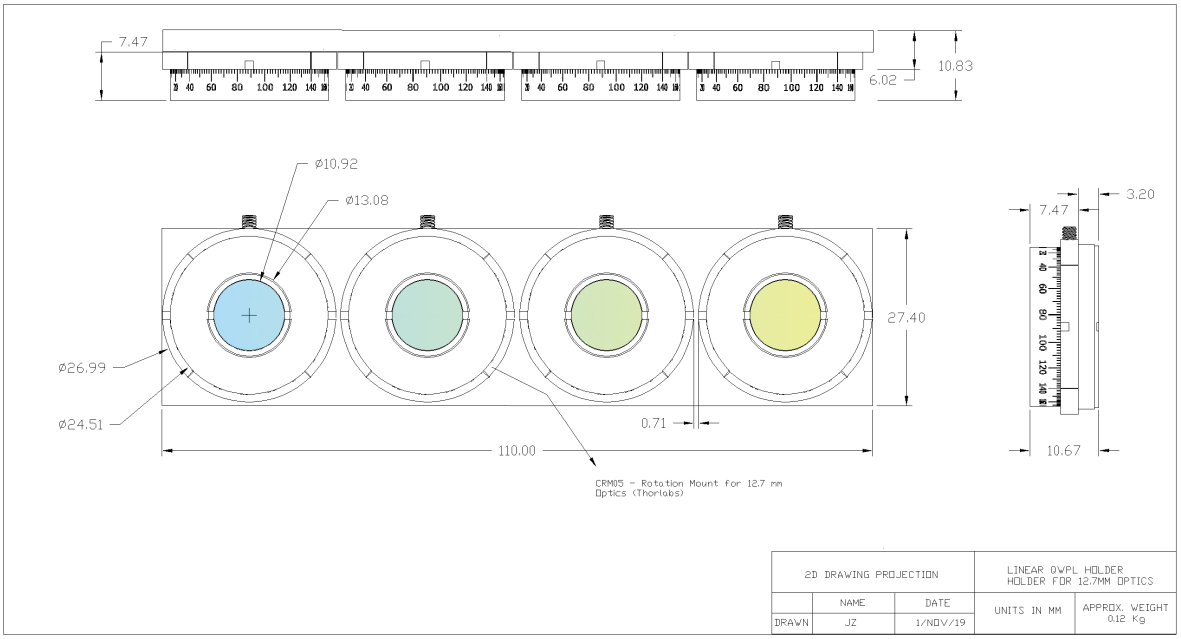

Figure 3.11: Linear holder with four QWPLs used for polarization modulation in the PSG and PSA. Each QWPL position is colour-coded indicating the four orientations of the QWPLs. The linear holder is connected to a linear actuator which moves the linear holder in and out of the beam path. The placeholder for each QWPL is a threaded continuous rotation mount by Thorlabs (CRM05) that can be integrated into the linear holder design for accuracy. Designed in AutoCAD Inventor

Apart from the advantage of removing all rotational components, the polarization modulation speed can be improved without additional errors. This is because a linear actuator of high speed can be used without concern for the exact position of the linear actuator during each of the sixteen measurements. In other words, using a QWPL that is larger than the beam leads to small inaccuracies in positioning do not affect the polarization

state. Lastly, this method allows customization of the size of the linear holder, enabling a compact implementation of PSG and PSA. The linear holder illustrated in Figure 3.11 is designed for commercially available QWPLs, but can be easily modified to custom sized QWPLs.

3.7 Image quality and polarization analysis

The performance of the MM scanning polarimeter was assessed by image quality and polarization ray-tracing analysis. The optical design files of the input illumination and pinhole detection channels were supplied in Code V and polarization optics were introduced in the design as described in Section 3.5. A diffraction-limited eye model was implemented to assess optical resolution in the MM polarimeter. The FOV, pixel resolution and pinhole size were also identified. Another important performance characteristic, the scanning speed was assessed which affects image quality due to fixation ocular eye movements [120]. Polarization ray tracing and transmission analysis was used to identify the effect of polarization optics in the beam path. Lastly, modifications are discussed to further improve the design.

3.7.1 Optical resolution

The spatial resolution of a traditional SLO is determined by different factors including wavelength, and entrance pupil size incident on the eye [177]. In a traditional SLO when the entire eye pupil is used as an exit pupil, the input illumination beam determines resolution. However, the donated SLO was found to not follow a conventional SLO design. The donated SLO has a small entrance beam that causes a large diffraction blur on the retina. This uniform illumination of the retina resembles a Maxwellian-view system. In a Maxwellian-view system, the illumination beam is focused on the pupil of the eye, and uniformly illuminates the retina [39]. Unlike the Maxwellian-view system, the donated SLO de-magnifies the entrance beam using a tube lens resulting in a 0.6 mm collimated entrance beam incident on the eye and results in a large, diffraction-limited Airy disk with a radius on the retina of 28 μm. This highly defocused spot is then scanned along the entire FOV creating uniform illumination on the retina with time. According to this analysis in Code V and simulation in Matlab, the point spread function (PSF) on the retina for each scan position is large. This large diffraction spot significantly overlaps adjacent PSFs as a function of time. The simulated result of this uniform illumination on the retina is illustrated in Figure 3.12, where the illumination is uniform except at the edges.

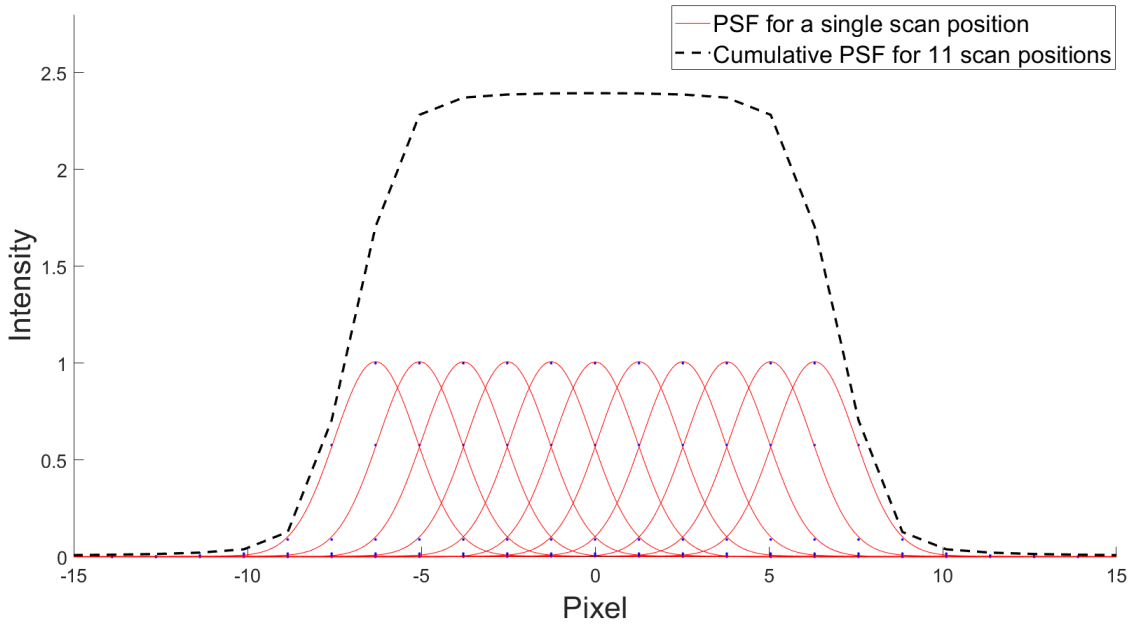

Figure 3.12: Point spread function (PSF) at each scan position and the superposition of these PSFs with time, which results in uniform illumination as indicated by the dashed line. Simulation in Matlab.

In this SLO with a small entrance pupil the optical resolution is dependent on the second-pass or return beam path of light leaving the eye [148], and the mathematics of this conclusion are further derived in Section 5.3.2. This image quality is thus dependent on the exit pupil in the return path. The exit pupil of the donated SLO is determined by the clear aperture of the collection lens, L7. However, there is an additional constraint in the donated instrument which is the collection fiber acceptance angle that further constrains the beam. Therefore, the reflected light from the retina passes the ocular optics and then the instrument optics where the beam is constrained first by the collection lens, L7 and then by the pinhole whose aperture is set to ensure maximum collection angle for the detection fiber. The pinhole is then the effective exit pupil of the system. The MTF on the retina from the second pass using a diffraction limited eye is illustrated in figure 3.13 where the cutoff frequent is 124 cycles/mm. Thus the diffraction blur on the retina due to the exit pupil, which corresponds to the system optical resolution, was equivalent to be $9.8\mu m$.

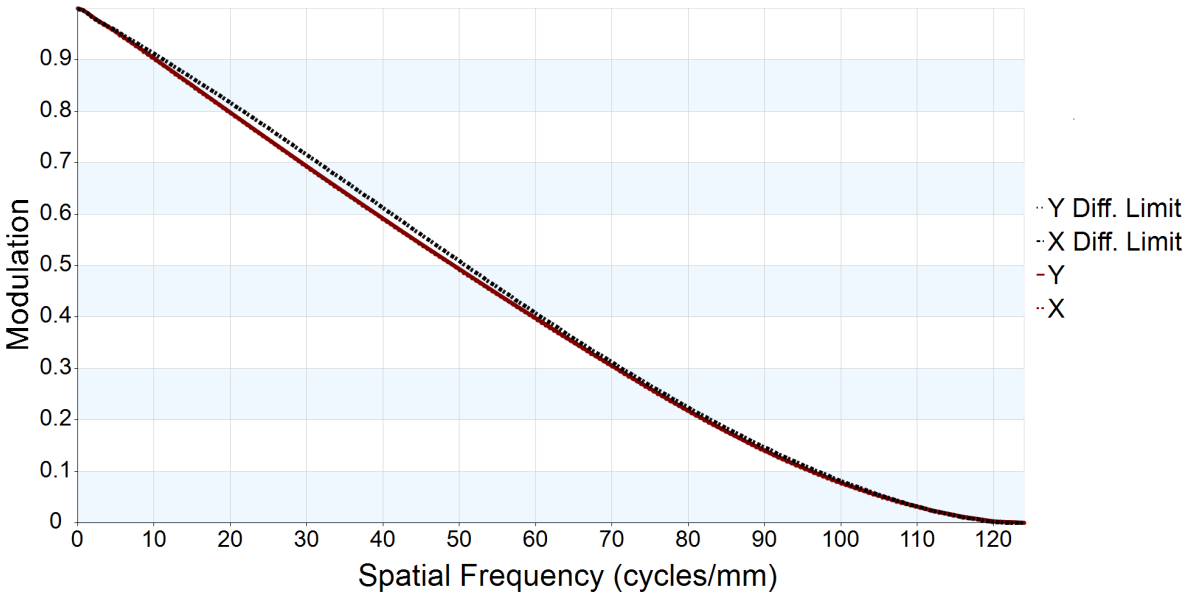

Figure 3.13: Modulation transfer function on the retina obtained from the return beam path leaving the eye

3.7.2 Field of view

The peripheral retina and its vasculature is of major importance in a variety of conditions including AD [8, 109, 125, 184]. Traditional fundus photography uniformly illuminates the retina and is capable of acquiring 30 to 60 degrees FOV, whereas initial SLO designs usually had a FOV less than 30 degrees [8, 107, 109, 125, 184]. Staurenghi et al. have used a widefield lens accomplishing an increase in FOV [160]. Further, innovative approaches have reached 100 degrees FOV using modified fundus photography or an SLO setup. The two leading widefield SLOs currently on the market are the Optos and the Heidelberg Spectralis HRA system and can accomplish from 100 to 200 degrees FOV [109, 125, 184]. The Heidelberg ultra widefield (UWF) module uses a non-contact removable lens which is attached on the camera head of the Heidelberg cSLO, expanding the FOV [184]. In contrast, the Optos fundus camera uses an ellipsoidal mirror that permits visualization of up to 200 degrees of the retina [109, 125].

Widefield imaging in the donated SLO is accomplished by using two custom-made lenses that form a telescope, which de-magnify the incoming beam scanned on the retina. The one dimensional FOV of the donated SLO measured at the nodal points of the eye

is the product of telescope magnification and maximum optical scan angle, as described by Izatt in [107]. Telescopes that de-magnify the entrance beam incident on the eye also magnify scan angles [107]. Therefore, the FOV is described by equation 3.7 calculated by the product of the maximum scan angle and angular magnification:

$$FOV = M \cdot \theta = 2.6 \cdot 25^\circ = 65^\circ \tag{3.7}$$

In traditional SLO optical setups there is a trade-off between the FOV and resolution. By maximizing magnification the beam size is de-magnified, which causes a larger diffraction blur on the retina due to the small entrance beam size on the eye. However, in the donated instrument optical resolution is not impacted by the large magnification of the tube lens as optical resolution is determined by the second pass.

3.7.3 Pixel resolution

Pixel resolution is equivalently as important as optical resolution and they are usually matched. The pixel size is found to be $9.46\mu m$ from equation 3.8. The pixel resolution is commonly double the pixel size and is determined in equation 3.9 as 18.9 μm.

$$\text{Pixel Size} = \frac{FOV \times f_0}{\text{pixels}} = \frac{1.134rad \times 16.67mm}{2000\text{pixels}} = 9.456\,\mu m \tag{3.8}$$

$$\text{Pixel Resolution} = 2 \cdot \text{Pixel Size} = 18.9\,\mu m \tag{3.9}$$

3.7.4 Confocal pinhole

The donated SLO has a pinhole, which is placed in front of the detector at a nearly conjugate plane to that of the retina. In traditional SLO setups a small pinhole can block light that is reflected or scattered by structures at different axial or lateral positions. Therefore, the pinhole attenuates light that would degrade the final image [107]. The pinhole can be expressed in terms of the times-diffraction-limited (TDL) spot size as described by Izatt in [107]. The TDL spot size is calculated by dividing the pinhole size with the Airy disc diameter as indicated in equation 3.10 [107]. In this equation, the pinhole and Airy disc sizes are projected onto the same plane, either the retinal plane, which is a pinhole conjugate plane, or the pinhole plane.

$$TDL = \frac{\text{Pinhole size}}{\text{Magnification} \times \text{Airy disc diameter}} \tag{3.10}$$

To determine the TDL on either plane the system magnification needs to be first characterized. The magnification of the system originates from the tube lens, which can be determined by taking the ratio of the focal lengths of the two lenses, L3 and L4, or by taking the ratio of the incoming and outgoing beam diameter from the tube lens. The magnification was determined from Code V to be $M_1 = 2.6$. There is also magnification caused by the eye's optics and the collection lens, L7, placed before the pinhole and was measured to be approximately $M_2 = 1.8$. The total magnification was determined to be approximately $M_{total} = M_1 \times M_2 = 4.65$. The donated SLO has a pinhole diameter of $250\mu m$. The Airy disk diameter on the retina from the output beam, which determines the optical resolution in the SLO with a small entrance pupil, was determined to be $19.6\mu m$, resulting in a TDL of 12.76.

Thus, the pinhole size is large and does not contribute much to the rejection of out-of-focus light. However, even in this large pinhole/detector setup the SLO can reduce out of focus or wide-angle scattered light due to the use of a scanning beam as described in [149]. Furthermore, wide-angle scattered light produces a wide-angle component compared to the PSF calculated from diffraction and refraction, which may be attenuated using an intermediate sized detector [149].

3.7.5 Scanning speed and eye movements during fixation

Traditionally in SLO systems, a fixation target is used to minimize patient eye motion during examination. By placing a dichroic mirror in the optical path the fixation pattern is imaged onto the retina. While people can focus at a visual target for extended periods of time, there are involuntary eye movements present even during fixation [120, 162]. Fixation eye movements are small movements of the eyes, which ensure that vision stays clear, and does not fade during a task that requires fixation [120]. These eye movements refresh images on retinal by preventing sensory adaptation. There are three main types of eye movements that are studied during fixation including tremor, drifts and microsaccades [120]. Tremors are the smallest eye movements while drift and microsaccades are the largest. While image calibration can be done afterwards, optimizing the fixation target to minimize involuntary eye movements during fixation can decrease the amount of image processing required afterwards [162]. As described in Section 3.2 the SLO uses galvonometric scanners to scan the retina. The retina is scanned with a fast line scan rate of 850 Hz providing a 2k$\times$ 2k image. The factor of two in the following equations is due a forward followed by a reverse scan in every cycle.

$$\tau_{\text{Line Scan}} = \frac{1}{2 * f} = \frac{1}{2 * 850} = 0.59\, ms \tag{3.11}$$

$$\tau_{\text{Pixel}} = \frac{\tau_{\text{Line Scan}}}{2000} = \frac{0.59}{2000} = 0.29\, \mu s \tag{3.12}$$

$$\tau_{\text{Image}} = \tau_{\text{Line Scan}} \times 2000 = 1.18\, s \tag{3.13}$$

The acquisition time of a single 2k × 2k image was calculated to be 1.18s for a 65 degree FOV measured from the nodal point. Since sixteen images have to be taken for the MM polarimetry analysis, the total acquisition time of an image set is at least 18.9s. The fastest microsaccade movement was documented at 97$\frac{deg}{s}$ and the average duration of a microsaccade is 25 ms and highest duration of 30 ms [120]. As determined in Equation 3.14, the imaged retina features moves approximately by 90 pixels during a line scan, which is likely to degrade part of a single line.

$$d_{\text{microsaccade}} = \quad 30ms \quad \times \quad 97\frac{deg}{s} = 2.91 \;\; deg = 846.6 \;\; \mu m = 90 \;\; pixels \tag{3.14}$$

Tremors had significantly slower rate than microsaccades. The fastest tremor was 20 $\frac{arcmin}{s}$ which is 0.33 $\frac{deg}{s}$, and the maximum reported duration is 1 s [120]. As determined in Equation 3.15, the imaged retina features move approximately 11 pixels during acquisition of a single frame, which is likely to introduce a small amount of degradation.

$$d_{\text{tremor}} = \quad 1s \quad \times \quad 0.33\frac{deg}{s} = 0.33 \;\; deg = 96 \;\; \mu m = 11 \;\; pixels \tag{3.15}$$

The fastest drift was reported to be 30 $\frac{arcmin}{s}$ which is 0.5 $\frac{deg}{s}$, and the maximum reported duration is 1 s [120]. As determined in Equation 3.16, the imaged retina features move approximately 15 pixels during acquisition of a single frame, which is likely to introduce a small additional amount of degradation.

$$d_{\text{drift}} = \quad 1s \quad \times \quad 0.5\frac{deg}{s} = 0.5 \;\; deg = 145.5 \;\; \mu m = 15 \;\; pixels \tag{3.16}$$

The equations presented give an estimate of the maximum displacements of an imaged retinal featured during a line scan or full image acquisition. It is evident that microsaccades, "the small, fast, jerk-like eye movements" that occur during involuntary fixation may pose a small problem [120]. Therefore, a fixation target that can minimize microsacades could improve the quality of the images acquired.

3.7.6 Polarization ray tracing

The four optimal rotation angles using QWPLs for a MM polarimetry were previously determined [7]. It was recommended that an angle set of (-45, 0, 30, 60) degrees or (-90, -45, 30, 60) degrees should be used to reduce polarization related errors and fluctuations in the detected intensity [7, 97]. These states convert light to circular polarized, linear and elliptical polarized light. Code V has the ability to track the polarization state of light in the beam path and on the image plane. Figure 3.14 illustrates the four polarization states generated by the PSG and projected on the retina.

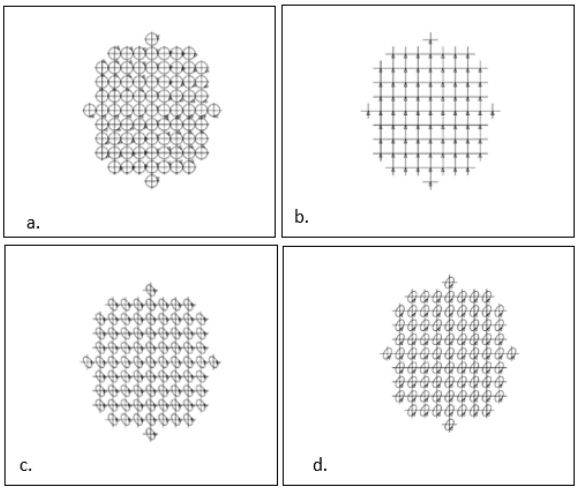

Figure 3.14: Polarization states on the retinal generated by the four PSG orientations: a. $-45°$, b.$0°$, c.$30°$, d.$60°$; using an eye model that does not alter the polarized light states.

Transmission characteristic analysis

The light source of the confocal scanning polarimeter has a central wavelength of 830 nm and operates an output power of 10 mW. Transmission characteristic analysis (TRA) was conducted through the system to determine how much power reaches the retina and the detector. Transmission analysis in Code V computes the transmission of an optical system, including the effects of lens material absorption plus single or multilayer anti-reflection coatings. TRA output shows the transmission associated with each surface due to coatings, diffraction efficiency and apodization, as well as the bulk transmission associated

with material absorption losses in between surfaces. The transmission ratio due to surface losses, referred to as REF and the transmission ratio due to bulk absorption, referred to as ABS is determined. It was determined that REF=0.7446 and ABS=0.9756, for an average wavelength 830 nm. However, when the PSG and PSA are introduced in the beam path REF= 0.2862 and ABS is= 0.9756. As described by Malus's law, the transmission decreases substantially when the beam interacts with the PSG and PSA.

3.8 Discussion

The MM scanning opthalmoscope was designed by modifying the donated SLO. The main modification included the implementation of the PSG and PSA in the input illumination and pinhole detection channel, respectively. Instrumentation requirements were specified to produce a competing product for the commercial market. It is essential that the polarization modulation unit must be repeatable and accurate, with fast modulation capability [80, 108, 110, 168]. Therefore, three methods for polarization modulation were compared, and the optimal method was selected based on the need for fast, repeatable and accurate polarization modulation. Rotating QWPLs provided better polarization modulation than PEMs and MO modulators. To further improve the design, an alternative design was presented in which four QWPLs were placed sequentially on a linear holder to reduce rotational errors in MM polarimetry. A linear actuator allows the linear holder to be moved into different positions, enabling one QWPL to be in the beam path at a given time. Therefore, the suggested PSGs and PSAs were designed using a polarizer, followed by the linear holder with the four QWPLs presented in Section 3.6.4.

The modified optical setup was assessed for image quality. The donated SLO with a small entrance pupil has an optical resolution of 9.8 μm, as determined in a diffraction-limited eye. Based on research previously conducted by members of Campbell labs, the required resolution was determined to be approximately 10 μm for imaging amyloid-β deposits in the neuronal retina, and is further discussed in Section 5.1.3 [47]. While the cuttoff frequency indicates that deposits at this size could be resolved with the current setup, the modulation or contrast beyond 80 cycles per/mm to this cuttoff is low. Thus, an improved contrast at these spatial frequencies could better detect amyloid-β deposits. Theoretically, the diffraction-limited optical resolution can be improved in the SLO by using a shorter wavelength or a larger pupil [10]. These changes are accompanied by other factors, in that when the wavelength is reduced, scattering increases and allowed light exposure decreases. In addition, when a large enough pupil size is used, more aberrations are introduced. Adaptive optics (AO) could be used to improve resolution and to enable a larger incident beam

with wavefront aberration correction. However, the use of a deformable mirror will increase the instrument's price and footprint. Therefore, the optimal pupil sizes that provide the best image quality as a function of age are presented in Chapter 4. The implementation of these changes and further investigation of image quality of the modified design are presented in Chapter 5. Further, the pinhole size in the original donated optical setup was significantly larger than the diffraction limited spot size diameter of $18.9\mu m$ on the retina caused by the second pass. However, according to the image sharpness and throughput for varying TDLs previously documented in [107], the best tradeoff between sharpness and throughput is for TDLs closer to 1. Optimal pinhole sizes are also identified in Chapter 4, and modifications are implemented in Chapter 5.

Because imaging the peripheral retina is of major importance in AD diagnosis [8, 109, 125, 184], the FOV was assessed. The FOV was determined to be 65 degrees from the nodal point. Thus, this device can be characterized as a widefield polarimetric opthalmoscope, making it a very attractive diagnostic tool. The pixel size, another central characteristic, was determined to be approximately 9.5 μm. This resolution is larger than we wish to resolve amyloid beta deposits. Therefore, that pixel size must be decreased by either reducing the FOV or by increasing the number of pixels by obtaining a 4k by 4k instead of a 2k by 2k image. To be precise when the target optical resolution is 10 μm the pixel size should be 5 μm, and for a 65 degree FOV an image size of 3800 by 3800 pixels is required.

In the donated SLO, galvo scanners are used to raster scan the retina. It was determined that a single image acquisition time of 1.18 s is relatively slow considering that at least sixteen images have to be taken for the MM polarimetry analysis, and therefore 18.9 s are required for a complete image set. Further analysis of fixation eye movements indicated that microsaccades could result in a small degradation or blur in a single line scan, while tremors and drifts should not introduce any visible distortion. Therefore, it is suggested that a fixation target should be optimized to reduce the effect of microsaccades. By nature, the eye is never still, even during fixation. There is evidence that shape, color, or eccentricity may influence the amplitude and direction of fixation eye movements [162]. The fixation target in the original instrument design was blue. Recent studies focusing on determining the causes of age-related macular degeneration (AMD) onset suggest that blue light may be a factor in AMD [1, 100, 183]. Since the older population makes up the main study subjects, it is recommended that a green target should be used instead of a blue one. Another study found that a target shape of a bull's eye and cross hairs resulted in a lower microsaccade rate [162]. Therefore, a target identical to this can be used. Further, previous research papers document that fixation stability does not change with age and that older observers focused on a fixation target have fixation eye movements similar to those of younger observers [172].

In conclusion, this chapter has introduced an MM scanning opthalmoscope capable of obtaining the full MM of the retina for a 65 degree FOV from the nodal point. Image quality analysis identified a need for modification to optimize the optical setup for imaging amyloid-β deposits in the retina of older adults. Chapter 4 presents the optimal pupil and pinhole sizes for improved image quality in older adults. Chapter 5 implements these modifications and present the final optimized optical setup.

Chapter 4

Optimized Conditions for Improved Image Quality as a Function of Age

4.1 Introduction

The scanning laser opthalmoscope (SLO), first described in early 1980s [177], uses a monochromatic laser source that is raster scanned to obtain an image of the retina. For *in-vivo* retinal imaging, the ocular optics are employed as a microscope objective. Therefore, the image quality, in such imaging systems, is limited by the complex nature of the human eye. Aberrations due to refraction of ocular surfaces, diffraction through the entrance pupil and intraocular scattering are the main sources of reduced image quality [10]. It was previously reported that the average optical performance of the human eye progressively declines with age [81, 82]. The increase of monochromatic ocular wavefront aberrations as a function of age was documented by several research groups, which explains the decline of optical performance and retinal image quality [40, 73, 121, 150]. Previous work on the relationship between monochromatic aberrations and age have shown high intersubject variability. [4, 40, 71, 73, 81, 82, 121, 150, 173].

In addition, blur, due to diffraction, decreases with increasing pupil size, while blur due to aberrations increases [9, 62, 146]. In the same way, optical quality metrics when limited only by diffraction tend to improve with increasing entrance pupil size. However, in the presence of wavefront aberrations, image quality becomes worse with increasing pupil size [9, 43, 62]. The effect of both diffraction and wavefront aberrations on optical image quality as a function of pupil size indicates that there is a point, which balances these effects to provide an optimal pupil size for best image quality [43, 62]. Campbell and

Gubisch determined that an optimal pupil size of 2.4 mm provides best lateral resolution based on 3 subjects in an experimental setup [43]. Donnely and Roorda determined that an optimal pupil size of 2.46 mm $\pm$ 0.66 mm improves lateral resolution, and a 4.30 mm $\pm$ 1.19 mm pupil improves axial resolution, based on aberration from 16 young adults and using a phase plate eye to model the aberrations of the eye [62].

In this study, I first determined the relationship between monochromatic higher order (HO) wavefront aberrations and age. While this is not a new finding, it is important to evaluate this relationship. The main objective of this study, which uses data from 1219 eyes of 20-70 years old, is to quantify retinal image quality to identify optimal pupil sizes as a function of age, that can be used in the design of SLO and cSLO systems. Age group specific, optimal pupil sizes for four image quality metrics are determined in this study. The age dependence of optimal pupil size is useful for the design of diagnostic instruments. In particular, for instruments specialized in the diagnosis of Alzheimer's disease, like the one presented in Chapter 3, it would be optimal to use entrance pupils that would maximize image quality for older adults since Alzheimer disease is prevalent in the older population [140]. To study image quality as a function of age, I implemented Zernike polynomial phase plate eye models, where each modeled subject-specific monochromatic aberrations and took into account diffraction at the entrance pupil. Data of Zernike polynomial coefficients were provided by Salmon [150] for 1219 subjects, who were between 20 and 70 years old.

The second objective of this study is to produce measures of both HO wavefront error and retinal image quality as a function of pupil size. These curves are also stratified by subject age. To my knowledge, this was the first time these results were documented based on a large data set ($n = 1219$), providing age dependence. Such plots could assist with optimized instrumentation design in order to maximize image quality on the retina and subsequently improve retinal images, in instruments designed for a specific population.

The relationship between optimal pupil size, RMS wavefront error and age was identified. At the end of this study, the optimal pinhole size for an SLO is also presented for optimal lateral and axial resolution. The work presented in this chapter can be used as a benchmark for future instrumentation design, but its predictions should be tested experimentally.

4.1.1 Optics of the human eye

The human eye is a sophisticated optical instrument with imperfect optical quality. Light incident on the cornea and crystalline lens, is then incident onto the retina. Light is then absorbed by the photoreceptors and the signal is transmitted to the visual cortex for

further processing. At pupil sizes used for daytime vision, optical quality approximately matches the cone photoreceptor sampling. At larger pupils, ocular aberrations are higher. Not only do eye's aberrations vary significantly with pupil size, they also vary from one person to another, making the design of optical instruments to be used with the eye a challenge, since the eye's optical quality impacts the quality of fundus imaging systems.

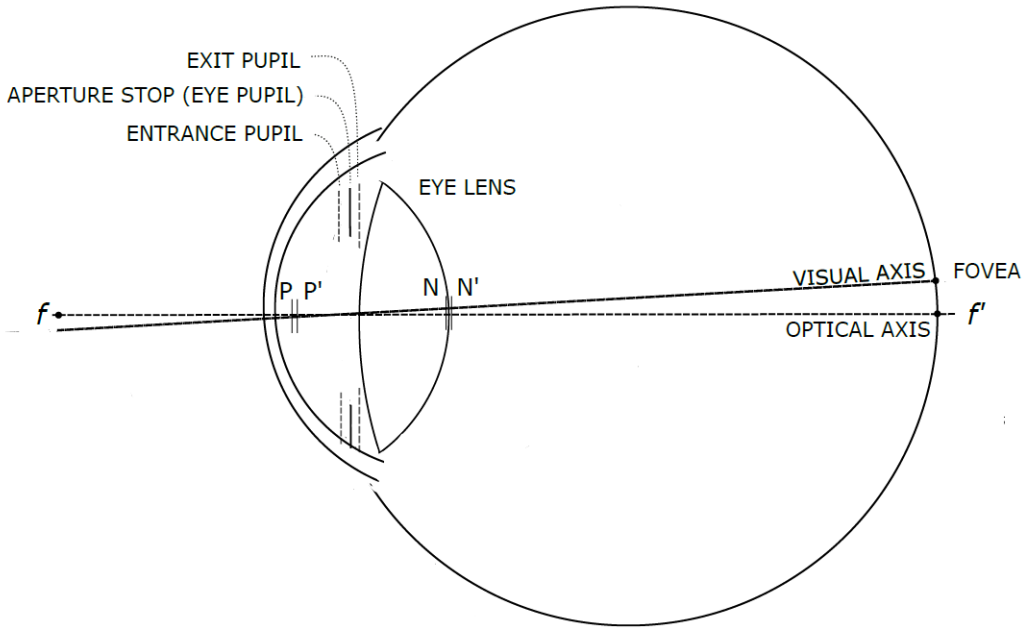

Figure 4.1: Gullstrand–Emsley relaxed schematic eye by Bennet and Rabbetts [146]. Drawn in Inkscape.

The Gullstrand–Emsley relaxed schematic eye presented in Figure 4.1 uses the assumption that all the refractive surfaces are co-axial with the cornea and crystalline lens, having a common optical axis. The cardinal points in the relaxed schematic eye are illustrated in Figure 4.1. Cardinal points enable calculation of image position and size without any information on the ocular biometry [18]. Due to the refractive index of the aqueous and vitreous, nodal points are shifted deeper into the eye, and are not coincident with the principal planes [9, 18]. The first and second principle point, P and P', lie in the anterior chamber while the nodal points N and N', are positioned near the back surface of the crystalline lens. The equivalent power of the eye, F_o, has been defined as $F_o = 60D$ with

a refractive index, $n = 1.336$, for an average eye used here [146]. The posterior nodal distance to the second focal length (N'F') is derived in Equation 4.3 which is used for determining the resolution limits for the diffraction-limited eye in Section 4.1.2 [146].

$$f_o = PF = \frac{1000 \times n_{air}}{F_o} = 16.67mm \tag{4.1}$$

$$f'_o = P'F' = \frac{1000 \times n_{eye}}{F_o} = 22.27mm \tag{4.2}$$

$$f_o = PF = N'F' \approx \frac{f'_o}{n_{eye}} \approx 16.67mm \tag{4.3}$$

Entrance and exit pupils

The entrance and exit pupils are illustrated in Figure 4.1. The entrance pupil is the image of the real pupil formed by the cornea. The exit pupil is the image of the real pupil formed by the crystalline lens. The entrance, exit and real pupil are all conjugate to each other but have different magnifications [62, 146]. As documented by Bennet and Rabbetts, the entrance pupil is 13% larger than the real pupil and the exit pupil is 3% larger than the real pupil [146]. The entrance pupil then is 10.0% larger than the exit pupil [62].

4.1.2 Theoretical resolution for the diffraction-limited eye

The Rayleigh criterion is equivalent to lateral resolution in a diffraction-limited system [28, 146]. For a circular aperture, the Rayleigh criterion states that two images are resolvable when the center of the diffraction pattern of the one is incident on the first minimum of the diffraction pattern of the other. The smallest possible resolvable angle is defined by Equation 4.4 where λ is the wavelength, and D is the entrance pupil diameter [28, 146].

$$\theta = \frac{1.22\lambda}{D} \tag{4.4}$$

By multiplying equation 4.4 with the length from the posterior nodal point to the second focal length (f_o) we can convert the lateral resolution from angular units to microns. NA is the numerical aperture of the eye [28, 146].

$$r_{\text{lateral}} = \frac{1.22\lambda}{D} f_o = \frac{0.61\lambda}{NA} \tag{4.5}$$

Unlike lateral resolution, there are two algebraic expressions that describe resolution in the z-direction as defined in [28, 138, 182]. The axial resolution, in depth (the z-direction) as described by Wilson in [138], is first defined using "normalized optical coordinates, u, rather than real-space coordinates", and then converted to μms. As described by Born and Wolf in [28], the relationship between axial real-space units (z) and axial optical units (u) is described by Equation 4.6 where n is the the index of refraction of the medium surrounding the specimen and λ is the wavelength.

$$u = \frac{2\pi NA^2}{n\lambda}z \tag{4.6}$$

The numerical aperture of the human eye, NA, expressed in Equation 4.7, where n is the index of refraction of air (n=1) and r is the entrance pupil radius ($r = \frac{D}{2}$) [138].

$$NA = nsin\alpha \approx \frac{r}{f_o} \approx \frac{D}{2f_o} \tag{4.7}$$

A second equation for axial resolution is described by Wilson [138, 182], which relates axial real-space units (z) and axial optical units (u) as described by Equation 4.8, where λ is the wavelength, n is the index of refraction of the medium around the specimen ,in the case of the retina $n \approx 1.337$, and $sin(\frac{\alpha}{2})$ is related to the NA.

$$u = \frac{8\pi n}{\lambda}(sin(\frac{\alpha}{2}))^2 z \tag{4.8}$$

Using the small angle approximation limit, $sin(\frac{\alpha}{2}) \approx \frac{r}{2f_o}$, Equation 4.6 simplifies to Equation 4.9 [138].

$$u \approx \frac{8\pi n}{\lambda}(\frac{r}{2f_o})^2 z = \frac{2\pi NA^2}{\lambda n}z \tag{4.9}$$

The axial resolution equation is then defined by Equation 4.10. This equation is derived in the paraxial approximation limit and insight on the high angle equivalent is presented in [156]. The variable u is an experimental measurement corresponding to the distance between the half intensity points of the focused spot. This is equivalent to the full width at half maximum (FWHM) of the integrated intensity of the point spread function (PSF) and defocus plot for a confocal scanning system given in optical units. [63, 138].

$$z = u\frac{n\lambda}{2\pi NA^2} \tag{4.10}$$

Values for u were determined experimentally and are dependent on the type of object imaged. For a diffraction-limited optical system, the halfwidth at half maximum of the

integrated intensity distribution along the u axis was found to be $u_{1/2} = \pm 4.4$ [63]. This corresponds to a FWHM of 8.8, $u = 8.8$ o.u. The axial resolution for the diffraction-limited eye is then defined by Equation 4.11, consistent with [63]

$$z = \frac{4.4n\lambda}{\pi NA^2} \tag{4.11}$$

4.1.3 Monochromatic aberrations in the eye

The eye is an optical system subject to a number of aberrations affecting resolution. Monochromatic aberrations are present in the eye, at larger pupil sizes [95, 135]. As with any optical system, the presence of aberrations in the eye reduces retinal image quality. Monochromatic aberrations can be described in terms of ray aberrations by longitudinal and transverse aberration and in terms of wavefront aberration $W(x, y)$. In this study, monochromatic aberrations are described in terms of wavefront aberrations as they are used to define aberrations over the entire pupil [158].

Wavefront aberrations

A wavefront is described as " a surface that has a constant phase, and is perpendicular to the rays". In an aberration-free optical system the shape of the wavefront is either spherical for nearer points or planar for distant sources [26]. After transmission through a perfect converging lens, the wavefront is spherical so that, in the geometrical approximation, all rays focus to a point [187]. When there are aberrations in the wavefront, the wavefront surface is no longer a sphere but has some other shape. The wavefront aberration at the eye pupil can be calculated as the optical path length difference between the actual wavefront and the ideal spherical wavefront [104, 136, 158].

Wavefront aberrations described by Zernike polynomials

In vision science, wavefront aberrations are described by the ophthalmic optics OSA convention using a Zernike polynomial function series [16, 163]. The wave aberration $W(\rho, \theta)$ has a polar representation defined by Equation 4.12 where $Z_n^m(\rho, \theta)$ is the Zernike polynomial and c_n^m is its weighting coefficient and represents the amount of that aberration [16, 158, 187]. The wave aberration is a function of ρ which is the normalized distance

from the center of the pupil ranging from 0 to 1 and θ is a meridian in the pupil in radians that ranges from 0 to 2π.

$$W(\rho,\theta) = \sum_{n=0}^{k} \sum_{m=2i-n}^{n} c_n^m Z_n^m(\rho,\theta) \tag{4.12}$$

Zernike polynomials are a set of generalized polynomials on the unit circle that are orthogonal to each other. The benefit of using Zernike polynomials is that the polynomials are independent from each other, and the sum of the coefficients gives the wavefront error. In addition, each Zernike polynomial describes a certain type of shape. The total aberration map is the weighted sum of fundamental shapes [26, 95, 135].

Each Zernike polynomial is the product of three terms, a normalization term, radial term and a meridional term as shown in Equations 4.13 and 4.14.

$$Z_n^m(\rho,\theta) = N_n^m R_n^{|m|}(\rho) cos(m\theta) \text{ for } m \geq 0, 0 \leq \rho \leq 1, 0 \leq \theta \leq 2\pi \tag{4.13}$$

$$Z_n^{-m}(\rho,\theta) = N_n^m R_n^{|m|}(\rho) sin(m\theta) \text{ for } m < 0, 0 \leq \rho \leq 1, 0 \leq \theta \leq 2\pi \tag{4.14}$$

Part of the definition of Zernike polynomials is that for a given n, m can only take values of $-n, -n+2, -n+4$. The normalization factor N_n^m is given by equation 4.15.

$$N_n^m = \sqrt{\frac{2(n+1)}{1+\delta_{m0}}}, \delta_{m0} = 1 \text{ for } m = 0, \delta_{m0} = 0 \text{ for } m \neq 0 \tag{4.15}$$

The radial term $R_n^{|m|}(\rho)$ is described by Equation 4.16

$$R_n^{|m|}(\rho) = \sum_{s=0}^{(n-|m|)/2} \frac{(-1)^s (n-s)!}{s![0.5(n+|m|)-s]![0.5(n-|m|)-s]!} \rho^{n-2s} \tag{4.16}$$

4.1.4 Human eye models in literature

Optical models of the human eye have been widely used for studying how refraction and aberrations are affected by anatomical changes [18]. In addition, they provide a framework on how retinal images are formed. Eye models have been used extensively in vision science providing insights on the visual process and the limitations imposed on vision by ocular optics [18].

Since the 19th century, optical eye models of varying complexity and anatomical accuracy have been developed. Emesley's reduced eye model, is among the first and most

well-known schematic eyes [146]. The reduced eye models are anatomically inaccurate, as they have a single high-powered surface [18, 146]. Three refractive surface eye-models were introduced like the Gullstrand-Emsley eye model which modeled the crystalline lens by using two refractive surfaces, as illustrated in Figure 4.1 [146]. The Le Grand's full theoretical eye model further improved the anatomical accuracy of the Gullstrand-Emsley model by using two corneal and two lens refracting surfaces. These last two designs enabled accommodation in the models [18, 146]. After the discovery of the inhomogenious nature of the crystalline's lens refractive index, more sophisticated and accurate human eye models were developed. Gradient index optics were first implemented by using nested, homogeneous shells with different refractive indices like the Gullstrand's No. 1 'exact' eye [18, 146]. Gullstrand's No. 1 'exact' eye has two corneal and four lens refractive surfaces. More models have followed with a greater number of shells. With advanced technology and increased understanding of the internal optical structure of the human lens, gradient index (GRIN) lens models were developed. GRIN design models the eye lens as a series of isoindical contours [27, 111, 129]. Navarro, Liou and Brennan schematic eyes are among many accurate eye models that were designed [111, 129]. A further advancement in eye models that happened parallel to the GRIN lens work was moving from paraxial models, which only accurately predict on-axis image quality at small pupils, to finite eye models. Finite eye models introduce aspherical surfaces like conics to more accurately model the image quality for large pupil sizes on and off-axis, which provides a more accurate prediction of image quality [18, 113, 126, 158].

While these eye models are anatomically correct and provide accurate results, the biometric data used are often based on population means or chosen to predict the image quality without the use of a lens GRIN so are not biometrically correct. An average eye model of a population causes some aberrations to approach zero, particularly asymmetric aberrations, reducing the total wavefront error. For the purpose of this study it is required to create an individual eye model for each subject. Navarro et al. developed customized eye models using biometric data specific to individuals [130]. However, this study does not have access to such data. Therefore, eye models using Zernike polynomial phase plates using subject-specific wavefront aberrations were implemented as described in section 4.2.1. Phase plate eye models were previously used to model younger eyes in [83] and [102] but this is the first time they were used to study image quality as a function of age.

4.2 Methods

Zernike polynomial phase plate eye models, described in section 4.2.1, were implemented in Code V (Optical Design software). Image quality analysis was carried out in Code V. Using the application programming interface (API) of Code V, I wrote a program to establish communication between Matlab and Code V to enable automation of this analysis, which is explained in Section 4.2.4. Hannah Sara Rosenberg has contributed to this work by writing code to generate Zernike polynomial coefficients specific to each subject and pupil size.

4.2.1 Zernike polynomial phase plate eye model

A paraxial eye model was implemented in Code V. Monochromatic aberrations were modeled by adding a Zernike polynomial phase surface in the entrance pupil in air for each subject [62]. Zernike polynomial coefficients were provided by Salmon [150] for 1219 subjects, who were between 20 and 70 years old. Zernike polynomial coefficients for each subject and each pupil size were corrected for best refractive correction. Only HO Zernike polynomial coefficients were included in this analysis; first and second order terms were excluded. A schematic of the Zernike Polynomial phase plate is illustrated in Figure 4.2 for a single subject. Incoming light is incident on the entrance pupil where the Zernike polynomial phase plate and pupil size are specified. The distorted wavefront travels through the posterior focal length, f=22.27 mm, and index of refraction n=1.336. The PSF of the distorted wavefront on the retina is illustrated in Figure 4.2.

Zernike coefficients provided by Dr. Salmon

Zernike coefficients obtained from Shack-Hartmann measurements of human eyes, originally from five different laboratories from large population studies, were provided by Salmon [150]. As described in [150], Zernike coefficients that were received from each laboratory were "rescaled for pupil diameters of 5.0 mm and corrected to 550 nm using a chromatic correction procedure" described in [118, 151] and further explained in Chapter 5. The measurements of the Zernike coefficients were centered on the center of the entrance pupil for all five studies. Three of the groups obtained Zernike coefficients without pupil dilation while the rest used a dilation agent. Since dilation agents are known to cause pupil decentration, they would be expected to change the Zernike coefficients. Upon further analysis, I confirmed that there was no statistical significant differences between the

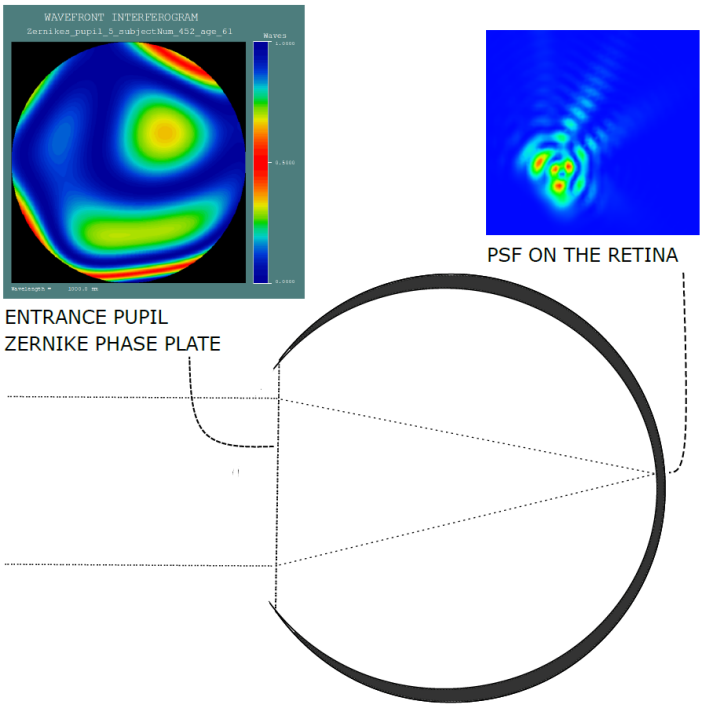

Figure 4.2: Zernike Polynomial phase plate eye model with the PSF resulting on the retina (on the right) from the given phase plate (on the left). The phase plate is an interferogram of the distorted wavefront in the pupil plane. The PSF on the retina was obtained in Code V. Drawn in Inkscape.

HO RMS found in each of the five studies [4, 53, 143, 164, 173]. Each laboratory received ethics approval from their respective Universities. Participants provided informed consent for the original study and for future work.

4.2.2 Image quality metrics

Optical and image quality (optical performance) metrics on the retina were used as an objective method to determine the optimal entrance pupil sizes [10]. Optimal entrance pupil was defined as the pupil size that gave a given metric of best image quality, previously described by Donnelly and Roorda [62]. Optical quality was measured by the root-mean-square (RMS) wavefront error [10] in the pupil plane. In addition, three optical quality metrics in the image plane, based on the PSF, were assessed including the diameter of

50% encircled energy (EE), the strehl ratio (SR), and FWHM of the squared integrated intensity as a function of depth. Three optical quality metrics in the Fourier domain were used including entropy, area under the Hopkins ratio, and the cutoff frequency [10]. In this analysis, each metric was obtained, for pupil sizes ranging from 1 to 5mm in increments of 0.25 mm for all 1219 subjects. The results were stratified by four age groups; 20-32, 33-45, 46-57 and 57-70. Optimal pupil sizes for each metric and age group were determined by averaging the optimal pupil sizes of subjects in an age group. All metric values were tested for distribution normality using the Kolmogorov-Smirnov test ($p < 0.05$). A two sample Kolmogorov-Smirnov test was also used to identify if two curves are statistical significant from each other. A regression analysis was performed testing the relationship between image quality metrics, optimal pupil sizes and age. The statistical significance of these results were assessed using a t-test or a Mann-Whitney test, in addition to the p-value obtained in regression. The t-test was used in the case of a normal distribution and a Mann-Whitney test was used in the case of a non-normal distribution.

Wavefront aberrations

Wavefront aberrations (WA) of the eye are most commonly described by Zernike polynomial expansions. As described in section 3.1.3, Zernike polynomials are widely used in ophthalmology due to their convenient nature. They are set a of generalized polynomials on the unit disk that satisfy the orthogonality relation. Equation 4.17 describes the WA as a linear combination of normalized Zernike polynomials.

$$WA(r,\theta) = \sum_{n,\pm m} c_n^{\pm m} \cdot Z_n^{\pm m}(r,\theta) \tag{4.17}$$

In equation 4.17, r is the pupil size, θ is the angular variable over the pupil, $Z_n^{\pm m}(r,\theta)$ is the Zernike polynomial and $c_n^{\pm m}$ is the aberration coefficients. The subscript n indicates the order of aberration. The superscript m is the angular frequency denoting the number of times the wavefront pattern repeats itself [10, 187].

Variance, σ^2, is used to described the spread of a set of numbers around the mean and from each other. The variance of the WA can be determined by subtracting the square of the mean of the WA from the mean of the squares of the WA presented in Equation 4.18.

$$\sigma_{WA}^2 = \overline{WA^2} - \overline{(WA)}^2 \tag{4.18}$$

The root-mean-square (RMS) wavefront error of HO abberations, one of the most-used optical quality metrics, is then calculated as the square root of the variance σ^2, described

in Equation 4.19.

$$RMS = \sigma_{WA} = \sqrt{\overline{WA^2} - \overline{(WA)}^2} \tag{4.19}$$

Since $\overline{(WA)}$ is fixed to zero the RMS is reduced to 4.20, where it is equal to the standard deviation. Equation 4.20 describes the spread of WA from the average [10].

$$RMS = \sqrt{\overline{WA^2}} \tag{4.20}$$

The advantage of using Zernike polynomials to describe the WA is that the RMS of WA can then be obtained easily from the Zernike coefficients. This is because of the orthogonality of Zernike polynomials. The variance then of the WA is given by the sum of the variance of each of the orthogonal components of the polynomial expansion,$(c_n^{\pm m})^2$, in equation 4.21 [10].

$$RMS^2 = \sum_{n,\pm m} (c_n^{\pm m})^2 \tag{4.21}$$

In this study, only the effect of HO aberrations were studied, since first and second order can be addressed with best refractive correction for each individual.

Srehl ratio

The SR describes the quality of the PSF as a scalar value and is commonly used as a measure of optical performance. SR is defined as the ratio of peak PSF intensity of the aberrated system and peak PSF intensity of the equivalent diffraction-limited system. The SR is pupil size specific and is described by Equation 4.22 [10].

$$SR = \frac{max(PSF)}{max(PSF_{DL})} \tag{4.22}$$

where PSF_{DL} is the diffraction-limited PSF and PSF is the aberrated PSF of the system. A perfect, diffraction-limited system results in a SR of 1, whereas a completely aberrated system results in a SR that approaches 0 [10]. In this study the SR was identified but not used for determining the optimal pupil size. This is because there is a monotonic relationship between entrance pupil and SR. Therefore, as the pupil increases, SR decreases, due the presence of aberrations, without any inflection point, which would signify the presence of an optimal pupil.

Lateral resolution

Lateral resolution describes quantitatively how small a feature can be resolved in the image of the retina. It is often calculated as the FWHM of the 2D PSF. The FWHM is measured by the distance between points on the PSF curve at which the intensity reaches half its maximum value [10, 157]. Since the PSF of the subject specific eye model is not symmetric, due to the presence of HO aberrations, including coma, another metric that will account for the asymmetric nature is used [157]. The diameter of the 50% EE was used as a metric of image quality and specifically resolution, similar to the methods described by Donnelly and Roorda [62]. EE measures the fraction of the total energy in the PSF that lies within a circle of a specified radius. It is calculated by first determining the total energy of the PSF, and identifying the centroid. Circles of increasing radius are then drawn from the centroid. The percentage of EE is determined by measuring the energy within each circle and dividing it by the total energy. As the radius of the circle increases, more of the PSF energy is enclosed. Therefore, EE ranges from zero to one [10]. The diameter of 50% EE is defined as the diameter of circular area that captures 50% of the light energy. Mathematically the diameter of 50% EE is computed from Equation 4.23 where r is the radius and ϕ is the angular variable within the circle of interest.

$$\int_0^{D50} \int_0^{2\pi} PSF_N(r,\phi) r dr d\phi = 0.5 \tag{4.23}$$

In a diffraction-limited system the energy of the PSF in concentrated within the center of the PSF. The energy is less concentrated within the center of the PSF in the presence of ocular aberrations. If the energy is concentrated within a small radius from the PSF center, the optics are good and lateral resolution is high. If the energy is distributed over a large area and a large radius is required to contain most of this energy, then this indicates poorer optics and lower lateral resolution. In a diffraction limited eye the EE is 7% different than the resolution determined by the cuttoff frequency. In addition, EE is often also described as light in the bucket. The EE was determined from the PSF on the retina of the Zernike polynomial phase plate eye model, described in section 4.2.1, using a built-in function in Code V. The pupil size with the smallest diameter of 50% EE corresponded to the optimal pupil.

Entropy

Entropy is a measure of spatial variance of the PSF and describes how the energy is distributed in the two dimensional image [10, 91]. It can be mathematically calculated using

Equation 4.24, which is commonly known as Shannon entropy. An aberration-free PSF shows minimum entropy with maximum concentration of light in the center. Aberrations increase the entropy because light tends to spread throughout the image.

$$H = -\sum_{x,y} PSF_N(x,y) log(PSF_N(x,y)) \tag{4.24}$$

Entropy can be defined in the spatial domain using the PSF or the frequency domain using the optical transfer function (OTF). In this work entropy is defined as a function of OTF in equation 4.25 and 4.26.

$$OTF = \left|\mathcal{F}(PSF(x,y))\right| \tag{4.25}$$

$$H = -\sum_{x,y} OTF_N(x,y) log(OTF_N(x,y)) = -\sum_{x,y} I_{OTF}(x,y) log_{OTF}(I(x,y)) \tag{4.26}$$

Modulation transfer function

Assessing contrast as a function of spatial frequency is another commonly used test of performance. A Foucault grading, a target consisting of sinusoidal gratings, is used to represent line objects. The smallest spating that can be imaged by the optical system is regarded as the limit of resolution, which is expressed as lines per millimeters or lines per degree. Modulation is described by Equation 4.27, where I_{max} and I_{min} are the maximum and minimum intensity levels in the image. The modulation transfer function (MTF) is a plot of the modulation as a function of spatial frequency. The modulation reaches zero at the cutoff frequency (f_{cutoff}) for a diffraction-limited eye. Therefore, f_{cutoff} of the MTF can be used as limit of resolution based on the minimum separation, or angle, at which two points can be distinguished as individuals [28].

$$M = \frac{I_{max} - I_{min}}{I_{max} + I_{min}} \tag{4.27}$$

When accessing the image quality from the MTF one can either identify the f_{cutoff} or identify the modulation for specific spatial frequencies of interest. Due to the fact that only HO aberrations were used in the eye models, excluding defocus, the MTFs were less prone to approach modulations as low as zero. A more important limitation is contrast reversal when working with MTFs instead of OTFs. Contrast reversal is directly related to the sign reversal in the real part of the OTF. This means that in the MTF, which is obtained by the magnitude of the OTF, neglecting the phase information, does not reach zero but simply reaches a minimum point modulation. To overcome this issue and identify

the cutoff spatial frequency, the spatial phase information was used to estimate the actual f_{cutoff} frequency in cases where the modulation did not reach zero. Lateral resolution from the f_{cutoff} can be plotted using Equation 4.28. This was used as secondary measure of lateral resolution to EE. Optimal pupil size in each subject was determined as the one that gave best lateral resolution or cutoff frequency.

$$\mathrm{r}_{\mathrm{lateral}} = \frac{1.22}{f_{cutoff}} \tag{4.28}$$

Area under the Hopkins ratio

While the MTF captures a lot of information about an optical system, it is desirable to describe performance with a single scalar metric instead of a function, and this is enabled by determining the area under the Hopkins ratio (HR) as an image quality metric for the human eye [10]. The HR is defined as the actual aberrated MTF divided by the diffraction-limited MTF as a function of spatial frequency, as described in Equation 4.29.

$$HR(f) = \frac{MTF(f)}{MTF_{dl}(f)} \tag{4.29}$$

The area under the HR is a more global measurement of image quality as it accounts for all spatial frequencies. The area under the HR is defined by Equation 4.30, where the HR is integrated between zero and the diffraction-limited f_{cutoff} [10, 87].

$$AHR = \int_0^{f_c} HR(f)df = \int_0^{f_c} \frac{MTF(f)}{MTF_{dl}(f)}df \tag{4.30}$$

The area under the HR is a useful metric for the purpose of this work as it is dependent on pupil size and was used in this study, in addition to the other metrics presented in this section. Optimal pupil size for each subject was determined as the one that results in the largest area under the HR.

Axial resolution

By employing a cSLO setup, some optical sectioning in depth can be accomplished particularly if adaptive optics is used, unlike fundus photography [62, 177, 182]. Axial resolution is equivalent to depth of focus and is defined as the distance in depth that the imaged surface can be moved without significant deterioration of image quality [146]. The smaller the depth of focus, the better the axial resolution.

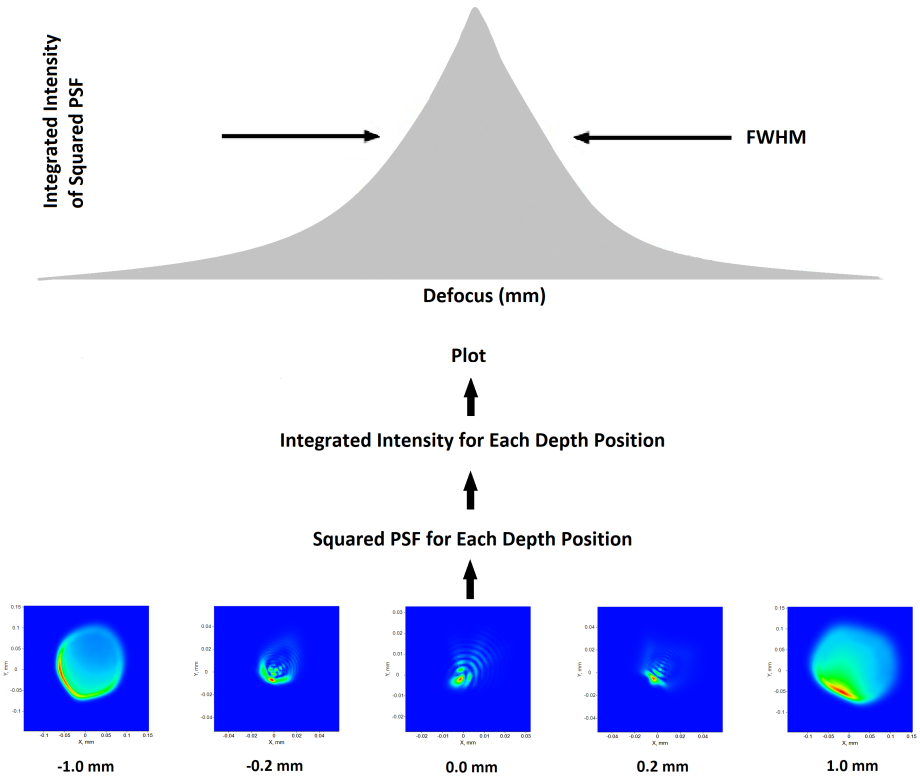

Figure 4.3: Axial resolution calculation summarized in four steps. Five through-focus PSFs are illustrated in the bottom of the Figure. The PSFs illustrated were obtained for a single subject at 4mm entrance pupil size. Defocus values are indicated below of the PSFs. Axial resolution is determined by the FWHM of integrated intensity as a function of defocus. Adapted with permission from [62] © The Optical Society.

The quantitative measurement, or metric, for axial resolution was derived from the theory of light detection in the confocal scanning laser ophthalmoscope. This theory states that "the measured PSF of a cSLO is proportional to the square of the intensity of the 3D point spread function" as described in [62, 182]. In fundus photography the integrated intensity for each axial position is identical in all planes [62]. In a cSLO, when reflected light is focused onto the pinhole a larger signal is detected than in the case that the reflected object image is positioned out of the focal plane. Thus, the intensity of this defocused spot is reduced. As explained by Donnelly and Roorda, "squaring is a direct optical property of the confocal pinhole" [62], and by squaring the PSF, non-linearity is introduced, which enhances high intensity peaks and attenuates the low intensities. Axial

resolution information was obtained by slicing in planes the retina through depth where each slice will contain 2D image information. Using Code V, 41 PSFs were obtained in depth, ranging from -1 mm to 1 mm of defocus, at increments of 0.05 mm. As the slice plane is further away from the the ideal focal plane the central intensity of the PSF decreases. The 41 slices were interpolated to 4000 slices. Each PSF was then squared and the integrated intensity of each squared PSF was plotted as a function of defocus. The FWHM of the resulting graph is computed which is equivalent to axial resolution. This method was described previously in [62]. The pupil that gave the smallest FWHM of the integrated intensity plot corresponded to the optimal pupil size for best depth resolution [62].

4.2.3 Effect of pinhole size on image quality

The SLO and cSLO minimize the effect of out-of-focus light and wide-angle scatter by using both a scanning beam, and a confocal pinhole or by limiting the detector area [91]. The confocal pinhole is usually placed in an optically conjugated plane with the retina. A small confocal pinhole can be described as cropping the PSF on the retina or by reducing the intensity in the wings of the PSF [149]. When using a very small pinhole, although there is high out-of-focus and scattered light rejection, it also reduces the light reaching the detector, thereby impacting throughput. A larger imaging pinhole has the ability to still remove wide-angle scatter as it manifests as a wide-angle component in the final PSF [149]. Thus, it improves contrast while maintaining sufficient reflected light hitting the detector. In this study, I simulated the effect of a confocal pinhole, that is optically conjugate to the retina, by projecting an aperture on the retina. The pinhole is described in terms of the times-diffraction-limited spot size (TDL) as presented in [107].

$$TDL = \frac{\text{Pinhole size on the retina}}{\text{Airy disc diameter}} \tag{4.31}$$

TDL is defined as the pinhole size in the retina normalized with respect to the diffraction-limited Airy disc diameter formed on the retina from the pupil 4.31 [107]. For each subject and each pupil size, 7 pinhole sizes were used. The lateral and axial resolutions were determined for all 7 pinhole sizes for each pupil size. TDLs of 0.5 to 3.0 in increments of 0.5 were studied, in addition to the results with no pinhole. Plots of throughput as a function of pinhole size were produced for each pupil to identify optimal pinhole size as a trade-off between throughput and resolution. Throughput was calculated by taking the sum of the intensity values of the PSF on the retina shown in Equation 4.32 as described

in [107].

$$\text{Throughput} = \sum_{i=1}^{n}\sum_{j=1}^{m} PSF(i,j) \tag{4.32}$$

4.2.4 Automation Process

An automation program was required in order to analyze the large data set with the methods described in the previous section. Therefore, I wrote an automation program enabling the communication between Matlab and Code V. Hannah Sara Rosenberg wrote a program to generate all the .INT files that contained the Zernike polynomial coefficients specific to each subject and pupil size. The Matlab and Code V communication was enabled by the Code V API which is an application programming interface that allows access to Code V commands from other programs [161]. The API operated using the Microsoft Windows standard component object model (COM) interface [161]. The COM interface enables the execution of Code V commands using programs such as Matlab. The Code V API was particularly useful for automation tasks providing the ability to use Code V's ray-tracing capability and data analysis with Matlab, illustrated in Figure 4.4. The

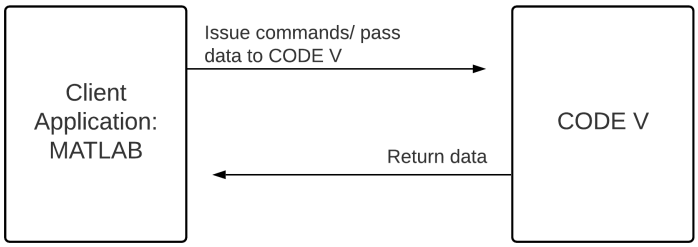

Figure 4.4: Illustration of Code V's API: Communication between client and server application

automation program provides advantages of faster acquisition of results and consistent analysis. Before running the automation code, the .INT files, which were later attached to the phase surface of each eye model, were generated by Hannah Sara Rosenberg. The .INT files contained the Zernike polynomial coefficients specific to subject and pupil size. The automation program attached the .INT files to each eye model and determined image quality metric values for each pupil size of each subject, and determined the optimal pupil sizes for each individual. The data was organized by age group, 20-32, 33-45, 46-57, 58-70 to study the age dependent of the optimal pupil size. The main steps of each program

are outlined in the flowcharts and the mathematics of each step are explained in previous sections of this chapter.

Zernike polynomial .int files

All Zernike coefficients correspond to a pupil size of 5.0 mm and a common wavelength of 550 nm. Only higher order aberration were included in this study. Therefore, piston, defocus (sphere, and astigmatism) were zeroed to mimic best refractive correction. Zernike coefficients are specific to pupil size and so a resizing method described by Campbell [42] based on [153] was used to generate coefficients for smaller pupil sizes from 1 mm to 5 mm with increments of 0.25 mm. For each subject and pupil size, the order and normalization was modified as appropriate to fit the standard of Code V. Figure 4.5 illustrates all the steps operated in Matlab to obtain individual .int files per pupil size and per subject that are normalized and rearranged as required by Code V. Using the paraxial eye model presented in section 4.2.2, individualized eye models are generated by attaching the .int file to the entrance pupil in air.

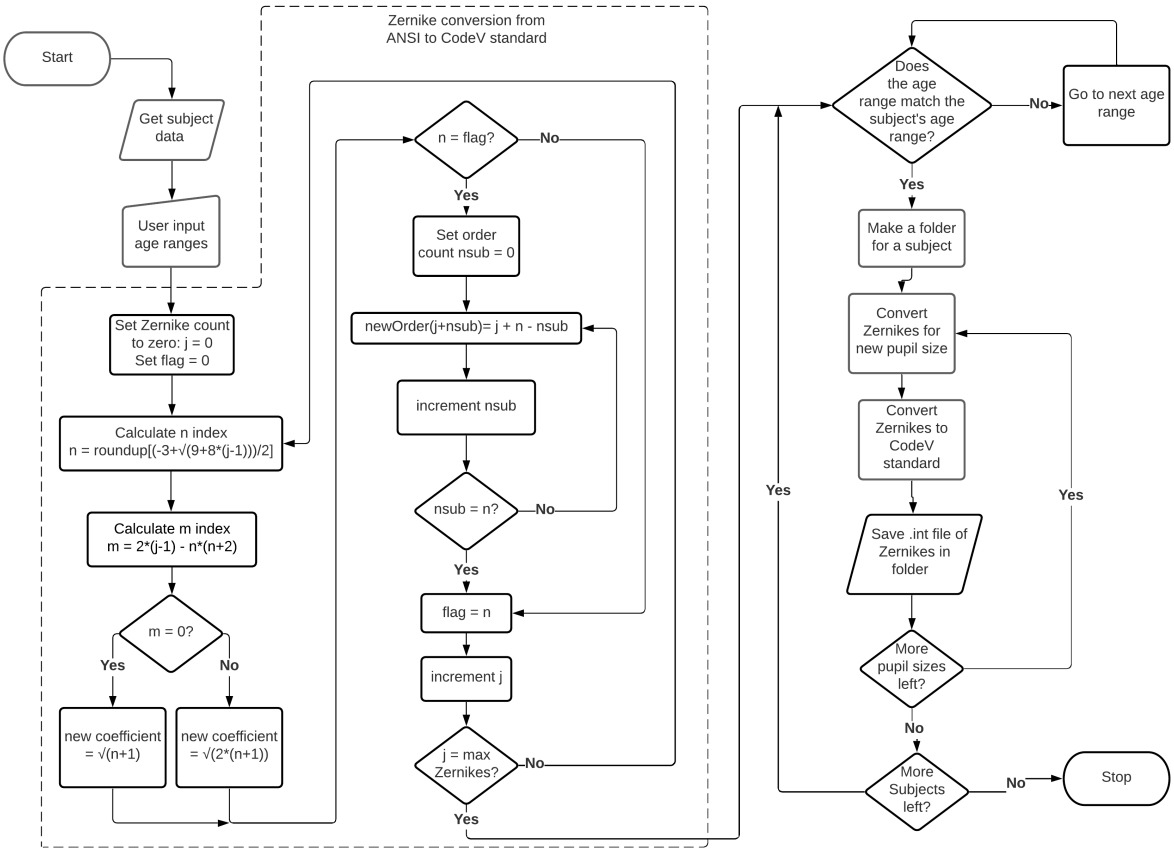

Figure 4.5: Flowchart describing the generation of .Int files containing the subject specific Zernike coefficients to be attached to the pupil of individual Zernike-polynomial phase plate eye models. Drawn by Hannah Rosenberg; see Statement of Contributions.

Optimal pupil size calculation for different metrics

The flow chart illustrated in figure 4.6 highlights the steps taken to output image quality metric values for each pupil size of all subjects, in four age groups separately. The first step in this process was to identify the subject age and subject identification number. Starting from the 5 mm pupil size, the appropriate .INT file was attached to the entrance pupil in air comprising the model eye in Code V. Image quality metrics were determined and were output into an excel file, saved to a subject specific folder. The optimal pupil size for each metric was output to a separate excel file that contained optimal pupil sizes of all subjects

in that age group. This methods allowed for easier analysis and presentation of results.

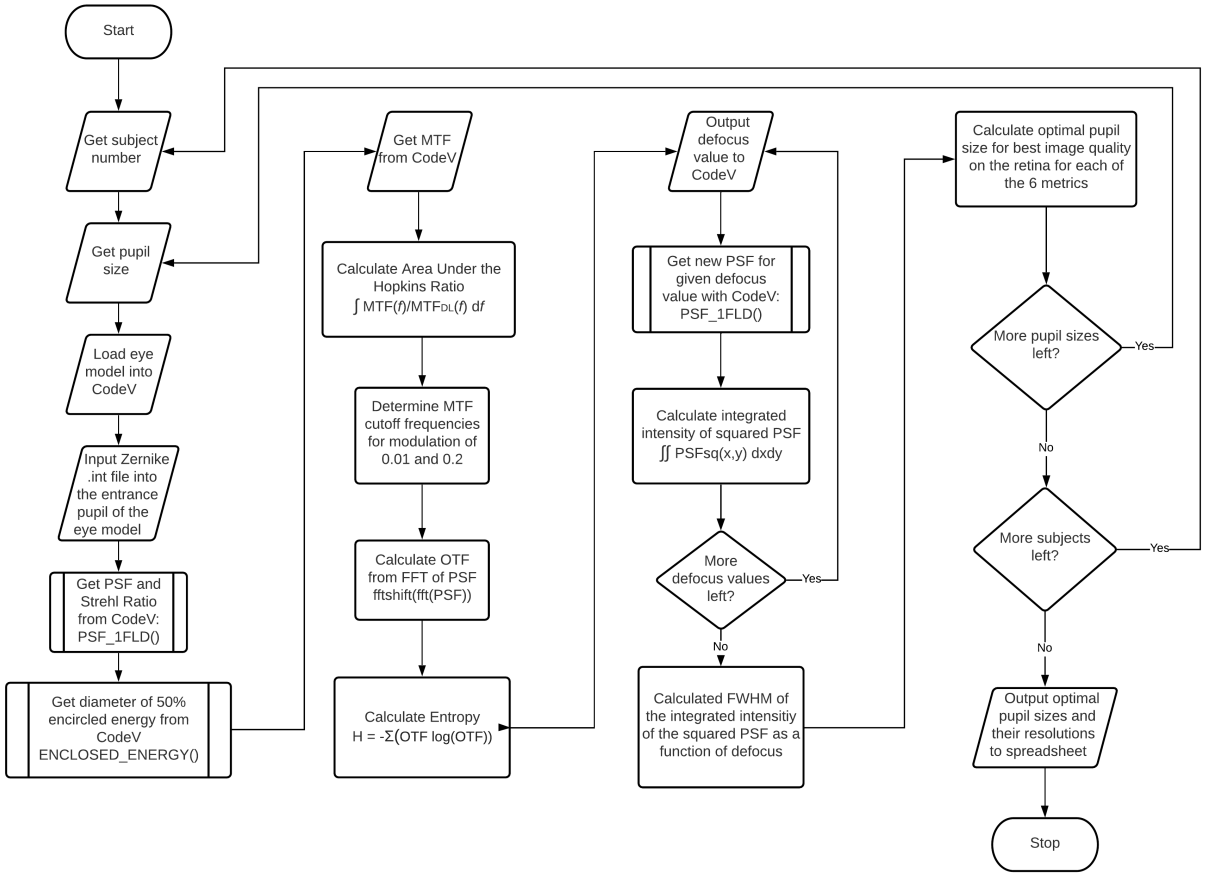

Figure 4.6: Flowchart describing the optimal pupil size determination for each Zernike-polynomial phase plate eye model. Drawn by Hannah Rosenberg; see Statement of Contributions.

Pinhole size

The flowchart illustrated in Figure 4.7 highlights the steps taken to obtain lateral and axial resolution for each pupil size of all subjects, while using an aperture to sample the PSF in the image plane, simulating the effect of a confocal pinhole. This flowchart is nearly identical to the one in Figure 4.6, but it includes an additional loop, which loops over the 7

pinhole sizes used in this study. Only two image quality metrics were assessed as a function of pinhole; lateral resolution measured with EE and axial resolution.

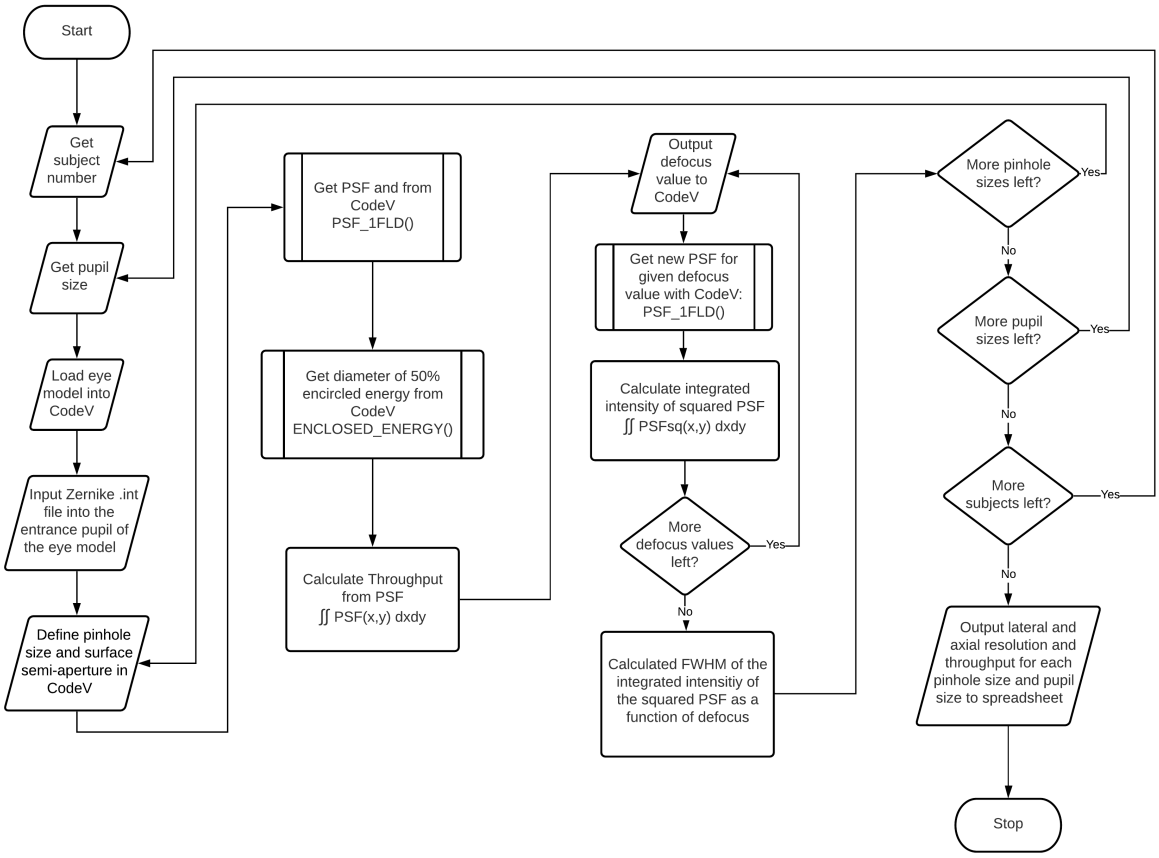

Figure 4.7: Flowchart describing the optimal pinhole size determination for each Zernike-polynomial phase plate eye model. Drawn by Hannah Rosenberg; see Statement of Contributions.

4.3 Results

The relationship between monochromatic HO wavefront aberrations and age is presented in section 4.3.1. In section 4.3.2, average lateral, axial resolution and area under the Hopkins ratio as a function of pupil size determined from 1219 subjects is shown. These plots are also stratified for the four age groups. In addition, the optimal pupil sizes for four image quality metrics that are significantly different with age are further discussed in section 4.3.3. Results from regression analysis identify the relationship between optimal pupil size and RMS wavefront error. Lastly, the optimal pinhole to maximize instrument performance in an SLO or cSLO is presented in Section 4.3.4.

4.3.1 Higher order (HO) root mean square (RMS) wavefront error as a function of age group

The variation of HO RMS wavefront error as a function of age group is presented in figure 4.8. Published results using this data in [150] were computed without regard to trends among subgroups but for the purpose of providing mean Zernike coefficients and RMS values to serve as a reference set for normal, healthy adult eyes [150]. The

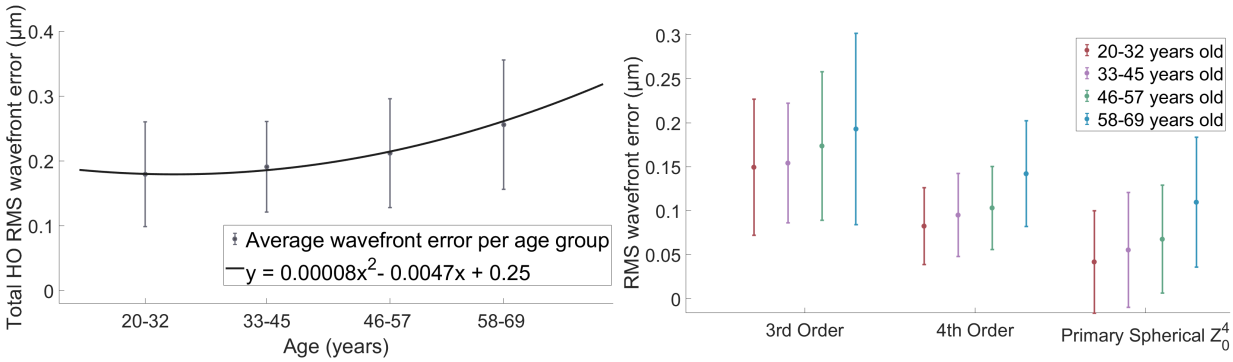

Figure 4.8: [Left](Points) Average HO RMS wavefront error as function of age group. The standard deviation is plotted with the average values as a function of age for a 5.0 mm pupil. (Curve) 2nd order regression line fitted to all the data (R^2= 0.055; p<0.01; Spearman's correlation coefficient, R_s=0.19; n =1219). [Right] 3rd, 4th RMS and primary spherical wavefront error as a function of age for a 5.0 mm pupil. (n=1219; 3rd: R^2=0.025; p<0.05; 4th: R^2=0.073; p<0.01; Z_0^4 coefficient: R^2=0.054; p<0.05). The subject numbers for the 4 age groups, 20-32, 33-45, 46-57 and 58-70 are 588, 416, 172 and 43 respectively.

variation of RMS based on subgroups such as age and ethnicity presented in this section is supplementary to the published work in [150]. The total HO RMS wavefront error increased significantly as a function of age as illustrated in figure 4.8. On average, 3^{rd}, 4^{th} order and spherical aberration Z_0^4 also increased as a function of age. The R^2 value, which describes the goodness of fit, statistically indicated that age poorly explains the variance in total HO RMS wavefront error. In addition, high variability in each age group was demonstrated by the high standard deviation in Figure 4.8. There were individual subjects in the older group with lower HO RMS wavefront error than others in the younger group. This high variability between subjects is consistent with previous studies [40, 73, 81, 82, 121, 150, 173]. Despite the wide variability at each age group, there was a statistically significant relationship between HO RMS wavefront error and age ($p < 0.01$). The Spearman's correlation coefficient ($R_s = 0.19$), a statistical measure of the strength of a monotonic relationship between two data sets, indicated a weak correlation, consistent with previous findings [173]. Therefore, while HO wavefront error varied widely among subjects, there was a significant trend of an average increase of HO wavefront error as a function of age.

A regression analysis with multiple predictors, which is equivalent to a multi-variable fit, was also carried out to identify additional factors that explain the variation in total HO RMS wavefront error. The relationship of HO RMS wavefront error as a function of age, gender, data set, sphere and cylinder was studied. Regression with multiple predictors provided an improved fit but the R^2 value remained low as R^2= 0.162. The fit with the following predictors x1, x2, x3, x4 and x5 corresponding to age, sphere, cylinder, gender and study, respectively, gave the following regression curve of $y = 0.18774 - 0.032782 \cdot x3 - 0.056638 \cdot x4 + 0.00028913 \cdot x1 \cdot x2 + 0.00074496 \cdot x1 \cdot x4 - 0.0053628 \cdot x4 \cdot x5 + 5.9591e-05 \cdot x1^2 + 0.042869 \cdot x4^2$ (p<0.05). Therefore, the variation of HO RMS wavefront error was dependent on, and statistically significant with, cylinder, gender and study, as presented in the equation above. These predictors provided a weak but statistically significant explanation of the variation of HO wavefront error.

4.3.2 Average image quality as a function of pupil size

The effect of both diffraction and wavefront aberrations on optical image quality as a function of pupil size indicated that there is a turning point which provides the optimal pupil size for best image quality, consistent with literature [9, 43, 62, 146]. Figures 4.9, 4.10, 4.11 and 4.12 present the average lateral resolution from EE, area under the HR, axial resolution and lateral resolution from the cutoff frequency as a function of pupil size, respectively, for 1219 subjects. As presented in the previous section, due to the high variability of RMS wavefront error among subjects, it is important to produce such curves

based on large sample sizes. Each image quality metric curve is presented separately for each age group. While entropy was studied, it was excluded from these results since it indicated no statistical significance with age. As described in Section 4.2.2, a two sample Kolmogorov-Smirnov test was used to determine if the curves are statistical significant from each other.

Average lateral resolution determined by the diameter of 50% EE on the retina, based on all subjects, improved with increasing pupil size to a turning point around 2.75 mm where it began to get worse due to the presence of aberrations. As illustrated in Figure 4.9, lateral resolution on average was nearly diffraction-limited for pupil sizes smaller than 1.5mm, consistent with previous published work by Campbell [43]. The shaded area on the left curve in Figure 4.9 is the standard deviation indicating the high variability of lateral resolution among subjects. On the right, in Figure 4.9, the average resolution is presented for each age group. Curves for average lateral resolution as a function of pupil size for each

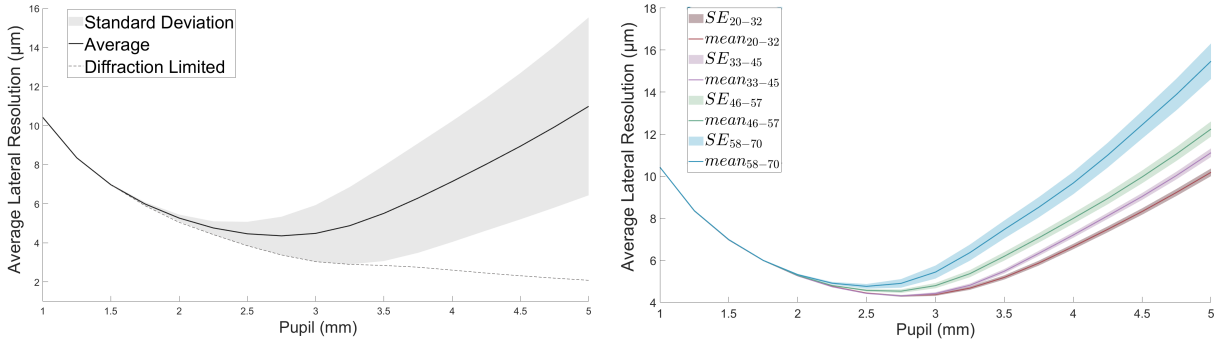

Figure 4.9: Average lateral resolution obtained from encircled energy as a function of entrance pupil. Solid curves indicate the average resolution for each pupil size. [Left] Shaded area is the standard deviation. [Right] Shaded area is the standard error (SE). The subject numbers for the four age groups, 20-32, 33-45, 46-57 and 58-70 are 588, 416, 172 and 43, respectively.

age group were significantly different from each other ($p < 0.05$). As age increased, there was a decline in lateral resolution beyond 2.25 mm. In addition, the deviation from the diffraction limited curve happens at a smaller pupil size for older adults than in younger adults. This was consistent with what one might expect given that the RMS wavefront error on average becomes higher as a function of age [81, 82, 173]. The standard error indicated the high variability of lateral resolution for all subjects but became smaller when age groups were considered separately. There are individual subjects in the older group with better lateral resolution than others in the younger group. HO RMS wavefront error

affects image quality, and subject specific retina image quality affects the optimal pupil size. Therefore, one explanation of the high standard deviation in these results, which increases in the older age group, is the high variability present in the RMS wavefront error discussed in Section 3.3.1.

The average area under the HR as a function of pupil size and age group is presented in figure 4.10. The area under the HR is an image quality metric that gives additional information as it takes into account all spatial frequencies, and thus a larger area under the HR is optimal. The relationship of this metric with pupil size was found to follow a similar trend to that of lateral resolution based on encircled energy. A diffraction-limited eye model resulted in an area under the Hopkins ratio that increased a function of pupil size. Due to the presence of aberration, the area under the Hopkins ratio started to decrease as pupil size increased beyond 2.5 mm, illustrated in Figure 4.10. The deviation from the diffraction limited curve happens at a smaller pupil size for older adults than in younger adults. Average area under the Hopkins ratio for each age group separately is illustrated on the right in Figure 4.10. The average area under the Hopkins ratio as a function of pupil size curves for each age group were found to be significantly different from each other ($p < 0.05$). There was a high standard deviation present in all age group curves consistent with the results obtained for lateral resolution and RMS wavefront error. Unlike the results based on encircled energy, the standard deviation did not increase as the pupil size increased.

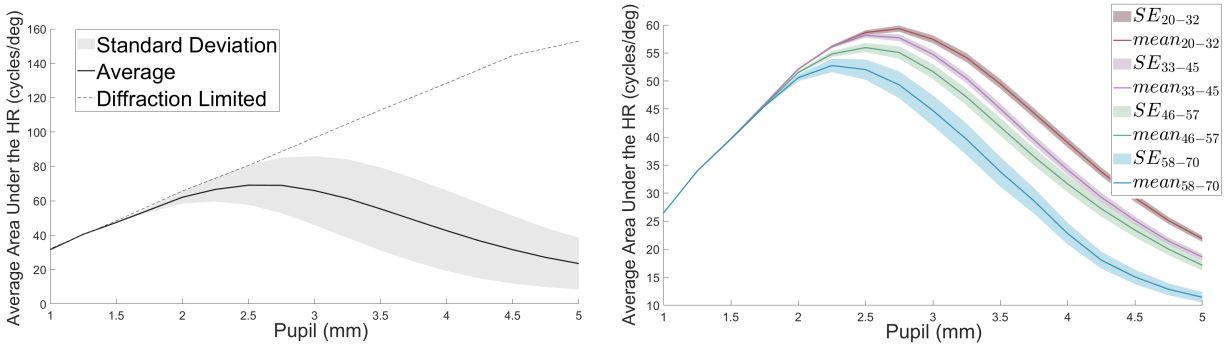

Figure 4.10: Average area under the Hopkins ratio as a function of entrance pupil. Solid curves indicate the average values for each pupil size. The AHR in the diffraction limit is equal to cutoff frequency. [Left] Shaded area is the standard deviation across all participants. [Right] Shaded area is the standard error (SE). The subject numbers for the four age groups, 20-32, 33-45, 46-57 and 58-70 are 588, 416, 172 and 43, respectively.

Average axial resolution as a function of entrance pupil sizes is illustrated in Figure 4.11. In the case of a diffraction-limited eye, axial resolution improved exponentially with increasing pupil size. The deviation of axial resolution from the diffraction limited curve happens at approximately 2.5 mm for younger adults and at a slightly lower pupil for older adults. When aberrations were included, average axial resolution improved up to a turning point of around 3.5mm. Beyond this turning point, the rate of decline for axial resolution decreases with increasing pupil size. Curves of average axial resolution as a function of pupil

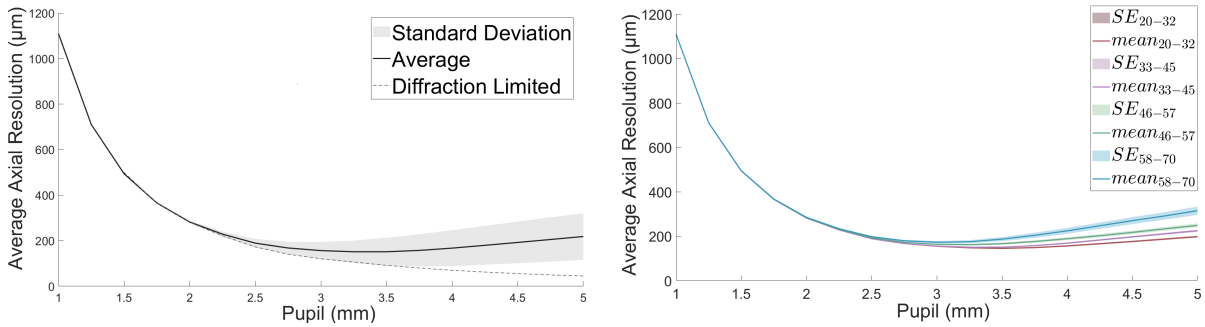

Figure 4.11: Average axial resolution as a function of entrance pupil. Solid curves indicate the average resolution for each pupil size. [Left] Shaded area is the standard deviation. [Right] Shaded area is the standard error (SE). The subject numbers for the four age groups, 20-32, 33-45, 46-57 and 58-70 are 588, 416, 172 and 43, respectively.

size for each age group are illustrated on the right of Figure 4.11. Average axial resolution as a function of pupil size curves for each age group were found to be significantly different from each other ($p < 0.05$). The high standard deviation was consistent with the results of other metrics where high variability was present.

An additional method to determine lateral resolution is to use the cutoff frequency of each MTF. The average lateral resolution determined from the cutoff resolution, which is expressed in Equation 4.28, as a function of pupil and age is illustrated in Figure 4.12. Consistent with the other metrics, average resolution improved for increasing pupil size but only to a turning point of around 2.75 mm where lateral resolution from the cutoff frequency became worse due to the presence of aberrations. The cutoff frequency method, in comparison to the diameter of 50% encircled energy method, introduced higher variability in the results as indicated by the high standard error and strange shape of the older age group. This can be observed when comparing Figures 4.9 and 4.12. The high variability stems from the fact that it is a challenge to identify precisely the cutoff frequency. The lateral resolution curves, as a function of pupil size, for each age group are shown on the right of Figure 4.12. Only the older group with respect to the younger groups was found to

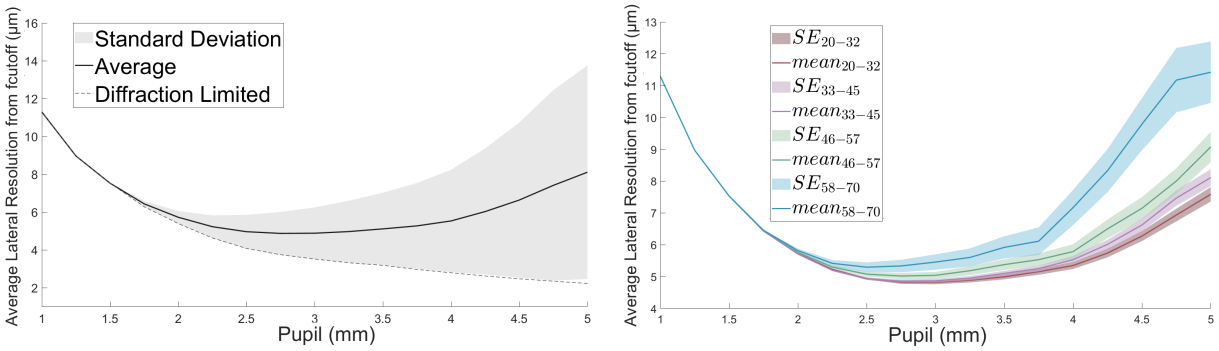

Figure 4.12: Average lateral resolution obtained from the cutoff frequency as a function of entrance pupil. Solid curves indicate the average resolution for each pupil size. [Left] Shaded area is the standard deviation. [Right] Shaded area is the standard error (SE).The subject numbers for the four age groups, 20-32, 33-45, 46-57 and 58-70 are 588, 416, 172 and 43, respectively.

be statistically different ($p < 0.05$). The lack of precise identification of the cutoff spatial frequency of the MTFs which is required to determine lateral resolution, could be due to the presence of extensive contract reversal. Contrast reversal is directly related to the sign reversal in the real part of the OTF. This means that the MTF which is obtained by the magnitude (absolute value) of the OTF, neglecting the phase information, may not reach zero but simply reaches a minimum point modulation. To overcome this issue and identify the cutoff spatial frequency, the spatial phase information was used to identify when contrast reversal occured and to estimate the actual cutoff frequency in cases where the modulation did not reach almost zero. In addition, due to the fact that only higher order aberrations were used in the eye models, excluding defocus, the MTFs were less prone to approach modulations as low as zero. In conclusion, this method is not as precise as the other metrics of image quality used in this study.

4.3.3 Optimal pupil size as a function of age group

The optimal pupil size for each optical performance metric, presented in the previous section, was determined for each subject. Optimal pupil sizes were selected as the ones that gave the best optical quality on the retina. Average entrance pupil size values and standard deviations for each age group are presented in tables 4.1 and 4.2. These values were obtained by averaging the subject specific optimal pupil sizes for each age group.

		Lateral Resolution (EE)		Lateral Resolution (f_{cutoff})	
	RMS (μm)	OPS (mm)	LR (μm)	OPS (mm)	LR (μm)
20 - 32 years					
AVG	0.1790	3.09	3.95	3.34	4.28
SD	0.0808	0.488	0.654	1.00	1.05
33 - 45 years					
AVG	0.1911	3.00	4.06	3.32	4.37
SD	0.0698	0.430	0.543	1.01	0.998
46 - 57 years					
AVG	0.2118	2.89	4.19	3.30	4.46
SD	0.0841	0.471	0.639	1.04	1.13
58 - 70 years					
AVG	0.2556	2.73	4.48	2.95	4.71
SD	0.0996	0.402	0.654	0.858	1.14

Table 4.1: Optimal pupil sizes (OPS) for best lateral resolution (LR). Root-mean-square (RMS) wavefront error at a 5 mm pupil for each age group is presented. The subject numbers for the four age groups, 20-32, 33-45, 46-57 and 58-70 are 588, 416, 172 and 43, respectively.

In table 4.1 average RMS wavefront error and optimal pupil size determined by the diameter of 50% EE were found to be significantly different as a function of age. The optimal pupil size determined by the cutoff frequency was significantly different between individuals aged 58-70, compared to all other age groups($p < 0.05$). No other age groups were significantly different. All optimal pupil sizes presented in table 4.2 for area under the Hopkins ratio and axial resolution were significantly different for each age group.

When studying Figure 4.9 in conjugation to table 4.1, I determined that if the optimal pupil size for younger adults (2.73mm) was used in older adults, then the resolution would be on average $0.53\mu m$ worse. If the optimal pupil size for best axial resolution for younger adults was used in older adults, then the axial resolution would be on average $26.4\mu m$ worse

as determined by Figure 4.11 and table 4.2. Both the average lateral and axial resolution were found to be significantly differenct as a function of age group.

	Area Under the Hopkins Ratio		Axial Resolution	
	OPS (mm)	AHR ($\frac{\text{cycles}}{\text{degrees}}$)	OPS (mm)	AR (μm)
20 - 32 years				
AVG	2.70	65.2	3.64	128
SD	0.531	11.3	0.577	42.8
33 - 45 years				
AVG	2.62	63.1	3.54	134
SD	0.473	9.9	0.556	35.3
46 - 57 years				
AVG	2.59	61.5	3.41	143
SD	0.527	10.9	0.538	39.8
58 - 70 years				
AVG	2.41	57.5	3.24	157
SD	0.420	9.08	0.455	36.4

Table 4.2: Optimal pupil sizes (OPS) for best axial resolution (AR) and area under the Hopkins ratio (AHR) averaged across subjects in each age group. The subject numbers for the four age groups, 20-32, 33-45, 46-57 and 58-70 are 588, 416, 172 and 43, respectively.

4.3.4 Optimal pupil size as a function of HO wavefront error and age across individuals

A regression of optimal pupil size across individuals as a function of their HO RMS wavefront error at 5 mm and age gave an exponential fit with $R^2 = 0.754$ presented in Figure 4.13. This was a good fit which statistically indicated that 75.4% of variability in optimal pupil size is explained by HO RMS wavefront error and the product of age with HO RMS wavefront error. An age factor alone was not statistically significant and not a determining factor for optimal pupil size. In addition, the Spearman's correlation coefficient ($R_s = -0.85$), a statistical measure of the strength of a monotonic relationship between two data sets, indicated a strong correlation between optimal pupil size and HO wavefront error. The Spearman's correlation coefficient of optimal pupil size and age ($R_s = -0.17$) indicated a weak correlation. Therefore, based on the results presented in Figure 4.13 HO RMS wavefront error is a good predictor of optimal pupil size for best lateral resolution. Although it is not illustrated here, it was found that on average optimal pupil sizes of the older age group were lower than the optimal pupil sizes for other age groups, which is consistent with aberrations being larger in older adults. A regression between optimal pupil size for best lateral resolution and best lateral resolution from the 50% EE is presented in Figure 4.14. Based on this data set, 88.7% of variability of lateral resolution $R^2 = 0.754$ was explained by the optimal pupil size for best lateral resolution.

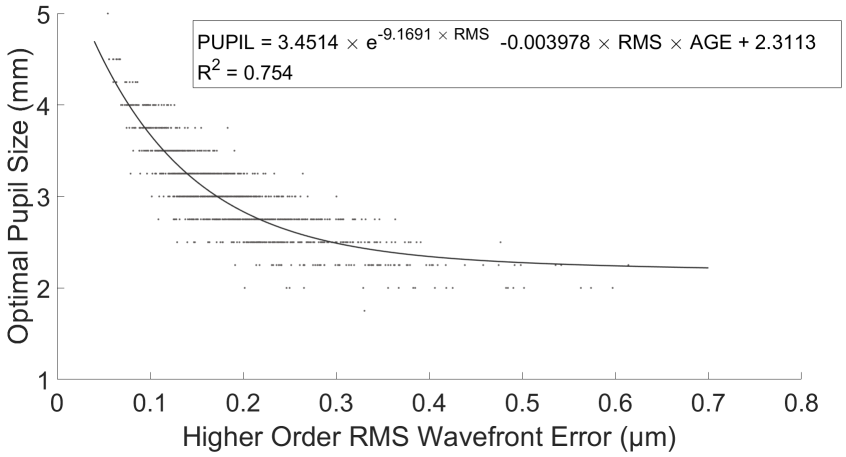

Figure 4.13: Exponential regression fit of optimal pupil size as a function of HO wavefront error and age ($n = 1219, p < 0.05$)

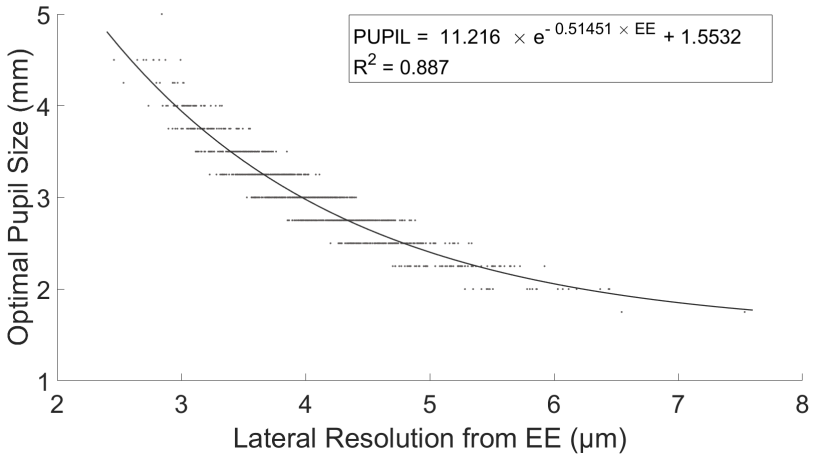

Figure 4.14: Optimal pupil for best lateral resolution as a function of encircled energy (EE) ($n = 1219, p < 0.001$)

4.3.5 Optimal pinhole sizes for improved resolution

In the model of a perfect diffraction-limited eye, when the confocal pinhole decreased in size, resolution on the retina improved while throughput decreased and would plateau at pinhole sizes half the PSF diameter . However, using the optimal pupil sizes determined in Section 3.3.3, pinhole sizes smaller than 1.5 TDL resulted in low throughput values. Low throughput corresponds to low signal to noise ratio (SNR), causing degradation in resolution for pinhole sizes smaller than 1.5 TDL.

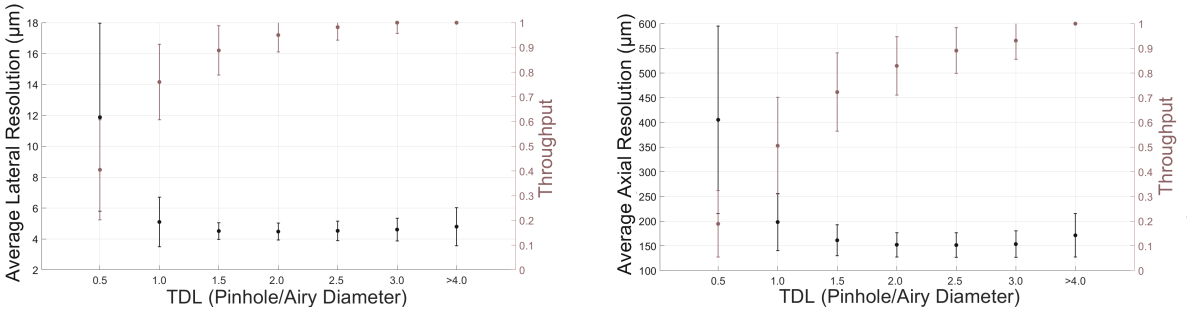

Figure 4.15: Average resolution and throughput for varying TDLs for subjects 58-70 years old. [Left] Average lateral resolution for participants with an optimal pupil size of 2.75 mm as a function of pinhole size. [Right] Average axial resolution for participants with an optimal pupil size of 3.25 mm as a function of pinhole size.

It was determined that the optimal pinhole size ranges between 1.5-2.5 TDL when using optimal pupil sizes determined from Figure 4.15. This result was consisted for all age groups. Results of the older age group, using optimal pupil sizes, for best lateral and best axial resolution are illustrated in Figure 4.15. Equivalent results for younger adults are in Apendix A. Lastly, it was determined that there was no age dependence of optimal pinhole size when using the optimal pupil size for each age group.

4.4 Discussion

Average optical performance progressively declines with age in the human eye [81, 82]. In this study, I confirmed that average HO RMS wavefront error, based on 1219 subjects, increased as a function of age. Despite the high variability among subjects, there was a statistically significant relationship between HO RMS wavefront error and age. This finding is consistent with the published works by several research groups, which document an increase of monochromatic ocular wavefront aberrations as a function of age and the presence of high variability among subjects [4, 40, 71, 73, 81, 82, 121, 150, 173].

Curves of average lateral resolution, area under the Hopkins ratio and axial resolution as a function of pupil size were presented, which demonstrated the effect of both diffraction and wavefront aberrations on optical image quality. Consistent with literature [9, 43, 62, 146], all curves had a turning point at the optimal pupil size. These curves were also plotted for each age group demonstrating that for each age group there is a different average optimal pupil size. Older adults displayed a more rapid decline in image quality than younger subjects as pupil size increased. The values of optimal pupil size for each image quality metric were presented in Section 4.3.3. Average optimal pupil sizes for best lateral resolution, area under the Hopkins ratio and axial resolution were significantly smaller in older adults, consistent with aberrations increasing in older adults [4, 121]. This suggests that the design of imaging systems to be used with older eyes should differ from those used with younger eyes.

Each image quality metric can be used for a different purpose. The EE metric can estimate lateral resolution well and it is 7% different from the theoretical lateral resolution or the resolution determined by the cutoff frequency, in the diffraction-limit. Overall, it is a reliable image quality metric and can account for the asymmetry in aberrated PSFs. While the cutoff frequency is another reliable method used to access lateral resolution, in this study it was found particularly difficult to identify reliably the cutoff frequency due to contrast reversal. Thus, in this study it was not used to identify optimal pupil sizes. The area under the HR is a global measure of image quality that reports on the image

quality for all spatial frequencies. Here, it provides optimal pupil sizes close to those for best EE. Although high depth sectioning is not possible with SLO and cSLO systems that are used with the eye without adaptive optics correction, the axial resolution gives insight onto optimal pupil size that could provide at least some optical sectioning through the retina. The method of calculating axial resolution in this study gave a 10% difference from axial resolution determined by theoretical equations, in the diffraction limit.

In addition, the optimal pupil values for best lateral and axial resolution are consistent with preceding work on optimal pupil size, considering that the sample size used in those studies was significantly smaller [43, 62]. Although the 16 subjects studied by Donnely and Roorda were young (20-35 years old), their reported HOAs were higher, resembling those of older adults in the study presented in this chapter [62]. While the standard deviation in both studies is high, the variability presented in this study is significantly less than the variability presented in the work by Donnelly and Roorda. It is likely that this result is due to the larger sample size used in the present study. Further, it is very likely that high variability of optimal pupil size stems from the high variably of HO wavefront error among subjects.

Furthermore, it was determined that optimal pinhole size ranges between 1.5-2.5 TDL when using optimal pupil sizes and there was no age dependence. Since it was determined that there is a linear realtionship between best TDL and entrance pupil size, larger TDL values should be used when using larger entrance pupils, outside the range of optimal sizes. This is consistent with ocular aberrations increasing for larger pupils [9, 146]. The optimal pinhole sizes suggested in this study are similar in compared to those used by Izatts group [107]. However, Izatts group obtained results in an experimental setting using different image quality metrics and a different optical resolution target. One difference is that since scattering is not considered in this study, throughput is higher than what one might expect in an experimental setting as observed in Izzat's results when comparing throughput values as a function of pinhole size [107]. In addition, Izatt used sharpness to determine image quality. Sharpness was defined as "the ratio of the L2 norm of the high-passed image region and the L2 norm of the low-pass image region" [107]. In Izatt's study, photoreceptors were imaged at an eccentricity of 4.2 degrees. Since the cone spacing varies with eccentricities, it was feasible to image cones further from the fovea as described by Merino[123] and Curcio et al.[57]. Therefore, Izatt was targeting lower spatial frequencies corresponding to 9.7μm resolution [57, 107, 123] in comparison to this study where the optimal resolutions presented in tables 4.1 and 4.2 were the target. Furthermore, Izzat's work used a constant entrance pupil of 2.5 mm for a single subject [107]. In spite of the differences between Izatt's study and the one reported here, the recommendations for optimal confocal pinhole sizes in terms of TDL are similar. However, the recommendations are a function of the

pupil sizes used and these differ in the two studies, leading to different absolute pinhole sizes.

The results presented in this study were documented based on a large data set ($n = 1219$), providing age dependence and obtained in a theoretical setting, making this study unique from others. It was determined that selecting a pupil size specific to an age group could significantly improve the optical quality. Figures 4.9, 4.10, 4.11 and 4.12 could assist with optimized instrumentation design in order to maximize image quality on the retina and subsequently improve image quality of the retinal images.

In section 4.3.4, it is shown that HO RMS wavefront error is a good predictor of optimal pupil size. In the presence of instrumentation that can identify the RMS wavefront error of an individual, figures 4.13 provide the ability to determine an optimal entrance pupil as described in Section 4.3.3. Alternatively, if one has no way to determine the individualized RMS wavefront error, using the graphs of image quality as a function of pupil size from the previous section could determine the best pupil size. Using optimal pupil size in the design of SLO instrumentation, would be a good way to obtain high resolution retinal imaging even without the use of adaptive optics as previously attempted in [107].

Chapter 5

Optimization of confocal scanning polarimeter design considering the double-pass retinal reflection

5.1 Introduction

In-vivo imaging of the human retina is a unique optical process because the retina is not directly accessible, so imaging must be done in a conjugate plane outside the eye. The image obtained at this optically conjugate plane stems from the double-pass reflection, in which light enters the eye, scatters from within the retina, and then exits the eye. Therefore, the resulting image is one reflection, which happens after the light travels twice through the ocular optics [12, 14, 149]. Modalities for imaging the human retina using the double-pass reflection have been developed for many years [14, 107, 149, 177, 178, 181]. Conventional direct and indirect opthalmoscopes have been used extensively because they are simple [166]. However, direct opthalmoscopes have poor image quality and small fields of view [166, 177]. With conventional fundus cameras, the illuminating beam passes through the periphery of the pupil and the reflected light is detected through the center of the pupil, achieving a larger field of view (FOV) than the direct or indirect opthalmoscope setups [59, 134]. One of the most significant shortcomings of conventional fundus photography is that imaging is uncomfortable for the subject since high intensity light levels are used and an invasive agent is utilized to dilate the eye pupil [22, 116, 117, 181, 185]. A major advancement in ophthalmoscopy was the invention of the scanning laser opthalmoscope (SLO), first presented by Webb [177]. The SLO uses a monochromatic illumination source

and a scanning unit, enabling improved contrast and optical quality in retinal images. In the SLO, a fundus image is generated by a beam raster scanned onto the retina. The reflected light is then recorded by a detector. The entrance and exit pupils are inverted so that a narrower laser beam is focused to a compact point on the retina, and the reflected light that passes through the large exit pupil is detected. This setup permits lower intensity illumination, which results in better comfort for the patient [177]. A later development, the confocal scanning laser opthalmoscope (cSLO), uses a confocal aperture prior to the detector, which is usually optically conjugate to the illumination spot on the retina [178]. The cSLO further reduces out of focus scattering in the image plane by blocking light scattered from planes and points other than the illumination spot [107, 177, 178, 181]. In retinal imaging, as the diameter of the confocal aperture is reduced, the depth of focus of the imaged layer is improved at the expense of detected intensity [107, 178, 181].

In this chapter, I present two ways to modify the MM confocal scanning polarimeter presented in Chapter 3 in order to improve lateral resolution when targeting amyloid-β deposits on the retina. Since the confocal scanning polarimeter is designed as an Alzheimer's disease (AD) diagnostic tool that will be used in older adults, the optical system is further optimized for the older population using findings presented in Chapter 4 and extended in this chapter. I first present an optimized small entrance pupil cSLO design and derive the double-pass expression that describes resolution. I then present an optimized large exit pupil cSLO design and derive the double-pass expression. The derivations presented in this chapter are based on the mathematics of the double-pass reflection previously described by Roorda and Artal [14, 149]. Lastly, I present the optical designs for both retinal instruments and evaluate image quality using Code V.

5.1.1 The Double-pass reflection

The double-pass reflection has been widely used to determine retinal image quality in the human eye [12, 14, 43, 146, 149]. The double-pass point spread function (PSF) described by Roorda et al. and Artal et al. [14, 149] is presented in this section. A PSF is defined as the response of an imaging system to a point source. The image or amplitute response of an imaging system can be expressed using the Superposition integral, described by Roorda and is given by the convolution of the PSF with the ideal image predicted by geometrical optics [149]:

$$U_i(x_i, y_i, z_i) = \iiint_{-\infty}^{\infty} e^{-ikz_o} h(\frac{x_i}{m} + x_o, \frac{y_i}{m} + y_o, \frac{z_i}{m^2} + z_o) U_g(x_o, y_o, z_o) dx_o dy_o dz_o \qquad (5.1)$$

where z is the distance along the optical axis, h is the PSF, U_g is the ideal image predicted by geometrical optics, m is the magnification difference between the object and image planes and U_i is the actual image. Object and image coordinates are x_o, y_o, z_o and x_i, y_i, z_i, respectively. Because the optical system of the eye is linear, the superposition integral can be used, representing the object as a superposition of many images from an array of point sources [149].

The spatial coordinates in the object plane x, y, z, in the retina plane x', y', z' and in the plane outside the eye x'', y'', z'' are used to mathematically describe the PSF. The amplitude response of an imaging system is given by the superposition integral, where U_2 defines the retinal image of an object U_{obj}, and h_{in} is the single-pass PSF through the eye's optics [149].

$$U_2(x', y', z') = \iiint_{-\infty}^{\infty} e^{-ikz} U_{obj}(x, y, z) \cdot h_{in}(\frac{x}{m} + x', \frac{y}{m} + y', \frac{z}{m^2} + z')dxdydz \tag{5.2}$$

The superposition integral in Equation 5.2 is equivalent to the convolution of the PSF with the imaged object [149]. Using the assumption that the object is an infinitely small illumination spot, U_{obj} can be represented as a delta function, $U_{obj}(x, y, z) = \delta(x, y, z)$. U_2 is then defined as:

$$U_2(x', y', z') = \iiint_{-\infty}^{\infty} e^{-ikz} \delta(x, y, z) \cdot h_{in}(\frac{x}{m} + x', \frac{y}{m} + y', \frac{z}{m^2} + z')dxdydz \tag{5.3}$$

Equation 5.3 is then further reduced to Equation 5.4, which indicates that the PSF is projected onto the retina in the first-pass.

$$U_2(x', y', z') = h_{in}(x', y', z') \tag{5.4}$$

In the double-pass reflection, the PSF projected onto the retina in the first-pass, scatters and becomes the source for the second-pass, defined as U_r. The superposition integral is used to predict the amplitude in the image plane outside the eye using U_r as the source [149]. The retina reflectance function is represented with $R(x', y', z')$.

$$U_r(x', y', z') = R(x', y', z') \cdot h_{in}(x', y', z') \tag{5.5}$$

Equation 5.5 defines the source in the second-pass which is described by the input PSF multiplied by the complex retinal reflectance function $R(x', y', z')$.

$$U_3(x'', y'', z'') = \iiint_{-\infty}^{\infty} e^{-ikz} U_r(x', y', z') \cdot h_{out}(x'' + mx', y'' + my', z'' + m^2 z')dx'dy'dz' \tag{5.6}$$

By substituting Equation 5.5 into 5.6, the double-pass PSF is expressed as:

$$U_3(x'', y'', z'') = \iiint_{-\infty}^{\infty} e^{-ikz} R(x', y', z') \cdot h_{in}(x', y', z') \cdot h_{out}(x''+mx', y''+my', z''+m^2 z') dx' dy' dz' \tag{5.7}$$

The total intensity in the image plane is the square of the magnitude of the amplitude U_3, described in Equation 5.8 . Using the assumption that the retinal surface is a single, diffuse-scattering layer at the ideal image plane, then the retinal reflectance function can be written as $R(x', y')\delta(z')$ and the equation reduces to [14, 149]:

$$I_3(x'', y'') = \left| \iint h_{in}(x', y') R(x', y') h_{out}(x'' + mx', y'' + my') dx' dy' \right|^2 \tag{5.8}$$

In the cSLO, a detector is used to measure the intensity transmitted through the confocal aperture. In this way the double-pass PSF with a confocal aperture is defined by [149]:

$$I_{SLO}(x'', y'') = \left| \iint h_{in}(x', y') R(x', y') h_{out}(x'' + mx', y'' + my') D(x'', y'') dx' dy' \right|^2 \tag{5.9}$$

Equation 5.9 determines the intensity for a single pixel as the reflected light is detected through a confocal pinhole $D(x', y')$. For a scanning system, the position of the illuminated spot for a single scan position in retinal space is denoted as (x''_s, y''_s). To simplify this expression, Roorda presents Equation 5.9 using a convolution. For a scanning beam with a confocal aperture, the intensity per scan position or pixel is shown in Equation 5.10. Convolution is symbolized using $\circledast$.

$$I_{SLO} = \left| \iint h_{in}(x'', y'') \cdot R(x'', y'') \cdot [h_{out}(x'', y'') \circledast D(x'', y'')] dx'' dy'' \right|^2 \tag{5.10}$$

Finally, Equation 5.11 described the intensity of a scanning beam at each point during the scan. Thus, the intensity at each position of the scanning spot is the convolution of the square of the PSF with the complex retinal reflectance function.

$$I_{SLO}(x''_s, y''_s) = \left| [h_{in}(x''_s, y''_s)] \cdot [h_{out}(x''_s, y''_s) \circledast D(x'', y'')] \circledast R(x''_s, y''_s)) \right|^2 \tag{5.11}$$

5.1.2 Optical resolution characterization using the double-pass reflection

Roorda in his work characterized image quality and discussed implications of the double-pass PSF for three imaging techniques including the conventional fundus imaging, non-confocal SLO and cSLO [149]. In this section, I present Roorda's findings which will be used as a reference and comparison to the derivations presented in the results section.

Conventional fundus photography

In conventional fundus photography, a large area of the fundus is illuminated in the first-pass. With a large source conjugate with the retina, the retinal illumination is a convolution of the large source with the first-pass PSF. Since the area of the source is much greater than the first-pass PSF, the illumination will be uniform on the retina [149]. Therefore, the input PSF, h_{in}, can be represented by a constant C_1 in Equation 5.12 [149].

$$U_r(x', y') = C_1 \cdot R(x', y') \tag{5.12}$$

Using the superposition integral the double-pass reflection in conventional fundus photography is described by Equation 5.13.

$$U_{\text{Fundus Imaging}}(x'', y'') = C_1 \iint_{-\infty}^{\infty} R(x', y') \cdot h_{out}(x'' + \frac{x'}{m}, y'' + \frac{y'}{m}) dx' dy' \tag{5.13}$$

The image intensity in fundus photography is described by a convolution of the second-pass PSF with the complex retinal reflectance function, presented in Equation 5.13. The constant C_1 is dropped since it is only a scaling factor.

$$I_{\text{Fundus Imaging}} = \left| h_{out}(\frac{x''}{m}, \frac{y''}{m}) \circledast R(\frac{x''}{m}, \frac{y''}{m}) \right|^2 \tag{5.14}$$

Equation 5.14 describes that fundus imaging is affected by the single-pass for light leaving the eye in the second-pass. Therefore, image quality is determined by the pupil in the second-pass (exit pupil) and is independent of the pupil size on the first-pass.

Non-confocal SLO

The non-confocal SLO setup can be derived by assuming a large detector area. A large detector area is realized by modeling the large detector as a constant. Using Equation 5.11, the convolution of h_{out} and D can be approximated as a constant. In the large detector limit, the intensity of the image is described as [149]:

$$I_{SLO}(x_s'', y_s'') = \left| [h_{in}(x_s'', y_s'')] \circledast R(x_s'', y_s'')) \right|^2 \tag{5.15}$$

Therefore, in the non-confocal SLO image quality is primarily influenced by the first-pass PSF. In order to maximize the collected light, the exit pupil can be increased without resolution loss due to an increase in aberrations [149, 177].

Confocal SLO

The intensity per scan position is shown in equation 5.11. In the limit where the confocal pinhole in infinitely small, $D(x'', y'')$ is represented as a delta function and Equation 5.11 reduces to [149]:

$$I_{cSLO}(x''_s, y''_s) = \left|[h_{in}(x''_s, y''_s) \cdot h_{out}(x''_s, y''_s)] \circledast R(x''_s, y''_s))\right|^2 \tag{5.16}$$

In addition, the complex reflectance function can be represented as a delta function, where the imaged feature is an isolated point scatter at the cetner of the FOV, and the equation reduces to:

$$I_{cSLO}(x''_s, y''_s) = \left|[h_{in}(x''_s, y''_s)][h_{out}(x''_s, y''_s)]\right|^2 \tag{5.17}$$

Equation 5.17 indicates that the cSLO is influenced by the ocular optics in the first and second passes. The lateral resolution advantage of the confocal ophthalmoscope over conventional fundus imaging is shown in equation 5.17. As Roorda explained, the PSF of the confocal ophthalmoscope is the square of the single pass PSF when the input and output PSFs are the same as indicated by Equation 5.18. For a diffraction-limited system, the cSLO has a PSF whose FWHM is 1.4 times narrower than the single pass PSF [149, 156].

$$I_{CSLO}(x''_s, y''_s) = \left|[h_{in}(x''_s, y''_s)]^2\right|^2 \tag{5.18}$$

5.1.3 Optical resolution target for imaging amyloid-β deposits in older adults

The confocal scanning polarimeter, presented in Chapter 3, is intended to be used as a diagnostic tool that identifies biomarkers of Alzheimer's disease, which are amyloid-β deposits. Amyloid-β deposits are conveniently present in the neural retina [47] and are the optical target of the confocal scanning polarimeter.

Based on cumulative histograms of proportion of *ex-vivo* deposits as a function of major and minor axis generated by members of Campbell labs, a target resolution of approximately 10 μm was selected, enabling detection of nearly all deposits. Using optimal pupil sizes for older adults, presented in Chapter 4 and extended to an imaging wavelength of 830 nm, which is presented in the next section, it is possible to accomplish a 10 μm optical resolution in the older eye. Similar to optical resolution, the FOV, which is also limited by the ocular optics, is another important design constraint for developing a reliable AD diagnostic tool. Members of Campbell labs have studied the distribution and size of deposits in *ex-vivo* flatmounted retinas. It was initially found that the retina amyloid-β

deposits were more dense in the center of FOV but it was then confirmed that the density of deposits is almost uniform across the retina [47]. The FOV of the confocal scanning polarimeter, presented in Chapter 3, is 100 and 65 degrees defined from the center of the eye, and from the posterior nodal point, respectively. A 100 degree FOV that was defined from the center of the eye was proven on *ex-vivo* tissue to be sufficient in identifying amyloid-β deposits and determining AD severity [47]. In conclusion, previous work conducted in Campbell labs identified that it is not necessary to image deposits in the far periphery of the retina enabling a simplified design of the live-eye diagnostic instrument. Further, it was determined that enough amyloid-β deposits are large enough to be resolved *in-vivo* and used as a diagnostic without the use of adaptive optics [47].

5.2 Methods

Two optimized confocal scanning polarimeter setups were designed in Code V to achieve the desired optical resolution. Additional design requirements were to maintain the system diffraction limited, the large FOV and a compact system. The two optimized MM polarimeter setups designed and presented use a small entrance beam and a conventional large exit beam SLO with an optimal exit pupil and an optimal entrance pupil, respectively. In addition, image quality was characterized and implications of the double-pass PSF for these setups is discussed. The double-pass formulation presented by Roorda and Artal was used as a benchmark [14, 149].

Furthermore, to maximize lateral resolution on the retina, the optimal pupil size for best lateral resolution in older adults was implemented. Since Zernike polynomial coefficients are wavelength specific as described by Salmon et al. [150], the optimal pupil size identified in Chapter 4 had to be re-evaluated for an 830 nm imaging wavelength, and is presented in Section 5.3.1. The wavelength dependence of Zernike polynomial coefficients (in microns) have been identified by various authors as being either relatively constant or slightly increasing with wavelength [17, 70, 118, 151, 165]. In addition, the chromatic aberration of the eye was further determined to not have an age dependence [89, 175]. The chromatic correction described by Salmon et al. in the COAS Shack-Hartmann Aberrometer was used to convert the older eye Zernike coefficients from 550 nm to 830 nm. The correction is described as follows where ${}^{\lambda}c_n^m$ is the Zernike coefficient at a specific wavelength [151]:

$$ {}^{830}c_n^m = \left(\frac{n_{830}-1}{n_{550}-1}\right){}^{550}c_n^m \tag{5.19} $$

Thibos et al. identified experimentally the chromatic difference, n_λ, of refraction as a

function of wavelength [165]. Using these findings Thibos et al. derived an equation that predicted the dispersion and monochromatic aberrations of an improved reduced model eye using water as the medium and an aspherical refracting surface [165]. n_λ at a given wavelength, λ was defined in [165] as $n_\lambda = 1.320535 - \frac{4.685}{\lambda - 214.102}$ as described by Salmon et al. in [151]. Thus, the chromatic correction is calculated to be very small, $\frac{n_{830}-1}{n_{550}-1} = 1.0207$, giving a nearly constant trend, consistent with other previous findings [17, 70, 118]. By using this chromatic correction for the Zernike coefficients in older adults, a new optimal pupil size for best lateral resolution was identified at the imaging wavelength of the donated SLO at 830 nm, using analysis presented in Chapter 4. Additional work on chromatic aberrations, has identified other methods to calculate the index of refraction of ocular structures as a function of wavelength [17]. However, these methods will be studied as a part of future extension of this work.

An optimal entrance pupil in the case of the conventional SLO setup and an optimal exit pupil for the SLO with a small entrance pupil were determined, which are identified in Section 5.3.1. Lastly, the optimal pinhole size, which is optically conjugate to the retina, was introduced in both setups to reduce out of focus, back-scattering light. Image quality analysis was carried out in Code V. The impact of the proposed instrument modifications was identified by comparing the MTFs of the original and modified optical systems using an individual eye with average monochromatic aberrations of older adults.

5.3 Results

The optimal pupil sizes of older adults for best lateral resolution at an imaging wavelength of 830 nm are identified in Section 5.3.1. Two MM confocal scanning polarimeter setups optimized to achieve high resolution imaging of retinal amyloid-β deposits in older adults are presented in Sections 5.3.2 and 5.3.3.

5.3.1 Calculation of optimal pupil size for best lateral resolution with wavelength in older adults

Zernike polynomial coefficients provided at 550 nm were converted to their corresponding values at 830 nm, the imaging wavelength of the MM confocal scanning polarimeter, using the chromatic correction explained by [151] and outlined in Section 5.2. Average lateral resolution determined from encircled energy (EE) as a function of pupil size is presented in Figure 5.1 for the older adult population (λ = 830). In addition, the average

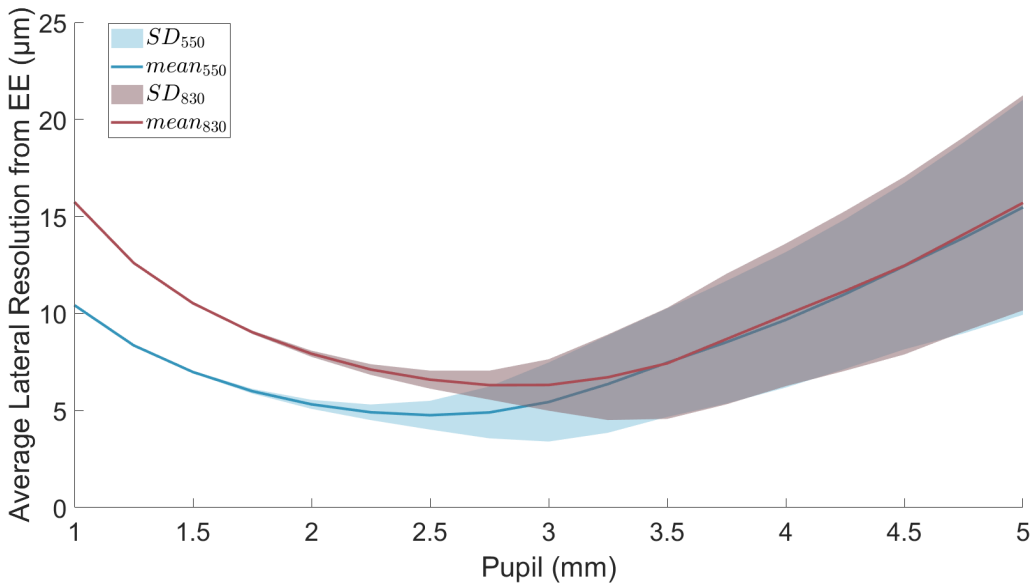

Figure 5.1: Average lateral resolution based on encircled energy as a function of pupil size in older adults, 58-70 years (n=43). Solid curves indicate the average resolution for each pupil size. Shaded area is the standard deviation. Blue and red curves correspond to 550 nm and 830 nm imaging wavelengths, respectively.

lateral resolution determined in Chapter 4 ($\lambda = 550$) is presented on the same curve for comparison. It is evident that in the absence of aberrations, the radius of 50% encircled energy and the PSF increase by the ratio of the two wavelengths, $830/550 = 1.509$. However, in the presence of aberrations, higher wavelengths do not introduce significant additional aberrations than the ones presented at 550 nm. This stems from the fact that Zernike coefficients (in microns) were found to either be constant or have an infinitesimally small increase with wavelength [17, 70, 118, 165]. As a result of this finding, Zernike coefficients (in waves) decrease with increasing wavelength and thus the effect of diffraction and aberrations in larger pupils is better balanced for higher wavelengths. Furthermore, the optimal pupil size was found to shift towards larger values for a higher imaging wavelength. The optimal pupil size for best lateral resolution obtained from the EE metric, in adults 58-70, was found to be 3.13 mm $\pm$ 0.486 mm, providing a lateral resolution of 5.9μm $\pm$ 0.848 μm ($\lambda = 830$ nm). The lateral resolution determined by the average cutoff frequency at a 3.13 mm pupil was determined to be 6.9μm. A higher wavelength was found to provide better comfort during imaging and enables safer light exposure for the subject [112]. Thus, this finding adds to these advantages by maintaining the same image quality in higher

wavelengths in the presence of ocular aberrations at larger pupils.

5.3.2 Small entrance pupil SLO system

In traditional Maxwellian-view systems, a beam is focused onto the entrance pupil of the eye, creating a large uniformly illuminated spot on the retina [179, 180]. In the original SLO polarimeter setup, presented in Chapter 3, a narrow input beam was incident on the eye and focused onto the retina, creating a large diffraction blur on the retina. Unlike traditional fundus cameras or Maxwellian view systems, the original SLO polarimeter used a scanning system to raster scan the large diffraction blur onto a large FOV. Figure 5.2 illustrates the PSF of the input beam on the retina for a single scan position. It is evident that a single scan position illuminates several pixels. Thus, the optimized system design presented in this section is called a small entrance pupil cSLO polarimeter.

The small entrance pupil cSLO polarimeter setup can be mathematically described by using Equations 5.9 and 5.11, derived by Roorda [149]. If the first pass, illustrated in Figure 5.2, creates an approximately uniform illumination across the area of the PSF created on the second pass, then h_{in} can be replaced by a constant, C_2, and Equation 5.9 reduces to 5.20.

$$I_{\mathrm{SLO}_{\text{small entrance pupil}}}(x'', y'') = \left| C_2 \iint R(x', y') h_{out}(x'' + mx', y'' + my') D(x'', y'') dx' dy' \right|^2 \tag{5.20}$$

Then the image quality will only be determined by the image quality of the PSF formed in the second pass and by the confocal pinhole. By representing the complex reflectance function as a delta function and by removing the constant, image intensity for each scan position can be described by Equation 5.21

$$I_{\mathrm{SLO}_{\text{small entrance pupil}}}(x''_s, y''_s) = \left| [h_{out}(x''_s, y''_s) \circledast D(x''_s, y''_s)] \right|^2 \tag{5.21}$$

Equation 5.21 describes the intensity for a single scan position detected through a confocal pinhole at the detector plane. The image quality will only be determined by the image quality of the PSF formed in the second pass convolved with the confocal pinhole.

To demonstrate this result, we use actual entrance and exit pupil sizes. The two PSFs (ingoing small pupil and outgoing optimal pupil) were approximated by Gaussians of the same half width as the actual PSFs. For this simulation, a PSF of a single older subject with average HO RMS, as found in the older population, was used at 830 nms. Guassian approximated the PSFs well except for the area shown by a dotted curve in Figure 5.3(b).

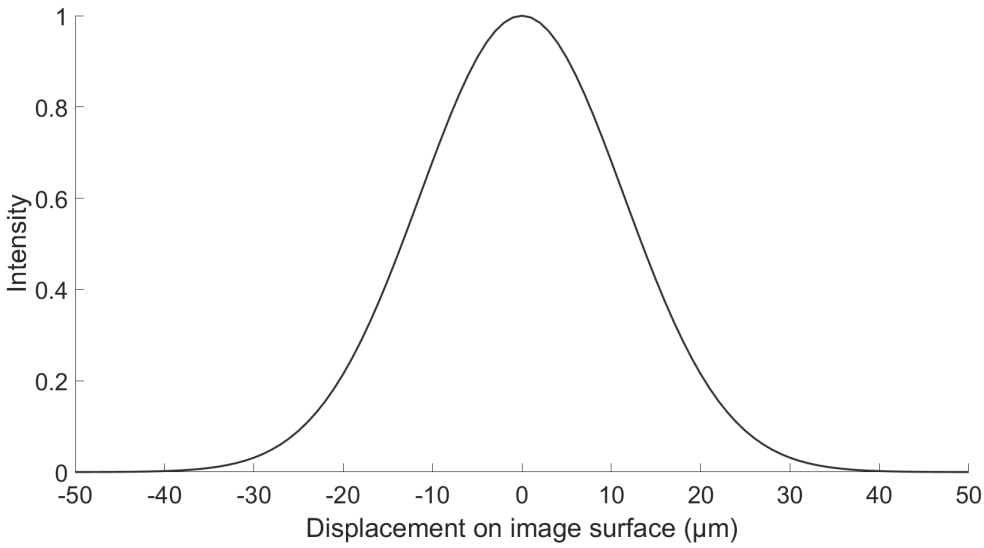

Figure 5.2: PSF on the retina from the first-pass in a small entrance pupil cSLO. Generated in Matlab.

To determine the effects of the two PSF's without the effect of the pinhole, an infinitely small detector was assumed. In this case the resulting PSF is the product of the two PSFs, as describe in Equation 5.17, derived by Roorda [149]. The Gaussian resulting from the 0.6 mm entrance pupil beam (5.3(a)) is multiplied by the Gaussian resulting from a 3.0 mm exit pupil beam (5.3(b)) to give the PSF in 5.3(c)

Consistent with what one might expect when multiplying a significantly broader PSF with a more compact PSF, the broad PSF contributes little to the final response. Therefore, retinal image quality using a small entrance pupil in an SLO is primarily affected by the light leaving the eye in the second-pass through the optimal exit pupil. This is analogous to a fundus camera design in which the retina is uniformly illuminated and image quality depends only on the second pass of light through the exit pupil.

The detector size, which appears in a convolution between the output PSF and detector plays a role in image quality. If it is a confocal pinhole, similar in size to the outgoing PSF, it will "trim" the PSF as discussed in Sections 3.7.4 and 4.2.3. For an intermediate sized detector there would also be improvement in image contrast by removing wide-angle scatter, which could be modeled by a broader, lower intensity Guassian added to the initial Gaussian in Figure 5.3.

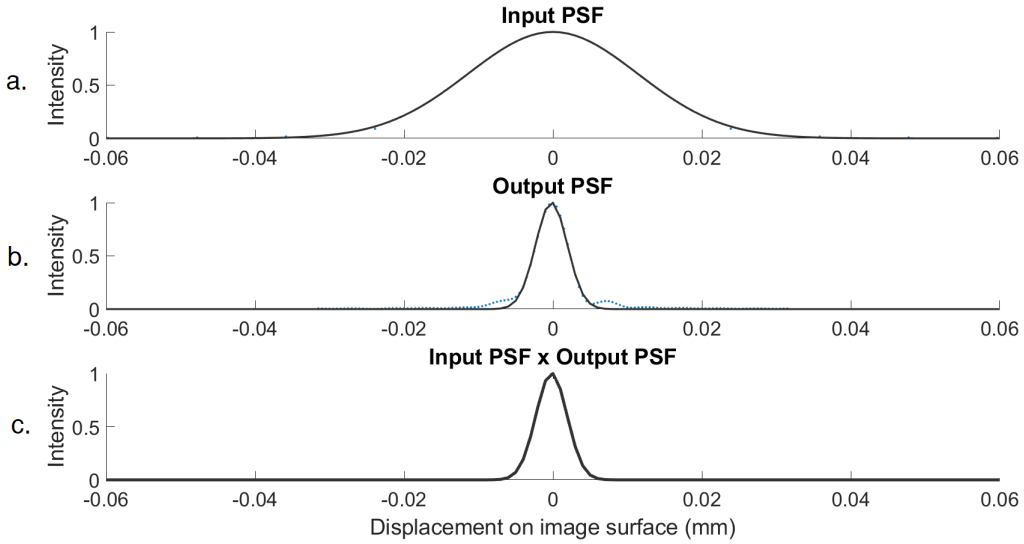

Figure 5.3: Intensity response for a single scan position. The input PSF of a small entrance beam (approximated by a Guassian) is multiplied by the output PSF of an optimally sized beam, also approximated by a Gaussian. The dotted curves represent the region of the outgoing PSF, not well modelled by the Gaussian. The product of the two PSF's approximates the double pass PSF as it leaves the eye, which is very similar to the single pass PSF through the optimal pupil. This is because the ingoing PSF has almost constant intensity over its central region. The dotted regions would be attenuated slightly more than the central region. The simulated PSFs presented were generated in Matlab.

Optimized design of the MM confocal scanning polarimeter using a small entrance pupil SLO setup

The optimized MM confocal scanning polarimeter using a small entrance pupil SLO setup is realized by introducing modifications in the return path, from the retina to the detector, of the original SLO polarimeter, presented in Chapter 3. Parts of the instrument will remain intact. The modified optical setup is illustrated in Figure 5.4. An 830 nm fiber, the input illumination source, and a two step collimator are still used to collimate the input beam. In the two step collimation, lens 2 (L2) is optically conjugate to the entrance pupil. The polarization state generator (PSG) is placed in collimated space before the beamsplitter (BS). The illumination and detection beam paths are separated by the BS. The collimated beam is then directed towards the scanning unit. The scanning unit consists of two galvanometric mirrors with a fast speed of 850 Hz and a max scan angle

of 12.5 degrees. Then, the entrance beam is reflected off the hot mirror and directed to the tube lens system. The unchanged tube lens consists of two custom-built lenses that de-magnify the scanning beam by 2.6 times. The small collimated input beam incident on the pupil (0.6 mm) creates a large diffraction blur on the retina as illustrated in figure 5.2. Reflected light from the retina is directed and descanned through the tube lens system. The return beam is refracted through the BS and is incident on the polarization state analyser (PSA). The exit pupil is defined by the clear aperture of the collection lens. By using a variable aperture in front of the collection lens, the exit pupil can be varied. A variable aperture could be placed prior to the PSA as well. Finally, the collection lens

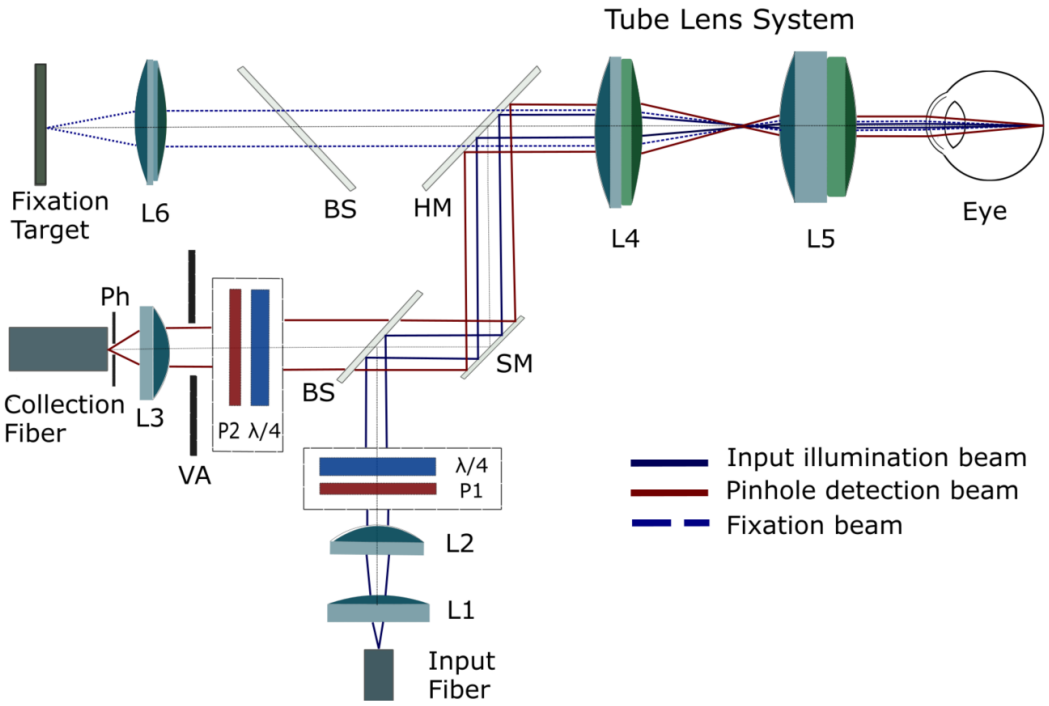

Figure 5.4: Schematic of the optimized MM confocal scanning polarimeter using a small entrance pupil cSLO setup. Input illumination beam path (dark blue), pinhole detection beam path (red), and fixation target beam path (light blue) are illustrated for the central scan position at zero scan angle. Optical components: L-Lens; BS-Beam splitter; HM-Hot mirror; SM-scanning mirror; Ph-Pinhole; P-Polarizer; $\lambda/4$-Quarter waveplate unit; VA-Variable aperture

focuses the reflected beam to the confocal pinhole. The variable aperture is used to change

the confocal pinhole size depending on the selection of exit pupil and collection lens.

Optimal entrance pupil and pinhole size for best lateral resolution were determined in Chapter 4 and further characterized in this chapter. It was determined that a 3.13 mm entrance pupil gave the best lateral resolution in older adults for an 830 nm imaging wavelength. When projecting the 3.13 mm exit pupil to a conjugate plane before the collection lens the pupil becomes 8.14 mm due to the magnification of the tube lens system, $M_{tube} = 2.6$. Therefore, the main proposed modifications of the SLO polarimeter included changing the L7 lens and placing two aperture stops, one for the confocal pinhole conjugate to the retina and one for regulating the exit pupil conjugate to the eye pupil. Modifications were implemented in CodeV and the optical design is presented in figure B.1 in Appendix B. The collection lens, L7, was selected to be a plano-convex lens (Edmund Optics 45487) with a large enough diameter to avoid light being attenuated. The aperture right in front of L7 was set to 8.14 mm. Using the pinhole analysis in Chapter 4 a TDL of 2.0 was selected. Thus, the pinhole size is calculated by the product of TDL, magnification and Airy disk diameter on the retina (Pinhole size = TDL $\times$ Magnification $\times$ Airy disc diameter). The pinhole size for a TDL of 2.0 was determined to be 101.1 μm, replacing the original pinhole of 250 μm.

5.3.3 Conventional large exit pupil SLO system

Image quality in cSLOs is determined by both the first and second-pass PSFs as demonstrated in equation 5.17 by the convolution of first and second pass PSFs [149]. While using the same optimal entrance and exit pupil size would result in an optimal image quality in the absence of aberrations, this setup significantly reduces the amount of light reaching the detector and degrades image quality in the presence of aberrations. Therefore, it is common to use a larger exit pupil to obtain as much light as possible and an optimally sized entrance pupil [107]. The cSLO polarimeter setup presented in this section uses an optimally sized entrance pupil and the full exit pupil for the return beam. In addition, common to other cSLO setups, the confocal pinhole only accepts light that originates from a small part of the retina, which overlaps with the illumination spot, reducing the amount of scattered light [107, 178].

Image quality dependence in the SLO system with an optimal input pupil and a large exit pupil was quantified using the assumption that the PSF on the retina, caused by a large exit pupil, was nearly uniform due to the presence of high aberrations. When replacing $h_{out}(x'_s, y'_s)$ with a constant, the convolution with the detector (D(x",y")) also became a constant, removing the effect of the detector, which is demonstrated in Equation

5.22. This equation is equivalent to the non-confocal SLO.

$$I_{\mathrm{SLO}_{\text{large exit pupil}}}(x''_s, y''_s) = \left|[h_{in}(x'_s, y'_s)] \circledast R(x'_s, y'_s)\right|^2 \tag{5.22}$$

However, experimental work like that of Izatt and Webb has demonstrated that the confocal pinhole or detector size does play an important role in the case where a smaller input pupil is used and collection through the whole pupil is conducted [107, 178]. An alternative way to mathematically investigate this relationship was undertaken by taking the convolution of an almost uniform second-pass PSF with the detector at different sizes, using Matlab. A Gaussian function was used to model the second-pass PSF and a rectangular function was used to model the detector. Both functions were normalized and convolved as illustrated in figure 5.5. This simulation indicated that even in the case when the second-pass PSF is taken to be nearly a constant, the detector size does affect the convolution. In addition, I then multiplied the convolution function with a Gaussian, which modeled the first-pass PSF, and squared the expression, obtaining a simulated double-pass image of a point source. As figure 5.6 suggests, the confocal pinhole plays a non-negligible role in the double-pass PSF.

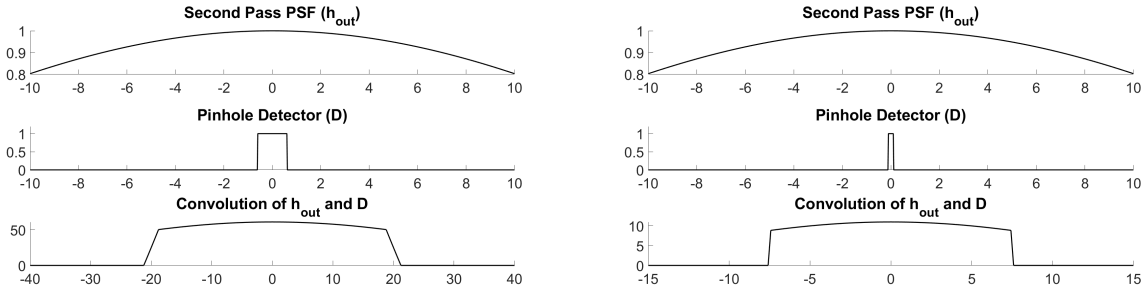

Figure 5.5: Improved net image quality with the smaller pinhole detector. Simulation of the second-pass by convolving the second-pass PSF and a narrower detector. The second-pass PSF due to a large exit pupil is simulated with a broad Gaussian function. The pinhole detector is simulated as a rectangular function. Both the Gaussian and rectangular functions were normalized. [Left] Simulation of the second-pass using a larger detector [Right] Simulation of the second-pass using a smaller detector. The smaller pinhole detector gives improved image quality.

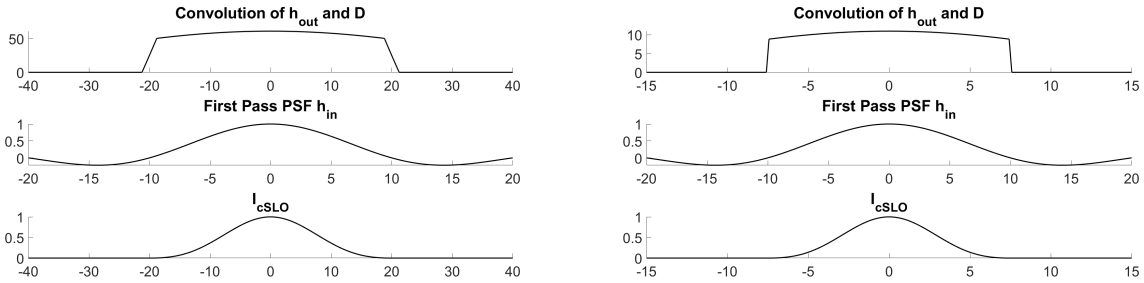

Figure 5.6: Simulation of the double-pass PSF as described in Equation 5.17. Convolution of the second-pass PSF and the pinhole detector, for two detector sizes presented in Figure 5.5, is used in this simulation. The first-pass PSF was modeled as a Gaussian for an optimal pupil size. [Left] Simulation of the double-pass PSF with a larger detector [Right] Simulation of the double-pass PSF with a smaller detector. The simulated results presented were generated in Matlab.

The image intensity of the SLO setup was represented by Equation 5.23 for each position of the illumination on the retinal space (x'_s, y'_s). Using the results of the simulation, the second-pass PSF was expressed as $h_{out} = C_3(D(x''_s, y''_s))$ and the double-pass PSF was expressed as:

$$I_{\text{SLO}_{\text{large exit pupil}}}(x''_s, y''_s) = \left|[h_{in}(x''_s, y''_s) \circledast R(x''_s, y''_s))] \cdot C_3(D(x''_s, y''_s))\right|^2 \tag{5.23}$$

Using the assumption that the feature of interest on the retina is an isolated point scatter at (0,0) then the complex reflectance function, $R(x'_s, y'_s)$, can be represented as a delta function resulting in Equation 5.24.

$$I_{\text{SLO}_{\text{large exit pupil}}}(x''_s, y''_s) = \left|h_{in}(x''_s, y''_s) \cdot C_3(D(x''_s, y''_s))\right|^2 \tag{5.24}$$

In conclusion, Figure 5.6 suggests that the confocal pinhole size plays a central role in the intensity of the image, further confirming Equation 5.24. This result is consistent with experimental work using this setup [107, 178]. Webb's and Izatt's cSLO setup, with a large exit pupil and smaller entrance pupil, experimentally indicated that optical resolution was determined by the focus of the incident beam on the retina and improved contrast was accomplished using a confocal aperture [107, 178]. While in both studies this result was indicated by experimental results, it was not mathematically proven. In this section, I demonstrated that the SLO behaves like a single-pass system when an optimally sized entrance pupil is used in the first-pass and a large pupil is used in the second-pass. In

addition, an optimally sized pinhole provided further improvement by trimming the PSF and improving contrast. Previously Webb and Roorda had shown an improvement in contrast for a system that used a mid-sized pupil on the first pass and a full pupil on the second pass. Here, I have shown that a large exit pupil does not degrade image quality and an optimal entrance pupil producing the best image quality on the retina can further improve the quality of the fundus image taken. Then, a confocal pinhole can be used in the place of the large detector, causing an additional effect for further improving resolution.

Optimized design of the MM confocal scanning polarimeter using an SLO setup with a large exit pupil

The optimized MM confocal scanning polarimeter using a cSLO setup with an optimal entrance pupil and large exit pupil is realized by introducing modifications in the incoming beam path, from the illumination source to the retina, of the original SLO polarimeter, presented in Chapter 3. The optical setup is illustrated in figure 5.7. An 830 nm fiber was used as an input illumination source. A two step collimator was used to collimate the input beam. Following the collimation, a beam expander is used to magnify the beam. Lens 4 (L4) is optically conjugate to the entrance pupil. Since the entrance beam diameter in the original SLO polarimeter was 0.6, the beam expander must introduce magnification of M=5.22 to enable an entrance pupil size of 3.13 mm. The entrance pupil is defined by the clear aperture of the second collimating lens L2. By using a variable aperture in front of L2, the entrance pupil can be varied. The variable aperture can also be placed after L4, which is another pupil conjugate. The polarization state generator (PSG) is placed in collimated space before the beamsplitter (BS). The PSG could also be placed before the beam expander. The illumination and detection beam paths were separated by the BS. The collimated and magnified beam is then directed towards the scanning unit. Then, the entrance beam is reflected off the hot mirror set at 45 degrees and directed to the tube lens system. The tube lens consists of two custom built lenses that de-magnify the scanning beam by 2.6 times. The collimated beam was then incident on the eye pupil, creating a compact diffraction blur on the retina. Reflected light from the retina was directed and descanned through the tube lens system. The return beam is refracted on the BS and is incident on the polarization state analyser (PSA). The exit pupil is defined by the clear aperture of the collection lens. Since the exit beam in this optical setup is taken to be the whole eye pupil, the clear aperture of L7 is chosen to be large enough to not attenuate any light. Finally, the collection lens focuses the reflected beam to the confocal pinhole. The variable aperture is used to change the confocal pinhole size depending on the selection of exit pupil and collection lens.

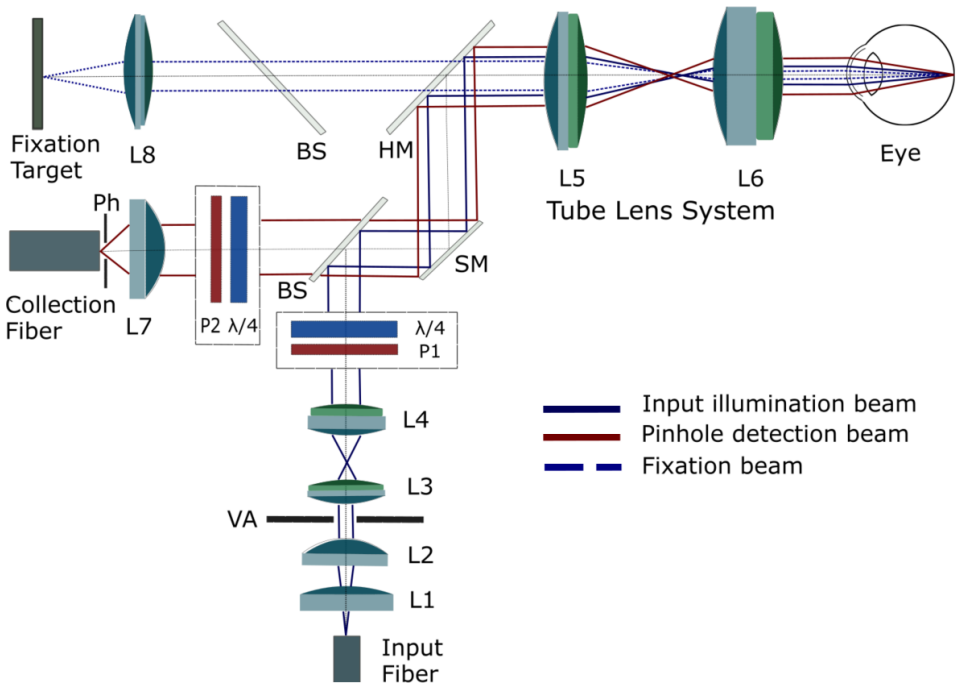

Figure 5.7: Schematic of the optimized MM confocal scanning polarimeter using a cSLO setup. Input illumination beam path (dark blue), pinhole detection beam path (red), and fixation target beam path (light blue) are illustrated for the central scan position at zero scan angle. Optical components: L-Lens; BS-Beam splitter; HM-Hot mirror; SM-scanning mirror; Ph-Pinhole; P-Polarizer; $\lambda/4$-Quarter waveplate unit; VA-Variable aperture

Optimal entrance pupil and pinhole size for best lateral resolution were determined in Chapter 4 and further characterized in this chapter. It was determined that a 3.13 mm entrance pupil gave the best lateral resolution in older adults for an 830 nm imaging wavelength. When projecting the 3.13 mm entrance pupil to the conjugate plane of L4, the aperture becomes 8.14 mm. Due to the addition of a reverse telescope, the beam is further demagnified, and so the variable aperture is set to 1.55 mm, enabling the entrance beam to be 3.13 mm on the pupil plane. Using the pinhole analysis in Chapter 4 a TDL of 2 was selected. The diffraction limited Airy disk diameter of a 3.13 mm entrance pupil is $5.4\mu m$ on the retina. Therefore, the pinhole size is calculated by the product of magnification between the retina and pinhole with the Airy disk on the retina (Pinhole size = TDL $\times$ Magnification $\times$ Airy disc diameter). The pinhole size was determined to be 101.1 μm for

this optical setup. Therefore, the main modifications of the cSLO polarimeter included adding a reverse telescope using L3 and L4 and placing two aperture stops, one for the confocal pinhole conjugate to the retina and one for regulating the entrance pupil conjugate to the eye pupil. The L7 lens was also replaced with a larger one to capture all the light exiting the eye pupil. Modifications were implemented in Code V and the optical design is presented in figure B.1 in Appendix B.

5.3.4 Impact of modification on image quality

Image quality was assessed in CodeV and the modulation transfer function (MTF) on the retina was generated for a diffraction limited eye in Figure 5.8. The MTF corresponds to both the cSLO with a small entrance pupil with optimal exit pupil and the cSLO with an optimal entrance pupil and a large exit pupil which demonstrate an improved image quality from the original donated instrument MTF presented in Figure 5.9.

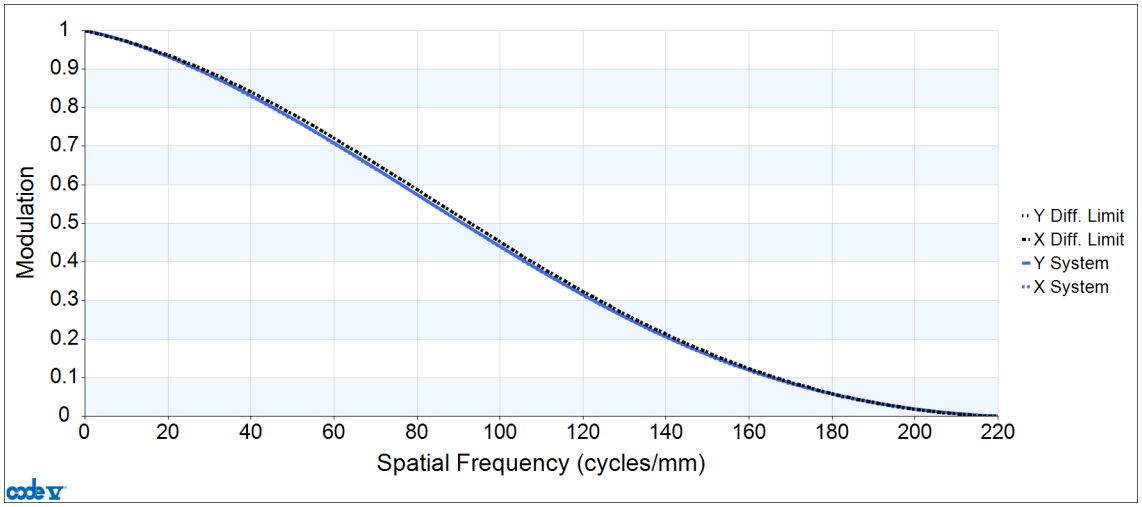

Figure 5.8: Modulation transfer function on the retina determined by the modified MM polarimeter SLO using either a small entrance pupil with optimal exit pupil or an optimal entrance pupil and a large exit pupil design with optimal confocal pinholes.

The improved image quality by using an optimal pupil size is also presented in Figure 5.9. The MTFs in Figure 5.9 correspond to a single 61 year old subject with average monochromatic aberrations among the older subject group. The cutoff frequency of the modified instrument MTF was determined to be 220 cycles/mm, which is significantly

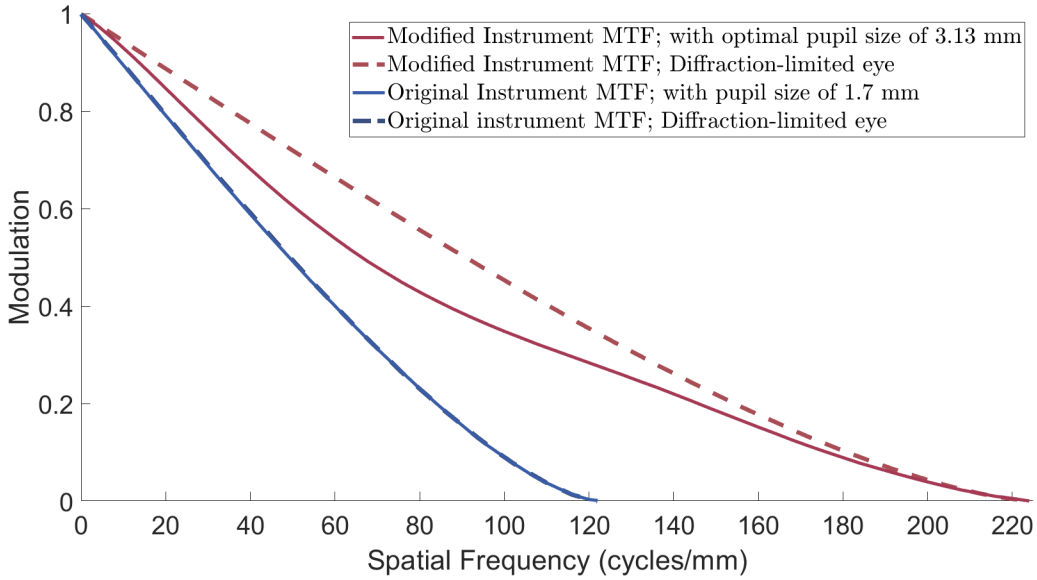

Figure 5.9: Modulation transfer function on the retina for the original (blue) and modified (red) setup for a single older subject with average monochromatic aberration.

improved from the original setup. The area under the MTF of the modified design is substantially larger than the original design even in the presence of ocular aberrations, further indicating the improved image quality. An improvement in modulation at the current pixel resolution limit at 60 cycles/mm is also evident.

5.4 Discussion

In this chapter, I showed that retinal image quality using a small entrance pupil in a cSLO setup, is dominated by the quality of the beam of light leaving the eye in the second-pass. In addition, the large exit pupil cSLO polarimeter setup using an optimally sized entrance pupil was confirmed to be a single-pass system, influenced by the optical quality of the ingoing beam. I have shown that the source of this effect can be either a large detector or the large amount of blur from the single-pass through a large pupil. In the latter case, I have further shown by derivation and modeling that the use of a confocal pinhole will further improve the image quality as previously demonstrated by Izatt [107]. Further, for both design the scanning beam and confocal pinhole reduce the effects of scat-

tered light and improve image quality, including optical resolution and contrast. The MM confocal scanning polarimeter can use either design for optimized instrumentation to image amyloid-β deposits in the retina of older adults. Both optical setups would theoretically provide equivalent results with minimal modification in the beam path. Comparing the two optical designs, the small entrance pupil cSLO with optimal exit pupil requires the least modification from the original MM confocal scanning polarimeter presented in Chapter 3. Lastly, the analysis of an optimal pupil size to be used in these setups was extended from Chapter 4, and was identified for an 830 nm imaging wavelength. Lateral resolution for optimal and larger pupils was found to remain relatively constant for a higher wavelength ($\lambda = 830nm$) in comparison to 550 nm, providing additional advantages when using an 830 nm imaging wavelength.

Chapter 6

Conclusion and future work

This thesis has proposed and presented a Mueller-Matrix (MM) confocal scanning laser polarimeter that integrates polarization optics with a donated scanning laser opthalmoscope (SLO). The proposed design was then optimized to improve image quality when imaging amyloid-β deposits in older adults. This work contributes to Campbell Lab's development of a prototype instrument for AD diagnosis.

Chapter 3, introduced the donated SLO and defined the design specifications. Since the commercial market for ocular technologies is highly competitive, and modalities for imaging the retina are constantly improving [26, 38, 142, 144, 169], it was important to design a prototype that has attractive features such as the combination of a large field of view and high lateral resolution. As competing technologies of AD diagnosis have been developed, it was important to design a prototype instrument that overcomes some of their shortcomings [103, 155, 189]. MM polarization imaging of amyloid-β deposits as a diagnostic approach has the advantage of providing a label-free, non-invasive, and potentially highly accessible diagnostic tool [45, 46, 58, 97, 145]. Other design specifications included the implementation of a repeatable, accurate, and fast polarization modulation method. Thus, a comparative analysis was carried out to identify the optimal polarization modulation method among quarter waveplates (QWPLs), photoelastic and magnetoptic modulators. The optimal method was deemed to be the rotating QWPL. This polarization modulation unit was further modified to eliminate rotation related errors in the polarization state generator and analyzer, a significant source of error in MM polarimetry [80, 108, 110, 168]. In addition, image quality analysis was conducted in Code V using a diffraction-limited eye to evaluate instrument performance. The optical resolution, pinhole size, pixel resolution, and fixation target were identified as the most important modifications needed to satisfy the specified design requirements.

Image quality in the MM scanning laser polarimeter is limited by the ocular optics. Retinal image quality was found to reduce with age due to the increase of monochromatic ocular wavefront aberrations in older adults [40, 73, 121, 150]. Although this finding has been documented by other research groups, it was confirmed in the results presented in Chapter 4. In addition, the chapter determined optimized conditions as a function of age that provide improved image quality in the MM scanning laser polarimeter, taking into account both diffraction through the eye pupil and aberrations in the ocular optics. Individual eye models using Zernike polynomial coefficients of 1219 subjects, 20-70 years old, were designed, and several image quality metrics as a function of pupil size were assessed, such as the 50 % encircled energy (EE) as a lateral resolution measure. The analysis in Chapter 4 confirmed that the relationship of pupil size and image quality reaches a turning point that provides the optimal pupil size for best image quality, consistent with literature [9, 43, 62, 146]. This turning point identifies the pupil size that provides the best balance between diffraction through the pupil and aberrations. Plots of image quality metrics as a function of pupil size were stratified by subject age: 20-32, 33-45, 46-57 and 58-70. Further, it was determined that selecting the pupil size specific to an age group will significantly improve the optical quality of an image taken of the fundus through the optics of the eye. The results presented were documented based on a large data set (n = 1219), providing age dependence and obtained in a theoretical setting, making this study unique. These results have important implications for the design of the MM scanning laser polarimeter as it can be optimized to the target resolution and age group subject to AD. Plots presented in this thesis could assist with optimized instrumentation designs in order to improve the quality of retinal images.

The wavelength dependence of lateral resolution as a function of pupil size in older adults was investigated to identify possible changes for an 830 nm imaging wavelength. It was determined that lateral resolution at 830 nm in the absence of aberration increases with the ratio of the two wavelengths, 830/550 = 1.509. However, in the presence of high aberrations, higher wavelengths do not introduce additional aberrations from those present at an imaging wavelength of 550 nm. The optimal pupil size for older adults (n=43), determined by 50 % EE, was found to be 3.13 mm ± 0.486 mm, providing a lateral resolution of 5.9 μm ± 0.848 μm (λ = 830 nm). Thus, resolution is impacted much less than 50 %, which is the impact of wavelength on resolution in the diffraction limit. Considering that higher wavelengths have been found to provide better comfort during imaging and enable lower light exposure, this finding adds to these advantages by improving image quality in higher wavelengths in the presence of ocular aberrations.

Chapter 5, following the work of Artal and Roorda [12, 14, 149], described the setup of two modified MM confocal scanning laser polarimeters. First, the SLO system with a

small entrance pupil and an optimal exit pupil was shown to be a single-pass system that is primarily influenced by the aberrations seen by light leaving the eye. The conventional SLO, using an optimally sized entrance pupil and the entire exit pupil, was determined to have resultant image quality which depended only on the image quality of the incoming beam. Therefore, the suggested optimal pupil size for best image quality on the retina and best pinhole size for resolution and throughput were implemented in designs for these setups, making both designs optimized to image amyloid-β deposits in the retinas of older adults, with higher optical resolution and greater image contrast.

Future work

The next major steps needed to extend the research presented in this thesis would be to experimentally implement and test the polarization optics in the donated instrument. To do so, the linear holder will have to be custom-made, and the QWPLs will need to be placed in their assigned orientations. Further, the modifications presented in Chapter 5 should also be implemented to optimize the optical setup for imaging amyloid-β deposits in older adults. The current pixel resolution should be improved by increasing the optical magnification of the instrument or increasing the number of pixels sampled. Additional information can be obtained by carrying out the following projects:

1. Testing the performance of the proposed MM polarimeter in older adults by directly assessing the quality of the images acquired. For a group of older subjects, the quality of images taken with the original instrument would be compared to the quality of the images taken with the each of the novel designs implemented. Image quality can be characterized by optical quality metrics used on the image described in [54, 91, 107]. Acutance was presented by Choong et al. in [54] and was implemented by Hunter et al. in [91] as an objective method to quantify the clarity of the nerve fiber layer [54, 91]. The SNR and Shannon entropy are additional image quality metrics that can be used in this study [91]. In addition, image sharpness can be quantitatively measured as done by LaRocca et al. in [107]. The experimental results can then be compared with the improvements predicted in this thesis, and quantitative differences can be identified.

2. Identification of optimal fixation target for older adults: The eye is never still, even during fixation and so ocular fixation eye movements possess a serious issue in SLO systems [120]. Thus, the fixation target is another important design parameter that needs to be optimized. There is evidence that shape, color, or eccentricity may influence the amplitude and direction of fixation eye movements [162]. Furthermore, it

was suggested that a fixation target that looks like a combination of a bull's eye and cross hairs resulted in a lower microsaccade rate [162]. In addition, previous research papers document that the fixation stability does not change with age and that older observers focused on a fixation target have fixation eye movements similar to those of younger observers [172]. However, since the investigation of the optimal fixation target is limited to a handful of published works, it would be useful to conduct a study using a set of shapes to identify the optimal fixation target shape for older subjects with or without AD. The fixation stability in older adults can also be determined from this study [172].

3. Implementing optimal conditions for other age groups to test proposed designs for improved performance in these populations: The optical quality is also degraded in other populations with abnormal optics due to diseases like diabetes [41]. Thus, the proposed designs can be tested for improved performance in these populations.

Letter of copyright permissions

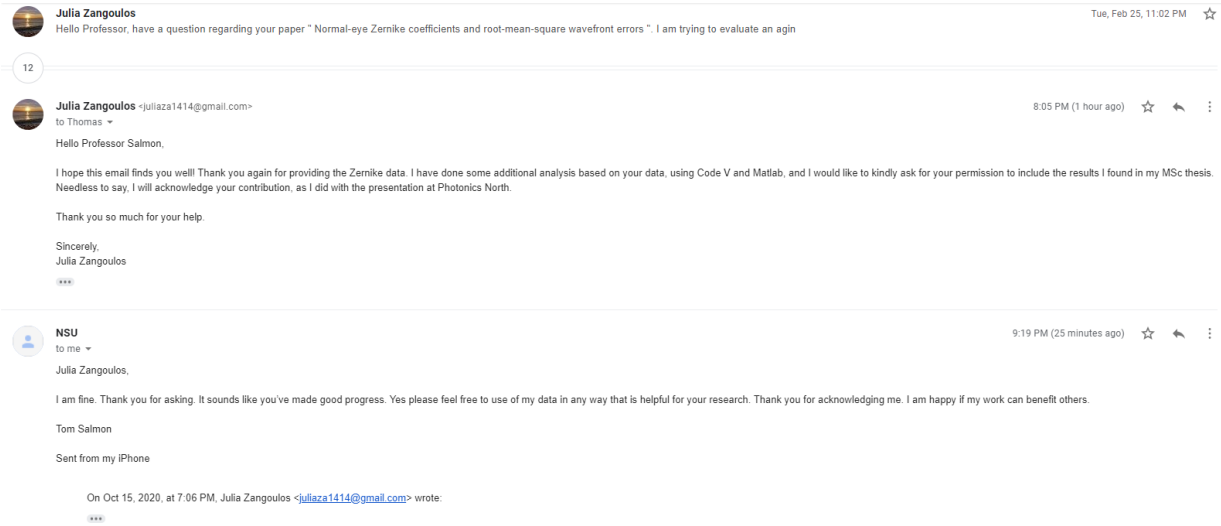

Julia Zangoulos Tue, Feb 25, 11:02 PM

Hello Professor, have a question regarding your paper " Normal-eye Zernike coefficients and root-mean-square wavefront errors ". I am trying to evaluate an agin

12

Julia Zangoulos <juliaza1414@gmail.com> 8:05 PM (1 hour ago)

to Thomas

Hello Professor Salmon,

I hope this email finds you well! Thank you again for providing the Zernike data. I have done some additional analysis based on your data, using Code V and Matlab, and I would like to kindly ask for your permission to include the results I found in my MSc thesis. Needless to say, I will acknowledge your contribution, as I did with the presentation at Photonics North.

Thank you so much for your help.

Sincerely,
Julia Zangoulos

NSU 9:19 PM (25 minutes ago)

to me

Julia Zangoulos,

I am fine. Thank you for asking. It sounds like you've made good progress. Yes please feel free to use of my data in any way that is helpful for your research. Thank you for acknowledging me. I am happy if my work can benefit others.

Tom Salmon

Sent from my iPhone

On Oct 15, 2020, at 7:06 PM, Julia Zangoulos <juliaza1414@gmail.com> wrote:

Figure 6.1: Permission from Dr. Salmon to used the Zernike polynomial coefficients, which were provided by his lab, for the human eye models presented in Chapter 4

Taylor & Francis Group LLC - Books - License Terms and Conditions

This is a License Agreement between Julia Zangoulos ("You") and Taylor & Francis Group LLC - Books ("Publisher") provided by Copyright Clearance Center ("CCC"). The license consists of your order details, the terms and conditions provided by Taylor & Francis Group LLC - Books, and the CCC terms and conditions.

All payments must be made in full to CCC.

Order Date	15-Jan-2021	Type of Use	Republish in a thesis/dissertation
Order license ID	1090711-1	Publisher	CRC Press
ISBN-13	978-1-4822-5155-5	Portion	Image/photo/illustration

LICENSED CONTENT

Publication Title	Polarized Light and the Mueller Matrix Approach	Country	United States of America
		Rightsholder	Taylor & Francis Group LLC - Books
Author/Editor	Ossikovski, Razvigor, Perez, Jose	Publication Type	Book
Date	05/18/2016	URL	http://www.crcnetbase.com/doi/book/10....
Language	English		

REQUEST DETAILS

Portion Type	Image/photo/illustration	Distribution	Worldwide
Number of images / photos / illustrations	2	Translation	Original language of publication
Format (select all that apply)	Electronic	Copies for the disabled?	No
Who will republish the content?	Academic institution	Minor editing privileges?	No
Duration of Use	Life of current edition	Incidental promotional use?	No
Lifetime Unit Quantity	Up to 499	Currency	CAD
Rights Requested	Main product		

NEW WORK DETAILS

Title	Mueller Matrix Confocal Scanning Laser Polarimetry and Optimal Conditions for Improved Image Quality	Institution name	University of Waterloo
		Expected presentation date	2021-01-21
Instructor name	Melanie Campbell		

ADDITIONAL DETAILS

Order reference number	N/A	The requesting person / organization to appear on the license	Julia Zangoulos

REUSE CONTENT DETAILS

Title, description or numeric reference of the portion(s)	The polarization ellipse; Poincare Sphere	Title of the article/chapter the portion is from	Polarized electromagnetic waves
Editor of portion(s)	N/A	Author of portion(s)	Ossikovski, Razvigor; Perez, Jose
Volume of serial or monograph	N/A	Issue, if republishing an article from a serial	N/A
Page or page range of portion	5,30	Publication date of portion	2016-05-18

Figure 6.2: Permission to reprint Figures 2.1 p.6, and 2.2 p.10.

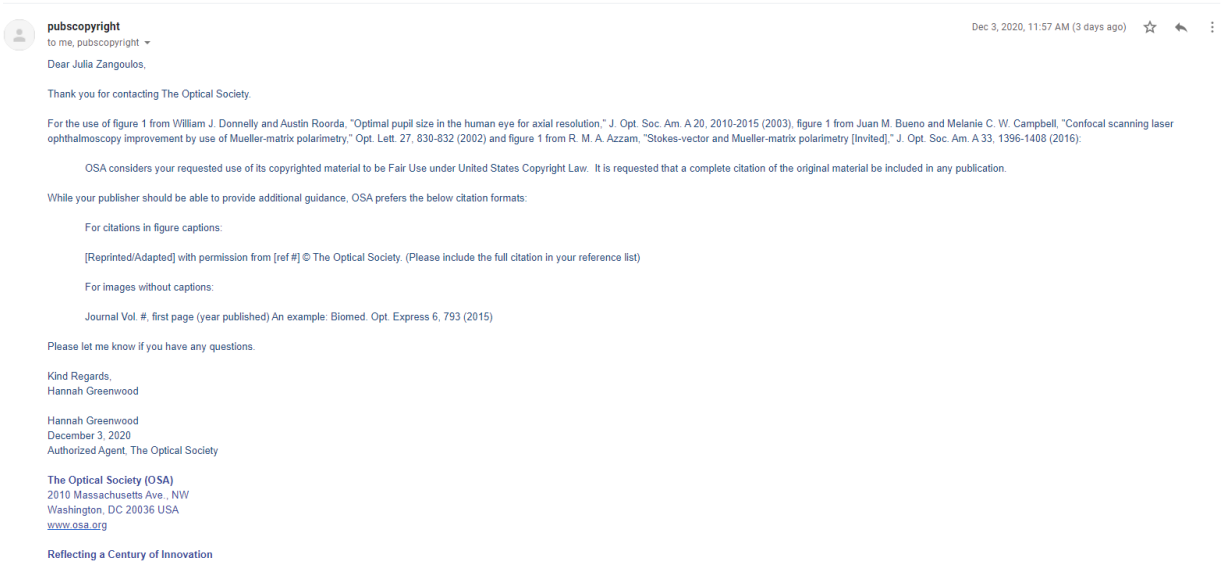

pubscopyright
to me, pubscopyright

Dec 3, 2020, 11:57 AM (3 days ago)

Dear Julia Zangoulos,

Thank you for contacting The Optical Society.

For the use of figure 1 from William J. Donnelly and Austin Roorda, "Optimal pupil size in the human eye for axial resolution," J. Opt. Soc. Am. A 20, 2010-2015 (2003), figure 1 from Juan M. Bueno and Melanie C. W. Campbell, "Confocal scanning laser ophthalmoscopy improvement by use of Mueller-matrix polarimetry," Opt. Lett. 27, 830-832 (2002) and figure 1 from R. M. A. Azzam, "Stokes-vector and Mueller-matrix polarimetry [Invited]," J. Opt. Soc. Am. A 33, 1396-1408 (2016):

OSA considers your requested use of its copyrighted material to be Fair Use under United States Copyright Law. It is requested that a complete citation of the original material be included in any publication.

While your publisher should be able to provide additional guidance, OSA prefers the below citation formats:

For citations in figure captions:

[Reprinted/Adapted] with permission from [ref #] © The Optical Society. (Please include the full citation in your reference list)

For images without captions:

Journal Vol. #, first page (year published) An example: Biomed. Opt. Express 6, 793 (2015)

Please let me know if you have any questions.

Kind Regards,
Hannah Greenwood

Hannah Greenwood
December 3, 2020
Authorized Agent, The Optical Society

The Optical Society (OSA)
2010 Massachusetts Ave., NW
Washington, DC 20036 USA
www.osa.org

Reflecting a Century of Innovation

Figure 6.3: Permission to reprint/adapt Figures 3.4 p.25, 3.5 p.26, 3.7 p.29, 3.9 p.32, and 4.3 p.63.

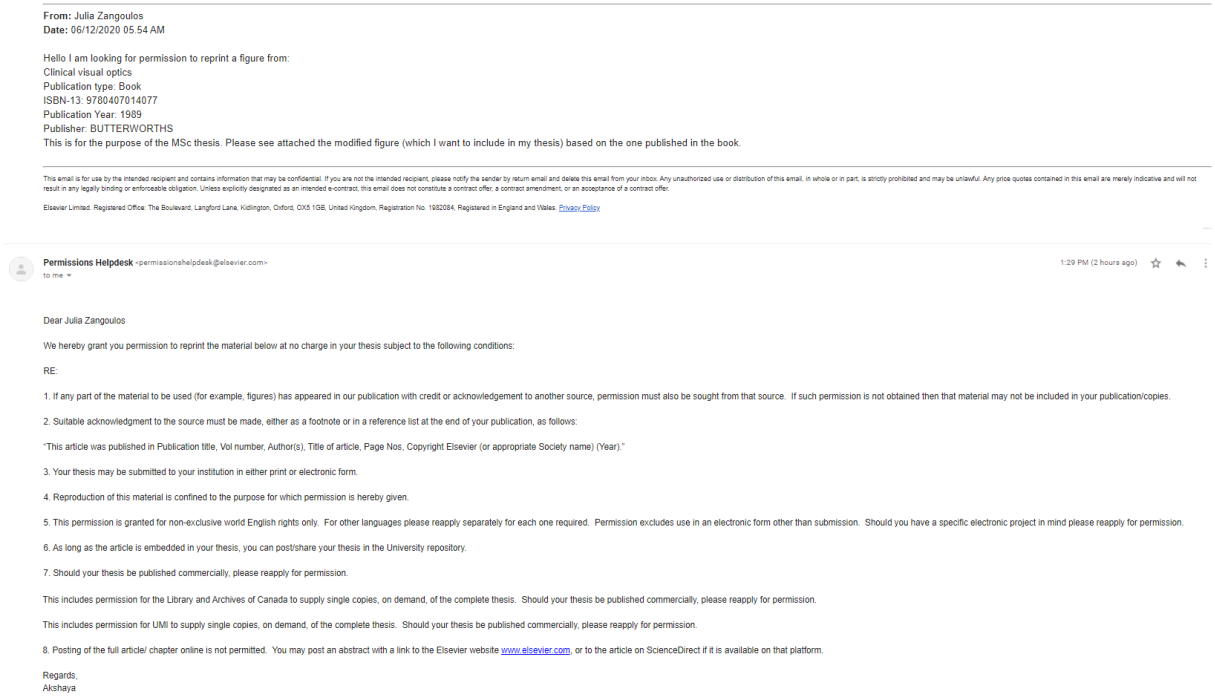

From: Julia Zangoulos
Date: 06/12/2020 05.54 AM

Hello I am looking for permission to reprint a figure from:
Clinical visual optics
Publication type: Book
ISBN-13: 9780407014077
Publication Year: 1989
Publisher: BUTTERWORTHS
This is for the purpose of the MSc thesis. Please see attached the modified figure (which I want to include in my thesis) based on the one published in the book.

Permissions Helpdesk <permissionshelpdesk@elsevier.com>
to me

1:29 PM (2 hours ago)

Dear Julia Zangoulos

We hereby grant you permission to reprint the material below at no charge in your thesis subject to the following conditions:

RE:

1. If any part of the material to be used (for example, figures) has appeared in our publication with credit or acknowledgement to another source, permission must also be sought from that source. If such permission is not obtained then that material may not be included in your publication/copies.

2. Suitable acknowledgment to the source must be made, either as a footnote or in a reference list at the end of your publication, as follows:

"This article was published in Publication title, Vol number, Author(s), Title of article, Page Nos, Copyright Elsevier (or appropriate Society name) (Year)."

3. Your thesis may be submitted to your institution in either print or electronic form.

4. Reproduction of this material is confined to the purpose for which permission is hereby given.

5. This permission is granted for non-exclusive world English rights only. For other languages please reapply separately for each one required. Permission excludes use in an electronic form other than submission. Should you have a specific electronic project in mind please reapply for permission.

6. As long as the article is embedded in your thesis, you can post/share your thesis in the University repository.

7. Should your thesis be published commercially, please reapply for permission.

This includes permission for the Library and Archives of Canada to supply single copies, on demand, of the complete thesis. Should your thesis be published commercially, please reapply for permission.

This includes permission for UMI to supply single copies, on demand, of the complete thesis. Should your thesis be published commercially, please reapply for permission.

8. Posting of the full article/ chapter online is not permitted. You may post an abstract with a link to the Elsevier website www.elsevier.com, or to the article on ScienceDirect if it is available on that platform.

Regards,
Akshaya

Figure 6.4: Permission to reprint/adapt Figure 4.1 p.50.

References

[1] Agustina Alaimo, Guadalupe García Liñares, Juan Marco Bujjamer, Roxana Mayra Gorojod, Soledad Porte Alcon, Jimena Hebe Martínez, Alicia Baldessari, Hernán Edgardo Grecco, and Mónica Lidia Kotler. Toxicity of blue led light and A2E is associated to mitochondrial dynamics impairment in ARPE-19 cells: implications for age-related macular degeneration. *Archives of Toxicology*, 93(5):1401–1415, may 2019.

[2] Sanaz Alali and Alex Vitkin. Polarized light imaging in biomedicine: emerging Mueller matrix methodologies for bulk tissue assessment. *Journal of Biomedical Optics*, 20(6):061104, mar 2015.

[3] Alzheimer Society of Canada. Dementia numbers in Canada , 2019.

[4] Shiro Amano, Yuki Amano, Satoru Yamagami, Takashi Miyai, Kazunori Miyata, Tomokazu Samejima, and Tetsuro Oshika. Age-related changes in corneal and ocular higher-order wavefront aberrations. *American Journal of Ophthalmology*, 137(6):988–992, jun 2004.

[5] Amrit Ambirajan. Optimum angles for a polarimeter: part I. *Optical Engineering*, 34(6):1651, jun 1995.

[6] Amrit Ambirajan. Optimum angles for a polarimeter: part II. *Optical Engineering*, 34(6):1656, jun 1995.

[7] Amrit Ambirajan and Dwight C. Look, Jr. Optimum angles for a Mueller matrix polarimeter. In Dennis H. Goldstein and David B. Chenault, editors, *Polarization Analysis and Measurement II*, volume 2265, page 314. International Society for Optics and Photonics, sep 1994.

[8] Anderson. United States Patent (19) 30 Foreign Application Priority Data. Technical report, nov 1994.

[9] Pablo Artal. Optics of the eye and its impact in vision: a tutorial. *Advances in Optics and Photonics*, 6(3):340, sep 2014.

[10] Pablo Artal. *Handbook of visual optics: Instrumentation and vision correction, volume II*. CRC Press, Taylor & Francis Group, 2017.

[11] Pablo Artal, Esther Berrio, Antonio Guirao, and Patricia Piers. Contribution of the cornea and internal surfaces to the change of ocular aberrations with age. *Journal of the Optical Society of America A*, 19(1):137, jan 2002.

[12] Pablo Artal, Daniel G. Green, Ignacio Iglesias, and Norberto López-Gil. Double-pass measurements of the retinal-image quality with unequal entrance and exit pupil sizes and the reversibility of the eye's optical system. *Journal of the Optical Society of America A*, 12(10):2358, oct 1995.

[13] Pablo Artal, Antonio Guirao, Esther Berrio, and David R. Williams. Compensation of corneal aberrations by the internal optics in the human eye. *Journal of Vision*, 1(1):1–8, may 2001.

[14] Pablo Artal, Susana Marcos, David R. Williams, and Rafael Navarro. Odd aberrations and double-pass measurements of retinal image quality. *Journal of the Optical Society of America A*, 12(2):195, feb 1995.

[15] Oriol Arteaga, Marta Baldrís, Joan Antó, Adolf Canillas, Esther Pascual, and Enric Bertran. Mueller matrix microscope with a dual continuous rotating compensator setup and digital demodulation. *Applied Optics*, 53(10):2236, apr 2014.

[16] David A. Atchison. Optics of the human eye. In *Encyclopedia of Modern Optics*, volume 1-5, chapter 5, pages 43–63. Elsevier, jan 2018.

[17] David A. Atchison and George Smith. Chromatic dispersions of the ocular media of human eyes. *Journal of the Optical Society of America A*, 22(1):29, jan 2005.

[18] David A Atchison and Larry N Thibos. Optical models of the human eye. *Clinical and Experimental Optometry*, 99(2):99–106, mar 2016.

[19] R. M. A. Azzam. Photopolarimetric measurement of the Mueller matrix by Fourier analysis of a single detected signal. *Optics Letters*, 2(6):148, jun 1978.

[20] R. M. A. Azzam. Stokes-vector and Mueller-matrix polarimetry [Invited]. *Journal of the Optical Society of America A*, 33(7):1396, jul 2016.

[21] R. M. A. Azzam, I. M. Elminyawi, and A. M. El-Saba. General analysis and optimization of the four-detector photopolarimeter. *Journal of the Optical Society of America A*, 5(5):681, may 1988.

[22] D. U. Bartsch, R. N. Weinreb, G. Zinser, and W. R. Freeman. Confocal scanning infrared laser ophthalmoscopy for indocyanine green angiography. *American Journal of Ophthalmology*, 120(5):642–651, nov 1995.

[23] Optical Society of America Bass, Michael. *Hanbook of Optics*. The McGraw-Hill Companies, Inc., 1939.

[24] Bernhard Baumann, Adelheid Wöhrer, Gerda Ricken, Michael Pircher, Gabor G. Kovacs, and Christoph K. Hitzenberger. Polarization properties of amyloid-beta plaques in Alzheimer's disease (Conference Presentation). In Steen J. Madsen and Victor X. D. Yang, editors, *Clinical and Translational Neurophotonics; Neural Imaging and Sensing; and Optogenetics and Optical Manipulation*, volume 9690, page 21. SPIE, apr 2016.

[25] E. Bernabeu and J. J. Gil. An experimental device for the dynamic determination of Mueller matrices. *Journal of Optics*, 16(3):139–141, may 1985.

[26] Josef F. Bille. *High Resolution Imaging in Microscopy and Ophthalmology*. Springer International Publishing, 2019.

[27] J. W. Blaker. Toward an adaptive model of the human eye. *Journal of the Optical Society of America*, 70(2):220–223, feb 1980.

[28] Max Born, Emil Wolf, A. B. Bhatia, P. C. Clemmow, D. Gabor, A. R. Stokes, A. M. Taylor, P. A. Wayman, and W. L. Wilcock. *Principles of Optics*. Cambridge University Press, oct 1999.

[29] Ron Brookmeyer, Elizabeth Johnson, Kathryn Ziegler-Graham, and H. Michael Arrighi. Forecasting the global burden of Alzheimer's disease. *Alzheimer's and Dementia*, 3(3):186–191, jul 2007.

[30] Juan M. Bueno. Measurement of parameters of polarization in the living human eye using imaging polarimetry. *Vision Research*, 40(28):3791–3799, 2000.

[31] Juan M. Bueno. Polarimetry using liquid-crystal variable retarders: Theory and calibration. *Journal of Optics A: Pure and Applied Optics*, 2(3):216–222, may 2000.

[32] Juan M. Bueno. The influence of depolarization and corneal birefringence on ocular polarization. *Journal of Optics A: Pure and Applied Optics*, 6(3):S91, mar 2004.

[33] Juan M. Bueno and Pablo Artal. Double-pass imaging polarimetry in the human eye. *Optics Letters*, 24(1):64, jan 1999.

[34] Juan M. Bueno and Melanie C. W. Campbell. Confocal scanning laser ophthalmoscopy improvement by use of Mueller-matrix polarimetry. *Optics Letters*, 27(10):830, may 2002.

[35] Juan M. Bueno and Melanie C. W. Campbell. Polarization properties of the in vitro old human crystalline lens. *Ophthalmic and Physiological Optics*, 23(2):109–118, mar 2003.

[36] Juan M. Bueno, Jennifer J. Hunter, Christopher J. Cookson, Marsha L. Kisilak, and Melanie C. W. Campbell. Improved scanning laser fundus imaging using polarimetry. *Journal of the Optical Society of America A*, 24(5):1337, may 2007.

[37] Juan M. Bueno and Jaroslaw Jaronski. Spatially resolved polarization properties for in vitro corneas. *Ophthalmic and Physiological Optics*, 21(5):384–392, sep 2001.

[38] Juan M. Bueno and Brian Vohnsen. Polarimetric high-resolution confocal scanning laser ophthalmoscope. *Vision Research*, 45(28):3526 3534, dec 2005.

[39] Stephen A Burns and Robert H Webb. Optical generation of the visual stimulus. Technical report, Handbook of optics. New York: McGraw Hill, 28(2), 1994.

[40] Richard I. Calver, Michael J. Cox, and David B. Elliott. Effect of aging on the monochromatic aberrations of the human eye. *Journal of the Optical Society of America A*, 16(9):2069, sep 1999.

[41] A. M. Calvo-Maroto, R. J. Perez-Cambrodí, C. Albarán-Diego, A. Pons, and A. Cerviño. Optical quality of the diabetic eye: A review, nov 2014.

[42] Charles E Campbell. Matrix method to find a new set of Zernike coefficients from an original set when the aperture radius is changed. *Journal of the Optical Society of America A*, 20(2):209, 2003.

[43] F. W. Campbell and R. W. Gubisch. Optical quality of the human eye. *The Journal of Physiology*, 186(3):558–578, oct 1966.

[44] Melanie C. W. Campbell, Juan M. Bueno, Christopher J. Cookson, Qingyuan Liang, Marsha L. Kisilak, and Jennifer J. Hunter. Enhanced confocal microscopy and ophthalmoscopy with polarization imaging. In Warren C. W. Chan, Kui Yu, Ulrich J. Krull, Richard I. Hornsey, Brian C. Wilson, and Robert A. Weersink, editors, *Photonic Applications in Biosensing and Imaging*, volume 5969, page 59692H. SPIE, sep 2005.

[45] Melanie C.W. Campbell, Wing Chung Theodore Chow, Laura Emptage, Christopher Cookson, Bill Milgram, and Howard Dobson. Polarization properties of amyloid beta deposits in retinas of an animal model of Alzheimer's disease. In *Frontiers in Optics, FiO 2014*, page FW5F.4. Optical Society of America (OSA), oct 2014.

[46] Melanie C.W. Campbell, David DeVries, Laura Emptage, Chris Cookson, Marsha Kisilak, Juan M. Bueno, and Francisco J. Avila. Polarization properties of amyloid beta in the retina of the eye as a biomarker of Alzheimer's disease. In *Bio-Optics: Design and Application, BODA 2015*, page BM3A.4. Optical Society of America (OSA), apr 2015.

[47] Ian Mackenzie Campbell, Melanie CW, Ji Ren, Erik Mason, Rachel Redekop, Laura Emptage, Veronica Hirsch-Reinshagen, Robin Hsiung. Distribution of retinal amyloid deposits in association with Alzheimer's disease. In *Investigative Ophthalmology & Visual Science, 60(9)*, pages 3541–3541, 2019.

[48] John F Casser, Linda.; Amos. Comprehensive adult eye and vision examination. *American Optometric Association*, 1994.

[49] Barry Cense, Teresa C. Chen, B. Hyle Park, Mark C. Pierce, and Johannes F. De Boer. Thickness and birefringence of healthy retinal nerve fiber layer tissue measured with polarization-sensitive optical coherence tomography. *Investigative Ophthalmology and Visual Science*, 45(8):2606–2612, aug 2004.

[50] W. N. Charman. *Visual optics and instrumentation*. Macmillan, 1991.

[51] Xiaojun Chen, Lianshan Yan, and X. S. Yao. Waveplate analyzer using binary magneto-optic rotators. *Optics Express*, 15(20):12989, oct 2007.

[52] Yi-Chun Chen, Chong-Jhih Jiang, Tsung-Hsun Yang, and Ching-Cherng Sun. Development of a human eye model incorporated with intraocular scattering for visual performance assessment. *Journal of Biomedical Optics*, 17(7):0750091, jul 2012.

[53] Han Cheng, Justin K. Barnett, Abhiram S. Vilupuru, Jason D. Marsack, Sanjeev Kasthurirangan, Raymond A. Applegate, and Austin Roorda. A population study on changes in wave aberrations with accomodation. *Journal of Vision*, 4(4):272–280, apr 2004.

[54] Y. F. Choong, F. Rakebrandt, R. V. North, and Jomes E. Morgan. Acutance, an objective measure of retinal nerve fibre image clarity. *British Journal of Ophthalmology*, 87(3):322–326, mar 2003.

[55] LW Chu. Alzheimer's disease: early diagnosis and treatment. *Hong Kong Med J*, 18(228-37), 2012.

[56] Eric Compain and Bernard Drevillon. High-frequency modulation of the four states of polarization of light with a single phase modulator. *Review of Scientific Instruments*, 69(4):1574–1580, apr 1998.

[57] Christine A. Curcio, Kenneth R. Sloan, Robert E. Kalina, and Anita E. Hendrickson. Human photoreceptor topography. *The Journal of Comparative Neurology*, 292(4):497–523, feb 1990.

[58] David DeVries, Melanie C W Campbell, Laura Emptage, Chris Cookson, Marsha Kisilak, Francisco J. Avila, Juan M Bueno, Rachel Redekop, and Matthew Wilson. Polarization properties of amyloid beta deposits in ex vivo human retinas from those with Alzheimer's disease differ from surrounding retina. In *ARVO Journals*, 2015.

[59] E. DeHoog and J. Schwiegerling. Optimal parameters for retinal illumination and imaging in fundus cameras. *Applied Optics*, 47(36):6769–6777, dec 2008.

[60] Walter T. Delpero, Barbara E. Robinson, Jane A. Gardiner, Louise Nasmith, Anne Rowan-Legg, and Benoît Tousignant. Evidence-based clinical practice guidelines for the periodic eye examination in children aged 0–5 years in Canada. *Canadian Journal of Ophthalmology*, 54(6):751–759, dec 2019.

[61] Dennis H. Goldstein. *Polarized Light*. CRC Press, third edit edition, 2017.

[62] William J. Donnelly and Austin Roorda. Optimal pupil size in the human eye for axial resolution. *Journal of the Optical Society of America A*, 20(11):2010, nov 2003.

[63] Andreas W. Dreher, Josef F. Bille, and Robert N. Weinreb. Active optical depth resolution improvement of the laser tomographic scanner. *Applied Optics*, 28(4):804, feb 1989.

[64] Andreas W. Dreher and Klaus Reiter. Scanning laser polarimetry of the retinal nerve fiber layer. *Polarization Analysis and Measurement*, 1746:34–41, dec 1992.

[65] Andreas W. Dreher, Klaus Reiter, and Robert N. Weinreb. Spatially resolved birefringence of the retinal nerve fiber layer assessed with a retinal laser ellipsometer. *Applied Optics*, 31(19):3730, jul 1992.

[66] Sami G. El Hage and Francoise Berny. Contribution of the crystalline lens to the spherical aberration of the eye. *J Opt Soc Am*, 63(2):205–211, feb 1973.

[67] Ann E. Elsner and Matthew S. Muller. Laser applications and system considerations in ocular imaging, 2008.

[68] Steven Esau and Melanie C.W. Campbell. Design for Faster Measurement of Mueller Matrices in Double Pass Retinal Imaging. In *2020 Photonics North, PN 2020*. Institute of Electrical and Electronics Engineers Inc., may 2020.

[69] R. Daniel Ferguson, Daniel X. Hammer, Ann E. Elsner, Robert H. Webb, Stephen A. Burns, and John J. Weiter. Wide-field retinal hemodynamic imaging with the tracking scanning laser ophthalmoscope. *Optics Express*, 12(21):5198, oct 2004.

[70] Enrique J. Fernández, Angelika Unterhuber, Pedro M. Prieto, Boris Hermann, Wolfgang Drexler, and Pablo Artal. Ocular aberrations as a function of wavelength in the near infrared measured with a femtosecond laser. *Optics Express*, 13(2):400, jan 2005.

[71] José Francisco Castejón-Mochón, Norberto López-Gil, Antonio Benito, and Pablo Artal. Ocular wave-front aberration statistics in a normal young population. *Vision Research*, 42(13):1611–1617, jun 2002.

[72] Thomas Friberg and Leanne Labriola. Wide-Field Imaging and Angiography. pages 27–40. Springer, Berlin, Heidelberg, 2010.

[73] Takashi Fujikado, Teruhito Kuroda, Sayuri Ninomiya, Naoyuki Maeda, Yasuo Tano, Tetsuro Oshika, Yoko Hirohara, and Toshifumi Mihashi. Age-related changes in ocular and corneal aberrations. *American Journal of Ophthalmology*, 138(1):143–146, jul 2004.

[74] José J. Gil Pérez and Razvigor Ossikovski. *Polarized Light and the Mueller Matrix Approach*. CRC Press, jul 2017.

[75] Adrian Glasser and Melanie C.W. Campbell. Presbyopia and the optical changes in the human crystalline lens with age. *Vision Research*, 38(2):209–229, jan 1998.

[76] Adrian Glasser and Melanie C.W. Campbell. Biometric, optical and physical changes in the isolated human crystalline lens with age in relation to presbyopia. *Vision Research*, 39(11):1991–2015, jun 1999.

[77] Dennis H Goldstein. *Polarized Light*. Marcel Dekker, Inc., NY, second edi edition, 2003.

[78] Hans E. Grossniklaus, John M. Nickerson, Henry F. Edelhauser, Louise A.M.K. Bergman, and Lennart Berglin. Anatomic alterations in aging and age-related diseases of the eye. *Investigative Ophthalmology and Visual Science*, 54(14):ORSF23–ORSF27, dec 2012.

[79] Honggang Gu, Xiuguo Chen, Chuanwei Zhang, Hao Jiang, and Shiyuan Liu. Study of the retardance of a birefringent waveplate at tilt incidence by Mueller matrix ellipsometer. *Journal of Optics (United Kingdom)*, 20(1):015401, jan 2018.

[80] Honggang Gu, Chuanwei Zhang, Hao Jiang, Xiuguo Chen, Weiqi Li, and Shiyuan Liu. Measurement errors induced by axis tilt of biplates in dual-rotating compensator Mueller matrix ellipsometers. In Bernd Bodermann, Karsten Frenner, and Richard M. Silver, editors, *Modeling Aspects in Optical Metrology V*, volume 9526, page 952617. SPIE, jun 2015.

[81] Antonio Guirao, Conceptión González, Manuel Redondo, Edward Geraghty, Sverker Norrby, and Pablo Artal. Average optical performance of the human eye as a function of age in a normal population. *Investigative Ophthalmology and Visual Science*, 40(1):203–213, 1999.

[82] Antonio Guirao, Manuel Redondo, and Pablo Artal. Optical aberrations of the human cornea as a function of age. *Journal of the Optical Society of America A*, 17(10):1697, oct 2000.

[83] Huanqing Guo, Zhaoqi Wang, Yang Wang, Qiuling Zhao, and Yan Wang. A new method to calculate corneal ablation depth based on optical individual eye model. *Optik*, 116(9):433–437, sep 2005.

[84] Nadav J. Hart, Yosef Koronyo, Keith L. Black, and Maya Koronyo-Hamaoui. Ocular indicators of Alzheimer's: exploring disease in the retina. *Acta Neuropathologica*, 132(6):767–787, dec 2016.

[85] Hecht and Eugene. *Optics*. Pearson Education, Inc., 2016.

[86] Eugene Hecht. *Optics*. Pearson Education, Inc., Boston, fifth edit edition, 2017.

[87] HH Hopkins. The use of diffraction-based criteria of image quality in automatic optical design. *Opt. Acta,*, 13:343–369, 1966.

[88] John Hornberger, Jay Bae, Ian Watson, Joe Johnston, and Michael Happich. Clinical and cost implications of amyloid beta detection with amyloid beta positron emission tomography imaging in early Alzheimer's disease–the case of florbetapir. *Current Medical Research and Opinion*, 33(4):675–685, apr 2017.

[89] P. A. Howarth, X. X. Zhang, A. Bradley, D. L. Still, and L. N. Thibos. Does the chromatic aberration of the eye vary with age? *Journal of the Optical Society of America A*, 5(12):2087, dec 1988.

[90] Xiang Run Huang, Harmobina Bagga, David S. Greenfield, and Robert W. Knighton. Variation of peripapillary retinal nerve fiber layer birefringence in normal human subjects. *Investigative Ophthalmology and Visual Science*, 45(9):3073–3080, sep 2004.

[91] Jennifer J. Hunter, Christopher J. Cookson, Marsha L. Kisilak, Juan M. Bueno, and Melanie C. W. Campbell. Characterizing image quality in a scanning laser ophthalmoscope with differing pinholes and induced scattered light. *Journal of the Optical Society of America A*, 24(5):1284, may 2007.

[92] K. Ichimoto, Kazuya Shinoda, T. Yamamoto, and J. Kiyohara. Photopolarimetric Measurement System of Mueller Matrix with Dual Rotating Waveplates. *Journal of Optics*, 16(139):139–141, 1985.

[93] Milos D. Ikonomovic, William E. Klunk, Eric E. Abrahamson, Chester A. Mathis, Julie C. Price, Nicholas D. Tsopelas, Brian J. Lopresti, Scott Ziolko, Wenzhu Bi, William R. Paljug, Manik L. Debnath, Caroline E. Hope, Barbara A. Isanski, Ronald L. Hamilton, and Steven T. DeKosky. Post-mortem correlates of in vivo PiB-PET amyloid imaging in a typical case of Alzheimer's disease. *Brain*, 131(6):1630–1645, jun 2008.

[94] S. N. Jasperson and S. E. Schnatterly. An improved method for high reflectivity ellipsometry based on a new polarization modulation technique. *Review of Scientific Instruments*, 40(6):761–767, jun 1969.

[95] Gopal Swamy Jayabalan and Josef F. Bille. The Development of Adaptive Optics and Its Application in Ophthalmology. In *High Resolution Imaging in Microscopy and Ophthalmology*, pages 339–358. Springer International Publishing, 2019.

[96] G. E. Jellison and F. A. Modine. Two-modulator generalized ellipsometry: theory. *Applied Optics*, 36(31):8190, nov 1997.

[97] Tao Jin. Polarimetric and birefringence analysis of presumed amyloid-beta deposits in the retina in association with Alzheimer's disease. *MSc Thesis*, sep 2018.

[98] Junichi Kaneshiro, Tomonobu M. Watanabe, Hideaki Fujita, and Taro Ichimura. Full control of polarization state with a pair of electro-optic modulators for polarization-resolved optical microscopy. *Applied Optics*, 55(5):1082, feb 2016.

[99] Nate J. Kemp, Jesung Park, Haitham N. Zaatari, H. Grady Rylander, and Thomas E. Milner. High-sensitivity determination of birefringence in turbid media with enhanced polarization-sensitive optical coherence tomography. *Journal of the Optical Society of America A*, 22(3):552, mar 2005.

[100] Ayala King, Eyal Gottlieb, David G. Brooks, Michael P. Murphy, and Joshua L. Dunaief. Mitochondria-derived Reactive Oxygen Species Mediate Blue Light-induced Death of Retinal Pigment Epithelial Cells. *Photochemistry and Photobiology*, 79(5):470–475, may 2007.

[101] H. B. klein Brink and G. J. van Blokland. Birefringence of the human foveal area assessed in vivo with Mueller-matrix ellipsometry. *Journal of the Optical Society of America A*, 5(1):49, jan 1988.

[102] Mei-mei Kong, Zhi-shan Gao, Xin-hua Li, Shu-hua Ding, Xiao-mei Qu, and Mei-qun Yu. A generic eye model by reverse building based on Chinese population. *Optics Express*, 17(16):13283, aug 2009.

[103] Yosef Koronyo, David Biggs, Ernesto Barron, David S. Boyer, Joel A. Pearlman, William J. Au, Shawn J. Kile, Austin Blanco, Dieu Trang Fuchs, Adeel Ashfaq, Sally Frautschy, Gregory M. Cole, Carol A. Miller, David R. Hinton, Steven R. Verdooner, Keith L. Black, and Maya Koronyo-Hamaoui. Retinal amyloid pathology and proof-of-concept imaging trial in Alzheimer's disease. *JCI insight*, 2(16), aug 2017.

[104] Vasudevan Lakshminarayanan and Andre Fleck. Zernike polynomials: a guide. *Journal of Modern Optics*, 58(7):545–561, apr 2011.

[105] D. Lara and C. Paterson. High resolution confocal polarimeter for the living human retina. volume 8011, page 80110E. International Society for Optics and Photonics, 8 2011.

[106] David Lara and Chris Dainty. Axially resolved complete Mueller matrix confocal microscopy. *Applied Optics*, 45(9):1917, 3 2006.

[107] Francesco LaRocca, Al-Hafeez Dhalla, Michael P. Kelly, Sina Farsiu, and Joseph A. Izatt. Optimization of confocal scanning laser ophthalmoscope design. *Journal of Biomedical Optics*, 18(7):076015, jul 2013.

[108] D. Layden, M. F. G. Wood, and I. A. Vitkin. Optimum selection of input polarization states in determining the sample Mueller matrix: a dual photoelastic polarimeter approach. *Optics Express*, 20(18):20466, aug 2012.

[109] Junyeop Lee and Min Sagong. Ultra-Widefield Retina Imaging: Principles of Technology and Clinical Applications. *Journal of Retina*, 1(1):1–10, may 2016.

[110] Yu Liang, Zhongquan Qu, Yue Zhong, Zhiming Song, and Shaoying Li. Analysis of errors in polarimetry using a rotating waveplate. *Applied Optics*, 58(36):9883, dec 2019.

[111] Hwey-Lan Liou and Noel A. Brennan. Anatomically accurate, finite model eye for optical modeling. *Journal of the Optical Society of America A*, 14(8):1684, aug 1997.

[112] Lourdes Llorente, Luis Diaz-Santana, David Lara-Saucedo, and Susana Marcos. Aberrations of the human eye in visible and near infrared illumination. *Optometry and Vision Science*, 80(1):26–35, jan 2003.

[113] W. Lotmar. Theoretical Eye Model with Aspherics. *Journal of the Optical Society of America*, 61(11):1522, nov 1971.

[114] Valérie Louis-Dorr, Karim Naoun, Paul Allé, Anne Marie Benoit, and Antoine Respiller. Linear dichroism of the cornea. *Applied Optics*, 43(7):1515–1521, mar 2004.

[115] Shih-Yau Lu and Russell A. Chipman. Interpretation of Mueller matrices based on polar decomposition. *Journal of the Optical Society of America A*, 13(5):1106, may 1996.

[116] A. Manivannan, J. N.P. Kirkpatrick, P. F. Sharp, and J. V. Forrester. Clinical investigation of an infrared digital scanning laser ophthalmoscope. *British Journal of Ophthalmology*, 78(2):84–90, feb 1994.

[117] A. Manivannan and P. F. Sharp. Digital fundus imaging using a scanning laser ophthalmoscope. *Physiological Measurement*, 14(1):43–56, 1993.

[118] Susana Marcos, Stephen A. Burns, Esther Moreno-Barriusop, and Rafael Navarro. A new approach to the study of ocular chromatic aberrations. *Vision Research*, 39(26):4309–4323, dec 1999.

[119] Charles Marcus, Esther Mena, and Rathan M. Subramaniam. Brain PET in the diagnosis of Alzheimer's disease, oct 2014.

[120] Susana Martinez-Conde, Stephen L. Macknik, and David H. Hubel. The role of fixational eye movements in visual perception. *Nature Reviews Neuroscience*, 5(3):229–240, 2004.

[121] JS McLellan, S Marcos, SA Burns Ophthalmology & Visual ..., and Undefined 2001. Age-related changes in monochromatic wave aberrations of the human eye. *tvst.arvojournals.org*, 42(6):1390–1295, 2001.

[122] Roger J. McNichols and Gerard L. Cote. Optical glucose sensing in biological fluids: an overview. *Journal of Biomedical Optics*, 5(1):5, 2000.

[123] David Merino, Jacque L. Duncan, Pavan Tiruveedhula, and Austin Roorda. Observation of cone and rod photoreceptors in normal subjects and patients using a new generation adaptive optics scanning laser ophthalmoscope. *Biomedical Optics Express*, 2(8):2189, aug 2011.

[124] Gary P. Misson. A Mueller matrix model of Haidinger's brushes. *Ophthalmic and Physiological Optics*, 23(5):441–447, sep 2003.

[125] Aaron Nagiel, Robert A. Lalane, SriniVas R. Sadda, and Steven D. Schwartz. Ultra-widefield fundus imaging. *Retina*, 36(4):660–678, apr 2016.

[126] R. Navarro, J. Santamaría, and J. Bescós. Accommodation-dependent model of the human eye with aspherics. *Journal of the Optical Society of America A*, 2(8):1273, aug 1985.

[127] Rafael Navarro. Incorporation of intraocular scattering in schematic eye models. *Journal of the Optical Society of America A*, 2(11):1891, nov 1985.

[128] Rafael Navarro. The optical design of the human eye: A critical review, jan 2009.

[129] Rafael Navarro, Fernando Palos, and Luis González. Adaptive model of the gradient index of the human lens I Formulation and model of aging ex vivo lenses. *Journal of the Optical Society of America A*, 24(8):2175, aug 2007.

[130] & Hernández-Matamoros J. Navarro R., González L. On the Prediction of Optical Aberrations by Personalized Eye Models. *Optometry and Vision Science*, 83(6):371–381, jun 2006.

[131] Peter Andrew Charles Neathway. *Morphological and Multifractal Analyses of Retinal Amyloid Deposits for Staging in Alzheimer's Disease*. PhD thesis, University of Waterloo, feb 2020.

[132] P. Q.J. Nederpel and J. W.D. Martens. Magneto-optical ellipsometer. *Review of Scientific Instruments*, 56(5):687–690, may 1985.

[133] Newport. Polarization in Fiber Optics, 2020.

[134] O Pomerantzeff; R H Webb; F C Delori. Image formation in fundus cameras. *Investigative Ophthalmology & Visual Science*, 18:630–637, jun 1979.

[135] Marsha Oberholzer, Wayne D.H. Gillan, and Alan Rubin. Higher order aberrations of the eye: Part one, jun 2016.

[136] Cristina M. Oliveira, Andreia Ferreira, and Sandra Franco. Wavefront analysis and Zernike polynomial decomposition for evaluation of corneal optical quality, feb 2012.

[137] Tetsuro Oshika, Stephen D Klyce, Raymond A Applegate, and Howard C Howland. Changes in Corneal Wavefront Aberrations with Aging. *Investigative Ophthalmology & Visual Science*, 40(7):1351–1355, 1999.

[138] James B. Pawley. *Handbook of biological confocal microscopy: Third edition*. Springer US, 2006.

[139] Bernhard C. E. Pelz, Christian Weschenmoser, Stefan Goelz, Joerg P. Fischer, Reinhard O. W. Burk, and Josef F. Bille. In-vivo measurement of the retinal birefringence with regard to corneal effects using an electro-optical ellipsometer. In Reginald Birngruber, Adolf F. Fercher, and Philippe Sourdille, editors, *Lasers in Ophthalmology IV*, volume 2930, pages 92–101. SPIE, dec 1996.

[140] Daniel P. Perl. Neuropathology of Alzheimer's disease, jan 2010.

[141] Michael Pircher, Erich Götzinger, Rainer Leitgeb, Harald Sattmann, Oliver Findl, and Christoph. K. Hitzenberger. Imaging of polarization properties of human retina in vivo with phase resolved transversal PS-OCT. *Optics Express*, 12(24):5940, nov 2004.

[142] Adrian Gh. Podoleanu and Richard B. Rosen. Combinations of techniques in imaging the retina with high resolution. *Progress in Retinal and Eye Research*, 27(4):464–499, jul 2008.

[143] Jason Porter, Antonio Guirao, Ian G. Cox, and David R. Williams. Monochromatic aberrations of the human eye in a large population. *Journal of the Optical Society of America A*, 18(8):1793, aug 2001.

[144] Ji Qi and Daniel S. Elson. Mueller polarimetric imaging for surgical and diagnostic applications: a review. *Journal of Biophotonics*, 10(8):950–982, aug 2017.

[145] Yunyi Qiu. *Predicting the thioflavin fluorescence of retinal amyloid deposits in association with Alzheimer's disease and differentiating amyloid protein from alpha-syn*. PhD thesis, University of waterloo, sep 2020.

[146] Bennett Rabbett. *Clinical Visual Optics*. Butterworth-Heinemann, second edition, 1989.

[147] Scott C. Rashleigh. Origins and Control of Polarization Effects in Single-Mode Fibers. *Journal of Lightwave Technology*, 1(2):312–331, 1983.

[148] Austin John. Roorda. *Double pass reflections in the human eye*. Phd thesis, University of Waterloo, 1998.

[149] Roorda A. J. *Double pass reflections in the human eye.* PhD thesis, University of Waterloo, Waterloo, 1996.

[150] Thomas O. Salmon and Corina van de Pol. Normal-eye Zernike coefficients and root-mean-square wavefront errors. *Journal of Cataract and Refractive Surgery*, 32(12):2064–2074, dec 2006.

[151] Thomas O Salmon, Roger W West, Wayne Gasser, and Todd Kenmore. Measurement of Refractive Errors in Young Myopes Using the COAS Shack-Hartmann Aberrometer. *Optometry and Vision Science*, 80(1), 2003.

[152] S. M. Salvi, S. Akhtar, and Z. Currie. Ageing changes in the eye, sep 2006.

[153] Jim Schwiegerling. Scaling Zernike expansion coefficients to different pupil sizes. *Journal of the Optical Society of America A*, 19(10):1937, oct 2002.

[154] Richa Sharma, Toshifumi Mihashi, and Howard C. Howland. Compensation of monochromatic aberrations in older eyes. *Journal of Modern Optics*, 55(4-5):773–781, feb 2008.

[155] Leslie M. Shaw, Hugo Vanderstichele, Malgorzata Knapik-Czajka, Christopher M. Clark, Paul S. Aisen, Ronald C. Petersen, Kaj Blennow, Holly Soares, Adam Simon, Piotr Lewczuk, Robert Dean, Eric Siemers, William Potter, Virginia M.Y. Lee, and John Q. Trojanowski. Cerebrospinal fluid biomarker signature in alzheimer's disease neuroimaging initiative subjects. *Annals of Neurology*, 65(4):403–413, apr 2009.

[156] C. J.R. Sheppard and T. Wilson. Effects of high angles of convergence on V(z) in the scanning acoustic microscope. *Applied Physics Letters*, 38(11):858–859, jun 1981.

[157] Warren Smith. Modern Optical Engineering, Third Edition — (2000) — Smith — Publications — Spie.

[158] Warren J Smith, New York, Chicago San, Francisco Lisbon, London Madrid, Mexico City, Milan New, Delhi San, and Juan Seoul. *Modern Optical Engineering The Design of Optical Systems Fourth Edition*. McGraw-Hill Education, 2008.

[159] Hongxin Song, Xiaofeng Qi, Weiyao Zou, Zhangyi Zhong, and Stephen A. Burns. Dual electro-optical modulator polarimeter based on adaptive optics scanning laser ophthalmoscope. *Optics Express*, 18(21):21892, oct 2010.

[160] Giovanni Staurenghi, Francesco Viola, Martin A. Mainster, Raymond D. Graham, and Peter G. Harrington. Scanning laser ophthalmoscopy and angiography with a wide-field contact lens system. *Archives of Ophthalmology*, 123(2):244–252, feb 2005.

[161] Synopsys Code V. Optical Design Solutions by Synopsys, 2020.

[162] L. Thaler, A.C. Schütz, M.A. Goodale, and K.R. Gegenfurtner. What is the best fixation target? The effect of target shape on stability of fixational eye movements. *Vision Research*, 76:31–42, jan 2013.

[163] Larry N. Thibos, Raymond A. Applegate, James T. Schwiegerling, and Robert Webb. Standards for reporting the optical aberrations of eyes. *Journal of Refractive Surgery*, 18(5):S652–S660, sep 2002.

[164] Larry N. Thibos, Xin Hong, Arthur Bradley, and Xu Cheng. Statistical variation of aberration structure and image quality in a normal population of healthy eyes. *Journal of the Optical Society of America A*, 19(12):2329, dec 2002.

[165] Larry N. Thibos, Ming Ye, Xiaoxiao Zhang, and Arthur Bradley. The chromatic eye: a new reduced-eye model of ocular chromatic aberration in humans. *Applied Optics*, 31(19):3594, jul 1992.

[166] George T Timberlake and Michael Kennedy. The Direct Ophthalmoscope How it Works and How to Use It. Technical report, University of Kansas Medical Center, 2005.

[167] K. Twietmeyer, R. Chipman, and A. Elsner. GDx-MM: An imaging mueller matrix retinal polarimeter. In *Optics InfoBase Conference Papers*, page FWE4. Optical Society of America (OSA), sep 2007.

[168] K. M. Twietmeyer and R. A. Chipman. Optimization of Mueller matrix polarimeters in the presence of error sources. *Optics Express*, 16(15):11589, jul 2008.

[169] K. M. Twietmeyer, R. A. Chipman, Ann E. Elsner, Y. Zhao, and D. VanNasdale. Mueller matrix retinal imager with optimized polarization conditions. *Optics Express*, 16(26):21339, dec 2008.

[170] Karen Marie Twietmeyer. *GDx-MM: An Imaging Mueller Matrix Retinal Polarimeter*. PhD thesis, The University of Arizona, Tucson, oct 2007.

[171] G. J. Van Blokland and S. C. Verhelst. Corneal polarization in the living human eye explained with a biaxial model. *Journal of the Optical Society of America A*, 4(1):82, jan 1987.

[172] W Kosnik, J Fikre, and R Sekuler. Visual fixation stability in older adults. — IOVS — ARVO Journals. *Investigative Ophthalmology & Visual Science*, 27(12):1720–1725, dec 1986.

[173] Li Wang and Douglas D. Koch. Ocular higher-order aberrations in individuals screened for refractive surgery. *Journal of Cataract and Refractive Surgery*, 29(10):1896–1903, 2003.

[174] Shuang Wang, Xie Han, Yaning Wang, and Kewu Li. Dispersion of the Retardation of a Photoelastic Modulator. *Applied Sciences*, 9(2):341, jan 2019.

[175] Colin Ware. Human axial chromatic aberration found not to decline with age. *Graefe's Archive for Clinical and Experimental Ophthalmology*, 218(1):39–41, jan 1982.

[176] R. A. Weale. Sex, age and the birefringence of the human crystalline lens. *Experimental Eye Research*, 29(4):449–461, oct 1979.

[177] Robert H. Webb and George W. Hughes. Scanning Laser Ophthalmoscope. *IEEE Transactions on Biomedical Engineering*, BME-28(7):488–492, jul 1981.

[178] Robert H. Webb, George W. Hughes, and Francois C. Delori. Confocal scanning laser ophthalmoscope. *Applied Optics*, 26(8):1492, apr 1987.

[179] Gerald Westheimer. The maxwellian view. *Vision Research*, 6(6):669–682, dec 1966.

[180] Gerald Westheimer. Specifying and controlling the optical image on the human retina. *Progress in retinal and eye research*, 25, 2006.

[181] T. Wilson and A. R. Carlini. Size of the detector in confocal imaging systems. *Optics Letters*, 12(4):227, apr 1987.

[182] C Wilson, T., & Sheppard. Theory And Practice Of Scanning Optical Microscopy, 1984.

[183] B. S. Winkler, M. E. Boulton, J. D. Gottsch, and P. Sternberg. Oxidative damage and age-related macular degeneration., 1999.

[184] Matthew T. Witmer, George Parlitsis, Sarju Patel, and Szilárd Kiss. Comparison of ultra-widefield fluorescein angiography with the Heidelberg Spectralis® noncontact ultra-widefield module versus the Optos® Optomap®. *Clinical Ophthalmology*, 7:389–394, feb 2013.

[185] W. H. Woon, F. W. Fitzke, A. C. Bird, and J. Marshall. Confocal imaging of the fundus using a scanning laser Ophthalmoscope. *British Journal of Ophthalmology*, 76(8):470–474, aug 1992.

[186] World Health Organization. Dementia, sep 2020.

[187] James C Wyant and Katherine Creath. Basic Wavefront Aberration Theory for Optical Metrology. Technical report, Optical Sciences Center, University of Arizona, 1992.

[188] X. Steve Yao, Lianshan Yan, and Yongqiang Shi. Highly repeatable all-solid-state polarization-state generator. *Optics Letters*, 30(11):1324, jun 2005.

[189] Henrik Zetterberg, Lars Olof Wahlund, and Kaj Blennow. Cerebrospinal fluid markers for prediction of Alzheimer's disease. *Neuroscience Letters*, 352(1):67–69, nov 2003.

[190] Stefan Zotter, Michael Pircher, Erich Götzinger, Teresa Torzicky, Hirofumi Yoshida, Futoshi Hirose, Stephan Holzer, Julia Kroisamer, Clemens Vass, Ursula Schmidt-Erfurth, and Christoph K. Hitzenberger. Measuring retinal nerve fiber layer birefringence, retardation, and thickness using wide-field, high-speed polarization sensitive spectral domain OCT. *Investigative Ophthalmology and Visual Science*, 54(1):72–84, jan 2013.

APPENDICES

Appendix A

Supplementary to Chapter 4

A.1 Optimal pinhole size for improved image quality

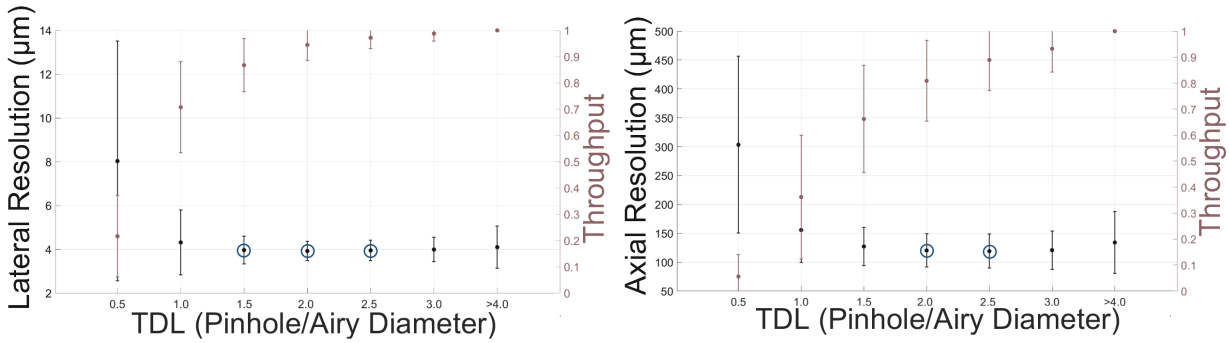

Figure A.1: Average resolution and throughput for varying TDLs for subjects 20-32 years old. [Left] Average best lateral resolution for those with an optimal entrance pupil size of 3.0 mm. [Right] Average best axial resolution for those with an optimal entrance pupil size of 3.75 mm.

Appendix B

Supplementary to Chapter 5

B.1 Optical Designs in CodeV

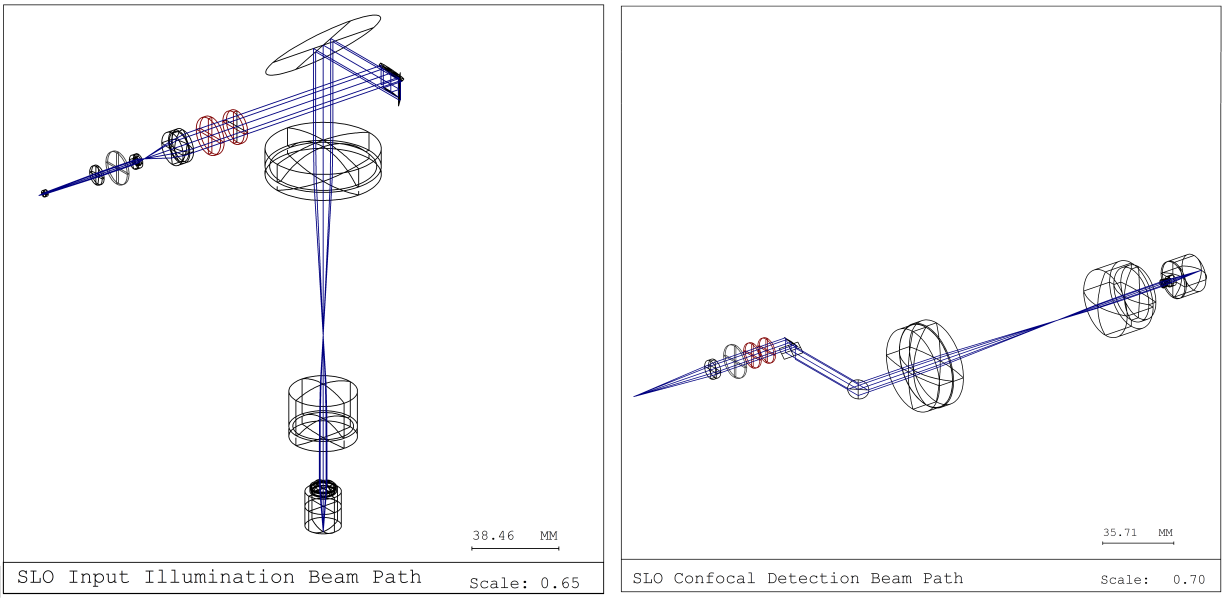

Figure B.1: Optical design in Code V [Left] Input illumination channel in the MM polarimeter using a large exit pupil cSLO design. [Right] Detection channel in the MM polarimeter using a small entrance pupil cSLO design. Polarization optics, PSG and PSA, are illustrated with red. Dimensions were modified for better visualization.